Channumsin, Sittiporn (2016) A deformation model of flexible, high area-to-mass ratio debris under perturbations and validation method. PhD thesis

http://theses.gla.ac.uk/7531/

# A DEFORMATION MODEL OF FLEXIBLE, HIGH AREA-TO-MASS RATIO DEBRIS UNDER PERTURBATIONS AND VALIDATION METHOD

Sittiporn Channumsin

Submitted in fulfilment of the requirements for the
Degree of Doctor of Philosophy

Aerospace Sciences Research Division
School of Engineering
University of Glasgow

Sittiporn Channumsin*: A deformation model of flexible, high area-to-mass ratio debris for accurate propagation under perturbations and validation method* submitted in fulfilment of the requirements for the Doctor of Philosophy
Aerospace Sciences Research Division, School of Engineering
University of Glasgow

ADVISORS:
Dr. Gianmarco Radice
Dr. Matteo Ceriotti

EXAMINERS: Prof Colin R. McInnes and Dr. Stuart Grey

LOCATION:
Glasgow, Scotland

DATE:
Aug 2016

# Abstract

A new type of space debris was recently discovered by Schildknecht in near - geosynchronous orbit (GEO). These objects were later identified as exhibiting properties associated with High Area-to-Mass ratio (HAMR) objects. According to their brightness magnitudes (light curve), high rotation rates and composition properties (albedo, amount of specular and diffuse reflection, colour, etc), it is thought that these objects are multilayer insulation (MLI). Observations have shown that this debris type is very sensitive to environmental disturbances, particularly solar radiation pressure, due to the fact that their shapes are easily deformed leading to changes in the Area-to-Mass ratio (AMR) over time.

This thesis proposes a simple effective flexible model of the thin, deformable membrane with two different methods. Firstly, this debris is modelled with Finite Element Analysis (FEA) by using Bernoulli-Euler theory called "Bernoulli model". The Bernoulli model is constructed with beam elements consisting 2 nodes and each node has six degrees of freedom (DoF). The mass of membrane is distributed in beam elements. Secondly, the debris based on multibody dynamics theory call "Multibody model" is modelled as a series of lump masses, connected through flexible joints, representing the flexibility of the membrane itself. The mass of the membrane, albeit low, is taken into account with lump masses in the joints. The dynamic equations for the masses, including the constraints defined by the connecting rigid rod, are derived using fundamental Newtonian mechanics. The physical properties of both flexible models required by the models (membrane density, reflectivity, composition, etc.), are assumed to be those of multilayer insulation. Both flexible membrane models are then propagated together with classical orbital and attitude equations of motion near GEO region to predict the orbital evolution under the perturbations of solar radiation pressure, Earth's gravity field, luni-solar gravitational fields and self-shadowing effect. These results are then compared to two rigid body models (cannonball and flat rigid plate). In this investigation, when comparing with a rigid model, the evolutions of orbital elements of the flexible models indicate the difference of inclination and secular eccentricity evolutions, rapid irregular attitude motion and unstable cross-section area due to a deformation over time. Then, the Monte Carlo simulations by varying initial attitude dynamics ($\psi$, $\theta$, $\phi$) and deformed angle ($\theta_d$) are investigated and compared with rigid models over 100 days. As the results of the simulations, the different initial conditions provide unique orbital motions, which is significantly different in term of orbital motions of both rigid models.

Furthermore, this thesis presents a methodology to determine the material dynamic properties of thin membranes and validates the deformation of the multibody model with real MLI materials. Experiments are performed in a high vacuum chamber ($10^{-4}$ mbar) replicating space environment. A thin membrane is hinged at one end but free at the other. The free motion experiment, the first experiment, is a free vibration test to determine the damping coefficient and natural frequency of the thin membrane. In this test, the membrane is allowed to fall freely in the chamber with the motion tracked and captured through high velocity video frames. A Kalman filter technique is implemented in the tracking algorithm to reduce noise and increase the tracking accuracy of the oscillating motion. The forced motion experiment, the last test, is performed to determine the deformation characteristics of the object. A high power spotlight (500-2000W) is used to illuminate the MLI and the displacements are measured by means of a high resolution laser sensor. Finite Element Analysis (FEA) and multibody dynamics of the experimental setups are used for the validation of the flexible model by comparing with the experimental results of displacements and natural frequencies.

# Table of Contents

# List of Tables

# List of Figures

# Acknowledgement

Firstly, I would like to acknowledge Ministry of Science and Technology of the Thai government who provides full financial support for my PhD study and European Office of Aerospace Research and Development to support travelling finance to conference on abroad and budget for my experiments. I would like to thank Dr.Siridech Bonsang and Dr. Kasin Vichienchom who motivate me to study postgraduate and advise me for the sources of scholarships. None of this work would have happened without my both supervisors, Dr. Gianmarco Radice and Dr. Matteo Ceriotti who guide and share many great novel ideas including useful feedbacks to improve my research and this dissertation throughout my PhD study. I would like to thank Dr. Ian Watson allows me to use a vacuum chamber for my experiment including basis guideline of a vacuum chamber. Then, Colin Roberts supports to set up and train me how to use the vacuum chamber and Dr. Andrew Feeney gives me some suggestions of a laser instrument. I would like to thank my friends from Space Research Space Glasgow Research Group at the University of Glasgow, Alessandro supporting me to use Linux-based computer cluster, Nicola, Leonel, Abdul, Spencer, Alisha, Chenthamarai and others who I do not mention for good times together in Glasgow. Lastly, I am also very grateful to my wife Manun Wongserepipatana for great support and for her assistance in all processes. This dissertation is dedicated to my parents and my family who encourage me to study postgraduate and are always besides me. Without my family, I would not even have the chance to pursue a PhD.

Sittiporn Channumsin

# Journal and conference publications

S. Channusmin, M. Ceriotti, and G. Radice, "*A Deformation model of Flexible, HAMR objects for accurate propagation under perturbations and self-shadowing effects*", Advances in Space Research: (Under revision)

S. Channusmin, M. Ceriotti, and G. Radice, "*Damping measurement and deformation validation of flexible, high area-to-mass ratio debris model*", 66th International Astronautical Congress, Oct 12-15 2015: Jerusalem, Israel.

S. Channusmin, M. Ceriotti, and G. Radice, "*A deformation model of flexible, high area-to-mass ratio debris under perturbations*", Aerospace Symposium 2015: The Aerospace Ecosystem. Oct 2014: Glasgow, UK.

S. Channusmin, M. Ceriotti, and G. Radice, "*A Deformation model of Flexible, high area-to-mass ratio debris for accurate propagation under perturbation*", 65th International Astronautical Congress. Sep 2014: Toronto, Canada.

S. Channusmin, M. Ceriotti, G. Radice, "*A deformation model of flexible, high area-to-mass ratio debris under perturbations", in 1st Stardust Global Virtual Workshop, Glasgow, UK, 2014.*

S. Channusmin, M. Ceriotti, G. Radice, and C. Früh, "*Orbital dynamics of lightweight flexible debris*", 64th International Astronautical Congress. Sep 2013: Beijing, China.

# Author’s Declaration

I hereby declare that this submission is my own work and that, to the best of my knowledge and Belief, it contains no material previously published or written by another person nor material which to a substantial extent has been accepted for the qualification of any other degree or diploma of a university or other institute of higher learning, except where due acknowledgment is made in the text.

Glasgow, United Kingdom,

Sittiporn Channumsin

# Definitions/Abbreviation

## Acronyms

| | |
|---|---|
| AU | Astronomical Unit, 149,597,870 km |
| AIUM | Astronomical Institute of the University of Bern |
| AMR | Area-to-Mass-Ratio |
| ASAT | Anti-satellite |
| DCM | Direction Cosine Matrix |
| DoF | Degree of Freedom |
| DISCOS | Database and Information System Characterising Objects in Space |
| DS | DebrisSat |
| ECI | Earth centred Inertial frame |
| EISCAT | European Incoherent Scatter Scientific Association |
| EVOLVE | Evolutionary debris environment model |
| ESA | European space agency |
| ESASDT | ESA Space Debris Telescope |
| FEA | Finite Element Analysis |
| FEM | Finite Element Method |
| FEP | Fluorpropylencopolymers |
| FFT | Fast Fourier Transform |
| FY-1C | Fengyun 1C |
| GEO | Geostationary Earth Orbit |
| GTO | Geostationary Transfer Orbit |
| HAMR | High Area-to-Mass Ratio |
| IADC | Inter-Agency Space Debris Coordination Committee |
| LEGEND | A LEO-to-GEO Environment Debris model |
| LEO | Low Earth Orbit |
| LHS | Latin Hypercube Sampling |
| MASTER | Meteoroid And Space Debris Terrestrial Environment Reference model |
| MEGNO | Mean Exponential Growth factor of Nearby Orbits |
| MEO | Medium Earth Orbit |
| MLI | Multilayer insulation |
| NASA | National Aeronautics and Space Administration |
| ODPO | Orbital Debris Program Office |
| PET | Polyethylene terephthalate |
| SRP | Solar radiation pressure |
| STK | Systems Tool Kit |
| SSN | Space Surveillance Network |
| TIRA | Tracking & Imaging Radar |
| ZIMLAT | Zimmerwald Laser and Astrometry Telescope |

# Nomenclature

## Chapter1 Introduction

| | |
|---|---|
| $A_{eff}$ | effective cross-sectional area |
| $A$ | maximum surface area of object |
| $C_r$ | dimensionless radiation pressure coefficient |
| $D_{reflectivity}$ | estimated coefficient due to reflectivity |
| $D_{deformation}$ | estimated coefficient due to deformation |
| $D_{tumbling}$ | estimated coefficient due to tumbling |

## Chapter2 Orbital dynamics of HAMR rigid object

| | |
|---|---|
| $A$ | Maximum surface area of flat plate |
| $A_{eff}$ | effective cross-sectional area |
| $\vec{a}_{\odot}$ | third-body attraction induced by the Sun |
| $\vec{a}_{\leftmoon}$ | third-body attraction induced by the Moon |
| $\vec{a}_{SRP}$ | solar radiation acceleration |
| $\vec{a}_{cannon}$ | solar radiation acceleration of cannonball model |
| $\vec{B}$ | position vector in body frame coordinates |
| $C_{Rs}$ | coefficients of specular reflection |
| $C_{Rd}$ | coefficients of diffuse reflection |
| $C_{Ra}$ | coefficients of absorbed reflection |
| $c$ | speed of light, 299,792,458 m/s |
| $E$ | solar flux constant, 1353 $W/m^2$ |
| $[E]$ | eigenvector matrix |
| $\vec{F}_{\oplus}$ | force of gravity acting on the object from the Earth |
| $\vec{F}_{SRP}$ | solar radiation pressure, |
| $G$ | gravity constant, $6.67259\times10^{-11}$ $m^3/(kg\cdot s^2)$ |
| $\dot{\vec{H}}$ | derivative of angular momentum vector of a rigid body at the centre of mass |
| $[\mathrm{I}]$ | identity matrix notation |
| $[I]$ | matrix of moment of inertia of objects |
| $l$ | length of the object, m |
| $m_{\oplus}$ | mass of the Earth, $5.9742\times10^{24}$ kg |
| $M_1$ | mass of the Sun, $1.9891\times10^{30}$ kg |
| $M_2$ | mass of the Earth, $7.348\times10^{22}$ kg |
| $m_{obj}$ | mass of an object |
| $\vec{N}$ | position vector in reference frame coordinates |
| $\hat{N}$ | surface normal unit vector |
| $\vec{q}$ | quaternion vector |

| | |
|---|---|
| $\dot{\vec{q}}$ | derivative of quaternion vector |
| $\vec{R}$ | position vector of the object transformed to the body system |
| $\vec{r}$ | position vector of the object in a inertial frame |
| $\vec{r}_1$ | position vector of the Sun in a inertial frame |
| $\vec{r}_2$ | position vector of the Moon in a inertial frame |
| $\ddot{\vec{r}}_{tot}$ | total acceleration of the space debris |
| $\ddot{\vec{r}}$ | acceleration of the space debris relative to the Earth |
| $\ddot{\vec{r}}_1$ | acceleration vector of the Sun gravitational perturbation in the inertial frame |
| $\ddot{\vec{r}}_2$ | acceleration vector of the Moon gravitational perturbation in the inertial frame |
| $\hat{S}$ | solar incidence unit vector |
| $[T]$ | transformation matrix from the inertial frame to the body frame |
| $w$ | width of the object |
| $\theta_{inc}$ | incident angle between $\hat{N}$ and $\hat{S}$ |
| $\vec{\tau}_t$ | total external torque acting on the body |
| $\vec{\tau}_{SRP}$ | solar radiation torque |
| $\vec{\tau}_{Grav}$ | gravitational torque |
| $\vec{\rho}_{SRP}$ | vector from the geometric centre of the objects to the centre of pressure |
| $\vec{\omega}$ | angular velocity vector of the debris with respect to the inertial frame |
| $\dot{\vec{\omega}}$ | derivative angular velocity vector of the debris with respect to the inertial frame |
| $\Psi$ | yaw angle |
| $\theta$ | pitch angle |
| $\phi$ | roll angle |
| $e$ | principal axis of eigenvector |
| $\alpha$ | principal angle of eigenvector |
| $\Omega$ | angular velocity matrix |
| $\mu_1$ | Sun gravitational constant $1.3279\times10^{11}$ km$^3$/s$^2$ |
| $\mu_2$ | Moon gravitational constant $4.9047\times10^{3}$ km$^3$/s$^2$ |

## Chapter3 Flexible model with Bernoulli-Euler theory

| | |
|---|---|
| $A_j$ | area of the $j^{\text{th}}$ beam element |
| $\vec{a}_{SRP,j}$ | SRP acceleration of $j^{\text{th}}$ node |
| $C_{Rs,j}$ | coefficients of diffuse of the $j^{\text{th}}$ beam element |
| $C_{Rd,j}$ | coefficients of specular of the $j^{\text{th}}$ beam element |
| $C_{Ra,j}$ | coefficients of absorption of the $j^{\text{th}}$ beam element |
| $c$ | speed of light (299,792,458 m/s) |
| $[C]$ | damping matrix of beam element inertial frame |
| $E_y$ | Young’s Modulus of material |
| $E$ | solar flux constant, 1,353 W/m$^2$ |
| $\vec{F}_{G(j)\perp}$ | perpendicular gravitational force of $j^{\text{th}}$ node |
| $\vec{F}_{sun(j)\perp}$ | perpendicular solar force of $j^{\text{th}}$ node |

| | |
|---|---|
| $\left[F_{x1}, F_{y1}, F_{z1}\right]$ | total external force of 1st node |
| $\left[F_{x2}, F_{y2}, F_{z2}\right]$ | total external force of 2nd node |
| $I_y$ | mass moment of inertia with respect to y axis |
| $I_z$ | mass moment of inertia with respect to z axis |
| $J$ | polar moment of inertia of the cross section area of beam |
| $\left[K\right]$ | stiffness matrix of beam element in inertial frame |
| $\left[\bar{K}\right]$ | stiffness matrix of beam element in body frame |
| $L_1 = L_2$ | length of beam element |
| $\vec{M}_{G,j}$ | gravitational torque of *j*th beam element |
| $\vec{M}_{sun,j}$ | solar radiation torque of *j*th beam element |
| $\left[M\right]$ | mass matrix of beam element in inertial frame |
| $\left[\bar{M}\right]$ | mass matrix of beam element in body frame |
| $\left[M_{x1}, M_{y1}, M_{z1}\right]$ | torsion moment of 1st node |
| $\left[M_{x1}, M_{y1}, M_{z1}\right]$ | torsion moment of 2nd node |
| $m_j$ | mass of *j*th beam element |
| $\hat{N}_j$ | surface normal unit vector of *j*th beam element |
| $\hat{S}_j$ | unit sun vector of *j*th beam element |
| $T_e$ | transformation matrix from body frame to inertial frame |
| $[u_1, u_2, u_3]$ | x, y and z displacement of the 1st node, km |
| $[u_4, u_5, u_6]$ | x, y and z displacement of the 2nd node, km |
| $\vec{x}_j$ | position vector of a centre of *j*th beam element in the inertial frame |
| $\vec{x}_1$ | the sun vector in the inertial frame |
| $[\theta_{x1}, \theta_{y1}, \theta_{z1}]$ | 3D rotation of the 1st node |
| $[\theta_{x2}, \theta_{y2}, \theta_{z2}]$ | 3D rotation of the 2nd node |
| $\alpha$ | coefficients related to mass |
| $\beta$ | coefficients related to stiffness |

## Chapter4 Flexible model with multibody model

| | |
|---|---|
| $A_{sphere}$ | surface sphere area |
| $AU$ | astronomical unit, 149,597,870 km |
| $A_{eq}$ | equivalent cross-sectional area |
| $A_j$ | cross sectional area of the *j*th rod |
| $a$ | semi-major axis |
| $\vec{a}_{J_2}$ | accelerations of oblateness |
| $\vec{a}_{\odot}$ | accelerations of third body from the Sun |
| $\vec{a}_{☾}$ | accelerations of third body from the Moon |
| $\vec{a}_{SRP,j}$ | SRP acceleration of *j*th lump mass |
| $\vec{a}_{avg}$ | accelerations of average solar radiation pressure |

| | |
|---|---|
| $C_{Rd,j}$ | coefficients of diffuse of the $j^{\text{th}}$ rod |
| $C_{Rs,j}$ | coefficients of specular of the $j^{\text{th}}$ rod |
| $C_{Ra,j}$ | coefficients of absorption of the $j^{\text{th}}$ rod |
| $c$ | speed of light, 299,792,458 m/s |
| $c_s$ | rotational damping constant |
| $D_F$ | dissipation factor of the material |
| $e$ | eccentricity |
| $E_y$ | young modulus of material |
| $E$ | solar flux constant, 1,353 W/m$^2$ |
| $\vec{F}_{avg}$ | average SRP force vector |
| $\vec{F}_{d,i}$ | rotational damper force vector of $i^{\text{th}}$ lump mass |
| $\vec{F}_{ext,i}$ | external force vector from a summation of both conservative and non-conservative perturbations of $i^{\text{th}}$ lump mass |
| $\vec{F}_{s,i}$ | rotational spring force vector of $i^{\text{th}}$ lump mass |
| $\vec{F}_{SRP,j}$ | solar radiation force vector of $j^{\text{th}}$ rod |
| $\vec{F}_{total,i}$ | total force vector acting on the $i^{\text{th}}$ lump masse |
| $G$ | gravity constant, 6.67259×10$^{-11}$ km$^3$/(kg·s$^2$) |
| $I$ | moment of inertia of cross section area |
| $i$ | inclination |
| $J_2$ | the 2$^{\text{th}}$ zonal harmonic coefficient, 0.00108263 |
| $k_s$ | rotational spring constant |
| $L$ | true longitude |
| $l_j$ | length of $j^{\text{th}}$ rod |
| $\vec{l}$ | light source vector |
| $\hat{N}_j$ | surface normal unit vector of j$^{\text{th}}$ rod |
| $M$ | total mass of membrane |
| $m_i$ | mass of $i^{\text{th}}$ lump mass ($i$=1,2,3) |
| P | plane: $\vec{n}_p \cdot \vec{x}_p + d_p = 0$ |
| $P_{SP}$ | solar radiation pressure per unit area |
| $\vec{p}$ | projection vector of shadow |
| $p$ | semilatus rectum |
| $\dot{\vec{q}}$ | derivative of quaternions vector |
| $\vec{q}$ | quaternions vector |
| $\ddot{\vec{x}}_i$ | total acceleration vector of $i^{\text{th}}$ lump mass |
| $\vec{x}$ | position vector of debris in inertial frame |
| $R_\oplus$ | radius of the Earth (6,378.13 km) |
| $\hat{S}$ | solar unit vector |
| $\hat{S}_j$ | solar unit vector of $j^{\text{th}}$ rod |
| $\vec{T}_j$ | tension force vector generated by the $j^{\text{th}}$ rod |
| $\vec{v}$ | vertex of plane |
| $\theta_d$ | deformation angle |
| $\dot{\theta}_d$ | angular velocity deformation angle |
| $\omega$ | argument of perigee |
| $\Omega$ | right ascension of ascending node |

| | |
|---|---|
| $\varphi$ | geocentric latitude of the object in ECI frame |
| $\nu$ | true anomaly |
| $\lambda_s$ | solar longitude |
| $\delta_s$ | solar latitude |
| $\vec{\tau}_j$ | summation of disturbance torques of $j^{\text{th}}$ rod |
| $\psi$, | yaw angle |
| $\theta$ | pitch angle |
| $\phi$ | roll angle |
| $\vec{\omega}_j$ | angular velocity of $j^{\text{th}}$ rod |
| $\dot{\vec{\omega}}_j$ | angular acceleration of $j^{\text{th}}$ rod |
| $[p, f, g, h, k, L]$ | modified equinoctial orbital elements |
| $[\dot{p}, \dot{f}, \dot{g}, \dot{h}, \dot{k}, \dot{L}]$ | differential modified equinoctial orbital elements |
| $[\vec{\Delta}_r, \vec{\Delta}_t, \vec{\Delta}_n]$ | non-two-body perturbations in the radial ( $\hat{R}$ ), tangential ( $\hat{T}$ ) and normal ( $\hat{N}$ ) directions respectively |
| $x_1, y_1, z_1$ | the vector position of the first lump mass |
| $x_2, y_2, z_2$ | the vector position of the second lump mass |
| $x_3, y_3, z_3$ | the vector position of the third lump mass |

## Chapter 5 Damping measurement and solar radiation pressure validation

| | |
|---|---|
| $A$ | Area of the object |
| $A_1$ | amplitude in general solution of $\theta_2$ |
| $A_2$ | amplitude in general solution of $\theta_2$ |
| $c$ | speed of light, 299,792,458 m/s |
| $C_D$ | drag coefficient |
| $C_{Rd}$ | coefficients of diffuse |
| $C_{Rs}$ | coefficients of specular |
| $C_{Ra}$ | coefficients of absorption |
| $C_{eq}$ | equivalent damping coefficient |
| $[C]$ | damping coefficient matrix |
| $d$ | distance from the light source to the membrane |
| $\vec{F}_{tot,i}$ | summation of the internal and external force vectors on the $\text{i}^{\text{th}}$ lump mass |
| $F_{x\_tot,i}$ | total force acting on the $i^{\text{th}}$ lump mass in $x$ direction |
| $F_{y\_tot,i}$ | total force acting on the $i^{\text{th}}$ lump mass in $y$ direction |
| $\vec{F}_{tot,i}$ | internal force from the rotational damper and spring on $i^{th}$ lump mass |
| $\vec{F}_{\text{int},i}$ | internal force vector from the rotational damper and spring force vector on $i^{th}$ lump mass |
| $\vec{F}_{ext,i}$ | external force vector on $i^{th}$ lump mass |
| $\vec{F}_{spring}$ | rotational spring force vector |
| $\vec{F}_{damper}$ | rotational spring force vector |
| $\vec{F}_D$ | air friction |

| | |
|---|---|
| $\vec{F}_{\exp}$ | solar radiation force |
| $H_{i+1}$ | a matrix to convert state space into measurement space at $i+1$ |
| $I_{rad}$ | flux of radiation |
| $[K]$ | stiffness matrix |
| $K_{eq}$ | equivalent stiffness |
| $K_{i+1}$ | Kalman gian at $i+1$ |
| $L_{rod}$ | length of rigid rod $L_{rod} = L_1 = L_2$ |
| $[M]$ | mass matrix |
| $M_{tot}$ | total mass of a sample |
| $m_i$ | $i^{th}$ lump mass( $i$ = 1, 2 and 3) |
| $\hat{N}$ | normal unit vector |
| $\hat{P}_i$ | error covariance estimate matrix at $i$ |
| $\hat{P}_{i+1}$ | error covariance estimate matrix at $i+1$ |
| $\bar{P}_{i+1}$ | state covariance prediction at $i+1$ |
| $Q$ | process noise covariance |
| $R$ | measurement noise covariance |
| $\hat{S}$ | spotlight incidence vector |
| $\vec{T}_j$ | tension force vector generated by the $j^{\text{th}}$ rod ( $j$ = 1 and 2) |
| $\Delta t$ | discrete time of sequence image |
| $\hat{X}_i$ | state estimate vector at $i$ |
| $\vec{V}_i$ | velocity vector of lump mass ( $i$ = 1 and 2) |
| $\bar{X}_{i+1}$ | state vector prediction at $i+1$ |
| $\ddot{x}_i$ | acceleration in x direction of the $i^{\text{th}}$ lump mass |
| $x_1, y_1$ | the first lump mass |
| $x_2, y_2$ | the second lump mass |
| $x_3, y_3$ | the third lump mass |
| $\ddot{y}_i$ | acceleration y direction the $i^{\text{th}}$ lump mass |
| $Z_{i+1}$ | measurement vector |
| $\xi$ | damping ratio |
| $\Phi_s$ | error state transition matrix |
| $\omega_d$ | damped natural angular frequency |
| $\tau_d$ | damped vibration period |
| $\varepsilon$ | transmissivity efficiency of the glass window of the vacuum chamber |
| $\theta_{inc}$ | incident angle |
| $\theta_1$ | angle measured by the first rod ( $L_1$ ) direction in vertical axis |
| $\theta_2$ | angle measured by the second rod ( $L_2$ ) direction in vertical axis |
| $\dot{\theta}_1$ | angular velocity of $\theta_1$ |
| $\dot{\theta}_2$ | angular velocity of $\theta_2$ |
| $\ddot{\theta}_1$ | angular acceleration of $\theta_1$ |
| $\ddot{\theta}_2$ | angular acceleration of $\theta_2$ |

# 1

# 1 Introduction

This chapter presents an overview of space debris and impact hazards to satellites and the development history of orbital debris models. The discovery of High Area-to-Mass Ratio (HAMR) debris and their properties are then described. This is followed by state of the art review of the different methodologies and approaches developed for orbital motion prediction of HAMR debris. Finally, the research motivation, objectives and the thesis structure will be presented at the end of the chapter.

## 1.1 Space debris

Space debris is generally classified in two groups: natural (meteoroid) and artificial (man-made) particles by the Inter-Agency Space Debris Coordination Committee (IADC). As the results of 50 years of spaceflight, space activities have led to the increase in the number of the man-made objects from launchers (e.g. rocket upper stage, fairings, adapters etc.) and deployment of payloads (e.g. satellites and objects lost from astronauts ). In September 2012, the U.S. Space Surveillance Network (SSN) was able to track more than 23,000 objects with sizes larger than 10 cm and only one thousand of these were operational spacecraft. By extrapolation, objects larger than 1 cm could amount to over 750,000 pieces. However, scientists estimate that the total number of space junk objects larger than 1 mm to be more than 170 million. Due to the hypervelocity of debris, in the order of 2.8-8 km/s, even orbiting paint flakes can damage active satellites as shown in Figure 1.1. In order to investigate the damage brought on by small debris on a satellite a joint National Aeronautics and Space Administration (NASA) and European Space Agency (ESA) investigation was performed. The results in Figure 1.1(b) and Figure 1.1(c) are clear evidence of the critical risks to satellites from debris impact.

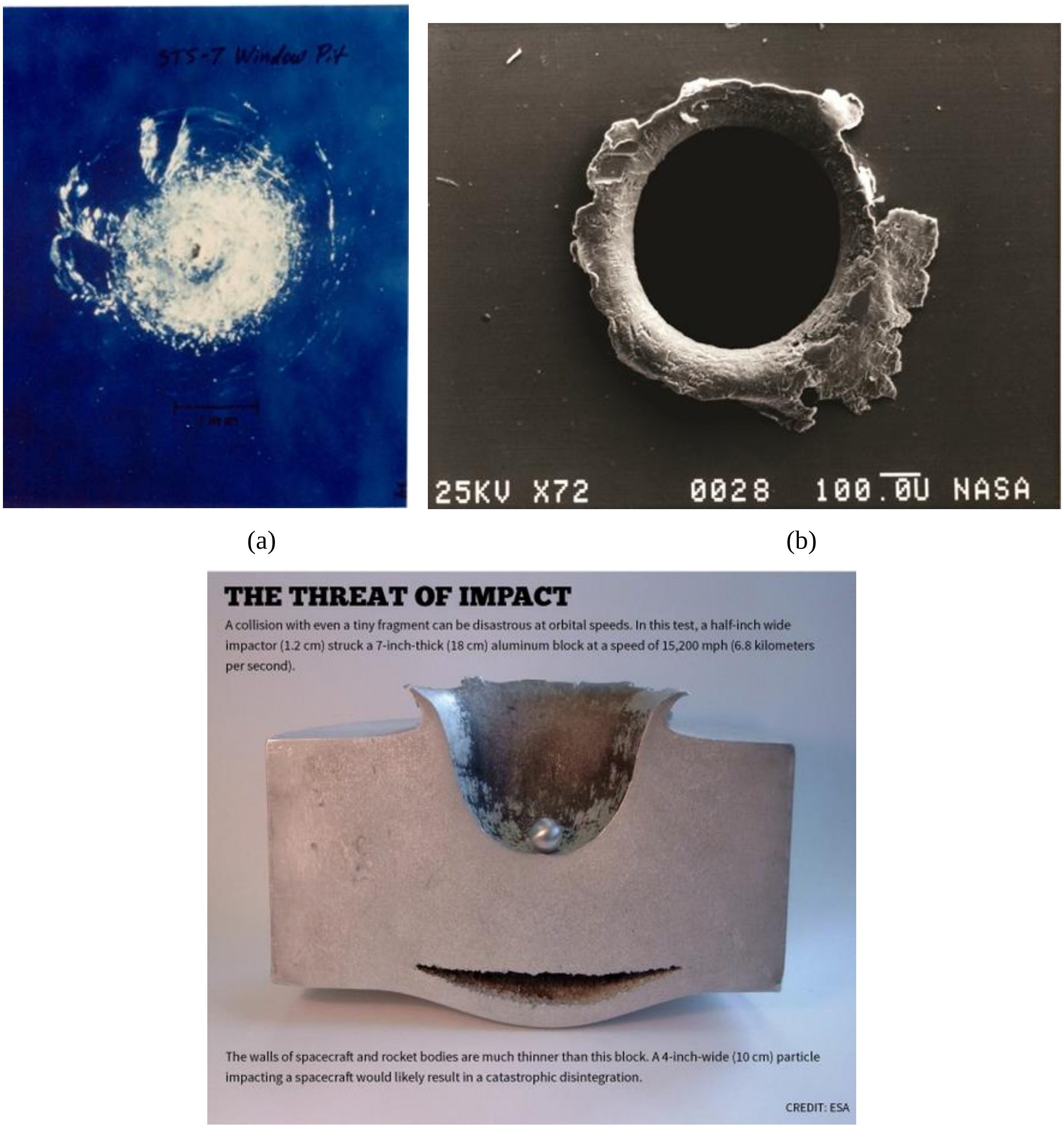

THE THREAT OF IMPACT

A collision with even a tiny fragment can be disastrous at orbital speeds. In this test, a half-inch wide impactor (1.2 cm) struck a 7-inch-thick (18 cm) aluminum block at a speed of 15,200 mph (6.8 kilometers per second).

The walls of spacecraft and rocket bodies are much thinner than this block. A 4-inch-wide (10 cm) particle impacting a spacecraft would likely result in a catastrophic disintegration.

(a) (b)

(c)

**Figure 1.1: Damage image detection from NASA. (a)A tiny piece of space junk (a paint fleck) damaged the window of the space shuttle during the STS-7 mission (Photo: the NASA Orbital Debris Program Office (ODPO)) (b) The image is from the orbital debris hole made in the panel of NASA's Solar Max experiment. (c) A damage from collision with a tiny fragment with high speed of 6.8 km/s from ESA.**

Figure 1.2 reports the time evolution of the catalogued space debris objects from 1956 to 2013. This latter classification clearly shows that the fragments resulting from breakups are a major of the total populations. Two spikes can be clearly noticed in 2007 and 2009. In January 2007, a direct-ascent anti-satellite (ASAT) vehicle [1] was successfully tested by destroying an inactive Chinese Fengyun 1C (FY-1C) weather satellite. This impact generated more than 2,300 pieces of trackable debris and about 1 million pieces of 1 mm larger more debris than any previous space incident. In February 2009, the defunct Russian military satellite, Cosmos, collided into one of the active U.S. communications satellite, within the Iridium constellation, at 790 km above Siberia [2].

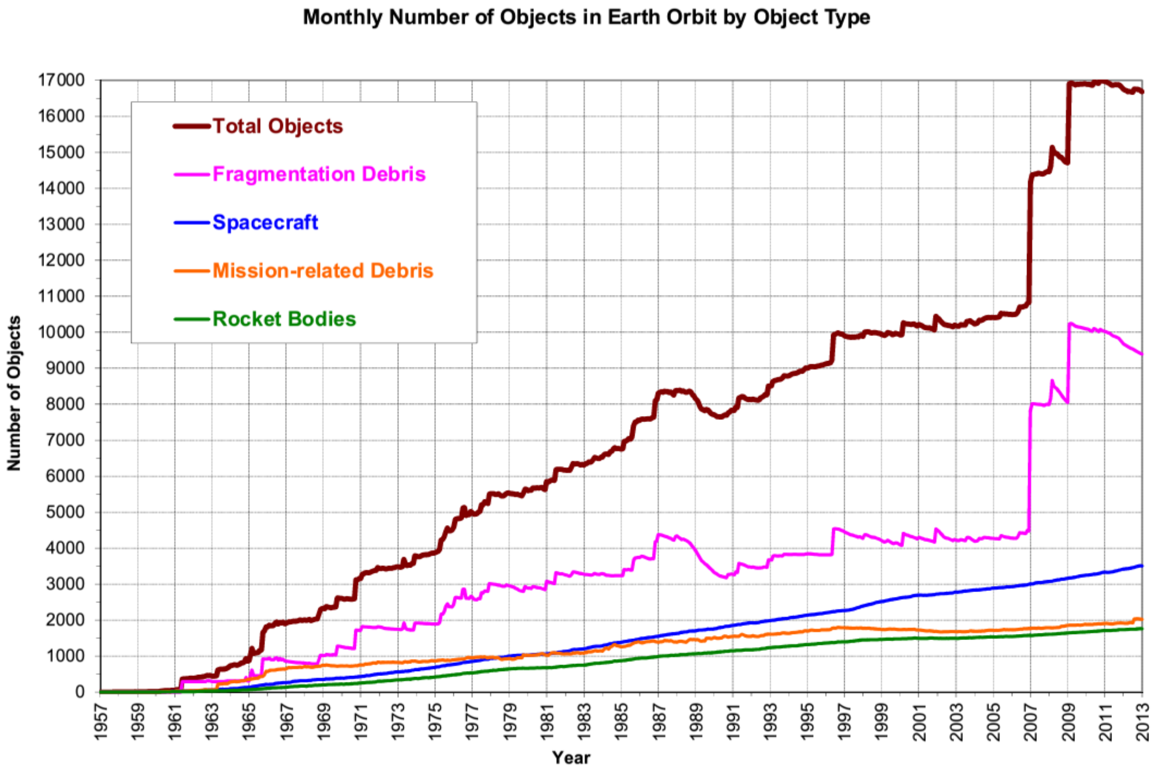

**Figure 1.2 Number of Catalogued objects in Earth orbit by Object Types: This chart shows a summary of all objects in Earth orbit officially catalogued by the U.S. Space Surveillance. Fragmentation debris includes satellite breakup debris and anomalous event debris while missions-related debris includes all objects dispensed, separated, or released as part of the planned mission. [Orbital Debris Quarterly News, January 2013].**

Both events generated the worst satellite breakups in history. The SSN reported that a total of 5579 had orbited into Low Earth Orbit (LEO) but over 5000 pieces were still at their impact orbits in January 2013. The major of fragment decays were from the Iridium 33 and Cosmos 2251 because of their lower altitudes. Comparing the orbital lifetime of the debris from Iridium 33 and Cosmos 2251, the former had shorter lifetime than the latter due to the use of lightweight composite materials in the construction of the Iridium spacecraft, which have higher Area-to-Mass ratio (AMR) properties. In addition, some of thousands of fragments down to the millimetre size regime could not be tracked by the SSN. These tiny fragments are however still large enough to pose a risk to human space activities due to their very high velocities.

Following the exponential growth of debris objects, there may occur an unbalance between the rate of production from collisions and the decay rates. This scenario is called “Kessler syndrome” from NASA’s Donald Kessler who, in 1968, suggested a scenario in which the amount and density of debris in low-Earth orbit reaches a critical mass resulting in a cascading and stochastic debris environment, creating an increasingly greater likelihood of collisions. In Figure 1.3, it shows NASA generated computer images of orbital debris currently being tracked in Low Earth Orbit and Geostationary Earth orbit (GEO). Currently, there are loose international guidelines, set forth by the NASA and ESA, which set the requirements for the deorbiting of spacecraft in LEO within 25 years of launch. These guidelines have been developed to mitigate the possible exponential growth in the number of man-made space objects.

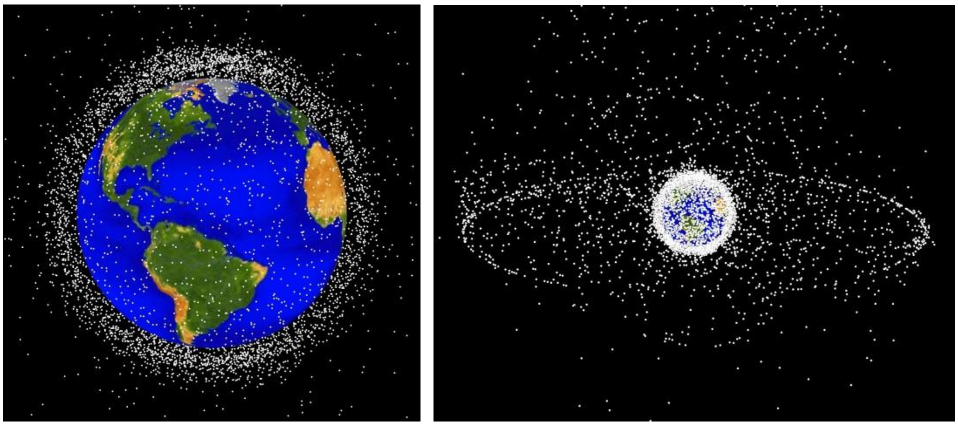

**a)** **b)**

**Figure 1.3 Image of space junk surrounding Earth by computer from NASA Orbital Debris Program Office (a) LEO (b) GEO.**

## 1.2 Development of orbital debris models

The NASA Orbital Debris Program Office (ODPO), established since the 1970s, has undertaken to conduct a measurement of the space environment (e.g. observation data of collision and explosions of spacecraft and upper stages) to understand the nature of the predicted debris environment. The first model developed was the Evolutionary debris environment model, EVOLVE, which was capable to describe a one-dimensional model of the orbit debris in LEO environment between 200 and 2000 km. As well as serving as stand-alone models for simulating the initial characteristics of debris clouds in Earth orbit, the breakup model critically affects the output of NASA's long-term satellite population environment model. This model is able to provide the estimation of size distribution, AMR and velocity distributions. The current version, EVOLVE 4.1 [3, 4], is updated with the database of observation data and the validation of debris size in range from 1 mm to 10 cm of debris test by Anz-Meador [5]. In addition, the standard breakup model in EVOLVE would encounter problems when the debris quantity from collision was more than a few hundred pieces. Li Yi –Young [6] presented a faster and more precise algorithm for calculating the debris cloud orbital lifetime and characterisation from spacecraft collision breakup.

In order to investigate the orbit debris in GEO, "GEO EVOLVE 1.0" was developed by ODPO in 1999. This was the GEO region version of EVOLVE 4.0 and the first attempt by NASA to simulate the GEO environment. Initially, there was no information on the actual position of the GEO object and the model estimated the probability of a future collision event through a spatial density representation of two objects within a box that included the region of mutual orbital crossing. This effected to slow precession of the node and argument of perigee in GEO. Therefore, a new model to improve the overestimation of the future collision rate in GEO was required. The GEO EVOLVE 2.0 [7] was developed in 2004, to address two main issues. Firstly, the development traffic database was upgraded to include more parameters such as insertion node, argument of perigee and mean anomaly of all launches from 1957 to 2001. Secondly, two new orbital propagation codes (GEOPROP and PROP3D) take into account orbital perturbations: atmospheric drag, lunar gravitational orbital perturbation, solar radiation pressure perturbation, Earth gravity-field zonal ($J_2$, $J_3$ and $J_4$) and tesseral ($J_{2,2}$ , $J_{3,1,}$ $J_{4,2,}$ $J_{4,4}$) harmonics perturbations and the Earth's shadow effects, as well as including more precise fragment area-to-mass estimation from improved observation data**.**

Motivations to develop a new model of replace EVOLVE hinge on two reasons. Firstly, a one-dimensional description in altitude of the debris environment is inadequate to address all issues. Secondly, with an increasing number of space debris, there was a requirement to build a full-scale debris mode to describe the near-Earth environment from Low Earth Orbit to Medium Earth Orbit (MEO) and to Geostationary Earth Orbit above. These concerns were addressed with A LEO-to-GEO Environment Debris model, (LEGEND) [8, 9]. This model is capable of describing debris characteristics (e.g. size distribution, spatial density distribution, velocity distribution, flux etc.) as functions of time, altitude, longitude and latitude. Moreover, LEGEND was updated with a historical simulation component (1957-2001). However, all debris in these models are assumed to be rigid object.

In 1995, ESA developed an orbital debris model called “Meteoroid And Space Debris Terrestrial Environment Reference model” (MASTER) [10]. This model was introduced to analyse space debris flux and spatial densities in a 3D control volume spanning from LEO to GEO debris larger than 0.1 mm. The debris originated from explosion and collision fragments, dust, solid rocket motor, lunches and mission-related objects, meteoroids and surface degradation products, were observed by the Tracking & Imaging Radar (TIRA), European Incoherent Scatter Scientific Association (EISCAT), Goldstone and Haystack radars, the ESA Space Debris Telescope (ESASDT) and Database and Information System Characterising Objects in Space (DISCOS). In 2004, the debris surveys uncovered and unexpected debris population [11, 12]. These objects presented highly eccentric orbits rapidly changing orbit parameters, and varying brightness. The possible sources of these objects were suspected to be thermal insulation or multilayer insulation (MLI). Flegel [13] investigated the orbital dynamics of this debris type and concluded that it was a rigid object with effective cross-sectional area ( $A_{eff}$ ), considering the maximum surface of the object ( $A$ ), times a product of three coefficients ( $A_{eff} = A \cdot D_{reflectivity} \cdot D_{deformation} \cdot D_{tumbling}$ ) that were modelled by the reduction in cross-sectional area due to tumbling ( $D_{tumbling}$ ), deformation ( $D_{deformation}$ ), and finally actual reflectivity ( $D_{reflectivity}$ ). A uniform distribution of values of the coefficients within their respective bounds was used for the propagation of the debris objects and then integrated and propagated in MASTER (version 2009). The predicted results compared well with the observations of the GEO region.

## 1.3 Discovery of High area to mass ratio (HAMR)

As mentioned above a new population of uncatalogued objects in GEO was detected in 2004 [11, 12]. This first observation, acquired in the framework of the European Space Agency (ESA) for space debris in GEO and in the Geostationary Transfer Orbit (GTO), was discovered by the Astronomical Institute of the University of Bern (AIUB). New HAMR objects were then detected by the one metre ESA Space Debris Telescope (ESADAT), located in Tenerife, Spain, and the one meter Zimmerwald Laser and Astrometry Telescope (ZIMLAT), in Switzerland. Earlier studies had shown that the characteristics of HAMR debris were large eccentricity and inclination due to solar radiation pressure (SRP) effect and the orbital evolution of these objects significantly differs from debris with low AMR. The characteristics of the debris light curve were then used to determine the sizes, attitude motion and possible composition of the HAMR objects. The light curve investigations by Früh [14] indicated that brightness of cannonball objects and rigid sheet objects clearly showed different brightness. The very rapid attitude motion due to SRP torque resulted in rapid brightness changes [15]. All current observed data of HAMR objects [16] have been collected several years and suggest that HAMR objects vary their AMR values throughout their orbital motion. It is also worth noting that they can change their geometry (deformation) over time.

In further investigations, Liou [17] studied the orbital dynamics of this kind of debris from the same initial data as Schildknecht. It is thought that this debris originates from thermal blankets or MLI. The “thermal blanket” is used to cover all major external surfaces of a typical spacecraft as well as individual components to minimize heat transfer by separating the individual layer either by spatial separation or by insertion of low conductance spacer material. Multiple layers of thin, metalized substrate materials are combined from insulating blankets as shown in Figure 1.4. The basic substrates are extremely thin layers of PET® (Polyethylene terephthalate), Kapton® and Teflon®. These substrates, are coated with very thin metal (aluminium, gold or silver on one or both sides of substrate), have a thickness in the order of 1000 Ǻ, are very lightweight and flexible and have low outgassing properties under vacuum environment. For example, AMR of PET® can have an AMR of 111.11 $m^2$/kg. The satellite bus may be covered by more than 20 layers while a sun shield for radio frequency antenna typically consists of less than five layers of MLI [18].

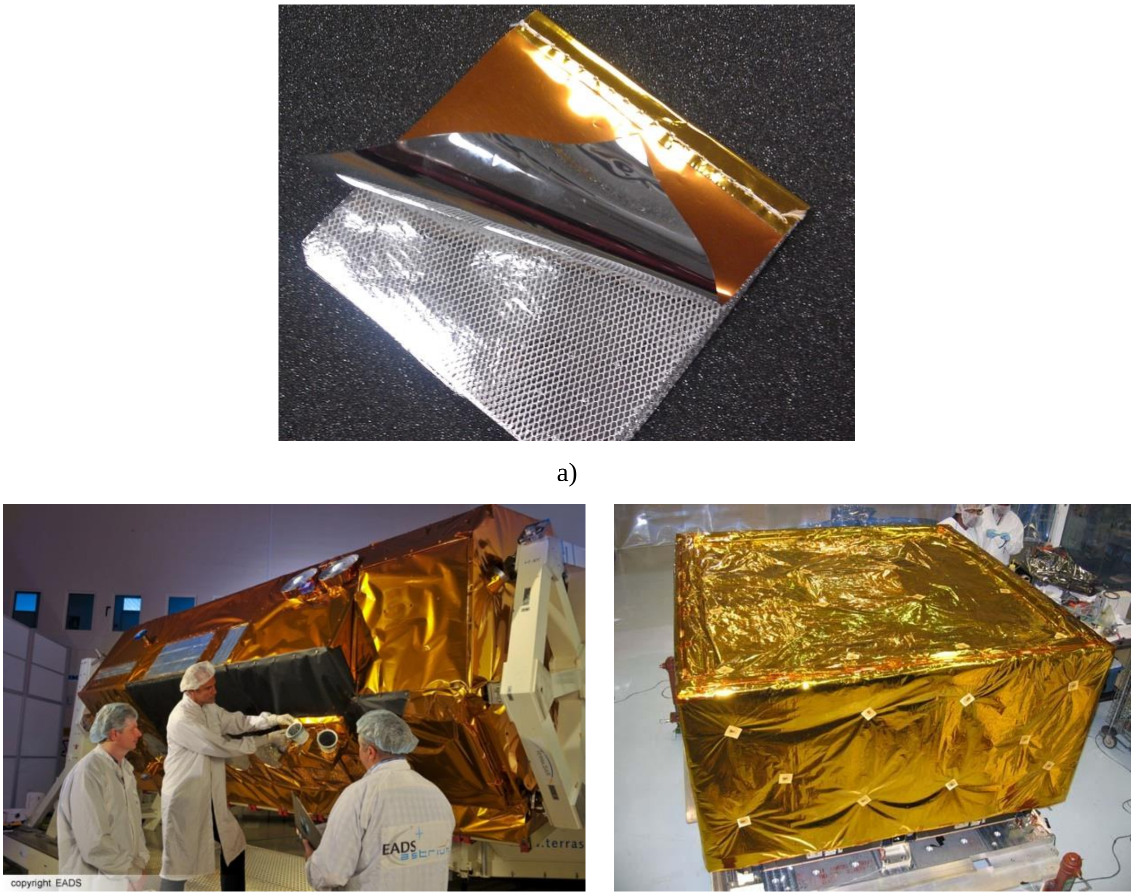

a)

b) c)

**Figure 1.4 Multilayer insulation installed with real applications a) MLI Film sample from Dunmore b) Multilayer insulation blanket to the Thermal Infrared Sensors (TIRS) for Landsat satellite for the Landsat Data Continuity Mission (LDCM) from NASA website c) Multilayer Insulation Installed on Anticoincidence Detector (ACD) and the MicroMeteoroid Shield (MMS) from NASA website photo credit: Diane Schuster.**

This hypothesis seems to be backed by anecdotal evidence as observation of the Hubble space telescope in 1998, found the degradation of Fluorinated Ethylene Propylene (FEP®) surface of the MLI around the telescope [19]. Moreover, recent results of a statistic orbital decay analysis of the AMR distribution from Fengyun-1C breakup [20] have been shown that about 5% of the catalogued fragments have AMR $\geq 1$ $m^2$/kg and around 1% have AMR $> 10$ $m^2$/kg (reaching to 90 $m^2$/kg). This spread is very similar results that of the Cosmos 2252 fragment collision. However, the larger HAMR fragments generated by the Iridium 33 resulted in a faster debris decay and reentry of 26% of the catalogued fragment for AMR $\geq 1$ $m^2$/kg and 5% for AMR $\geq 10$ $m^2$/kg as shown in Figure 1.5.

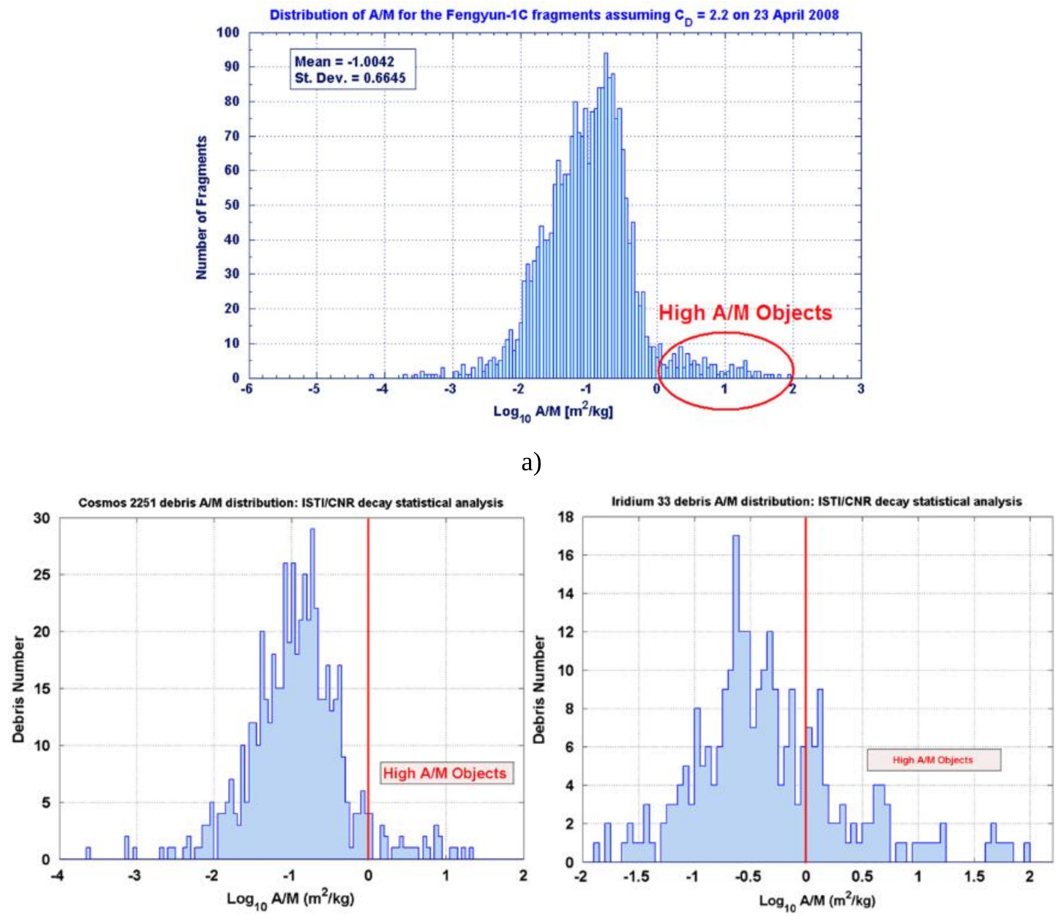

a)

b) c)

**Figure 1.5 Area-to-Mass Ratio distribution inferred from a statistical orbital decay analysis a) Fengyun-1C b) Cosmos 2251 c) Iridium 33 Anselmo, L., et al. [20, 21].**

In order to investigate the fragments of DebrisSat (DS) from an explosion of a spacecraft [22, 23], Murakami experimented by shooting an aluminium alloy solid sphere (30 mm, approximately 40 grams) through a satellite in two different areas as shown in Figure 1.6. The results of experiment can be seen in Figure 1.7. Figure 1.8 shows that MLI is the HAMR among other objects. The classification of debris with AMR from Murakami’s experiments supported the thesis that MLI could possibly be one of the sources of HAMR objects.

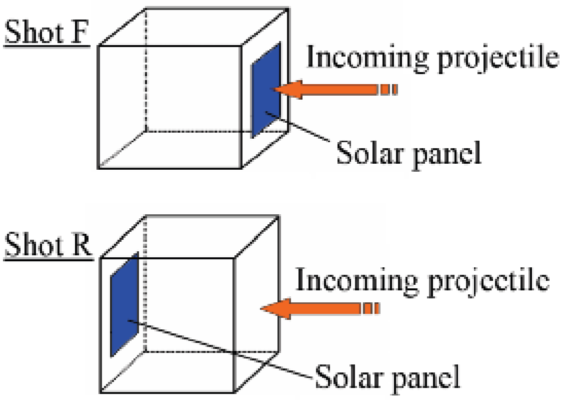

**Figure 1.6 Shot F that shot through solar panel before. Shot R that was shot opposite side of the solar panel (Graphic by Murakami, J., et al. [23]).**

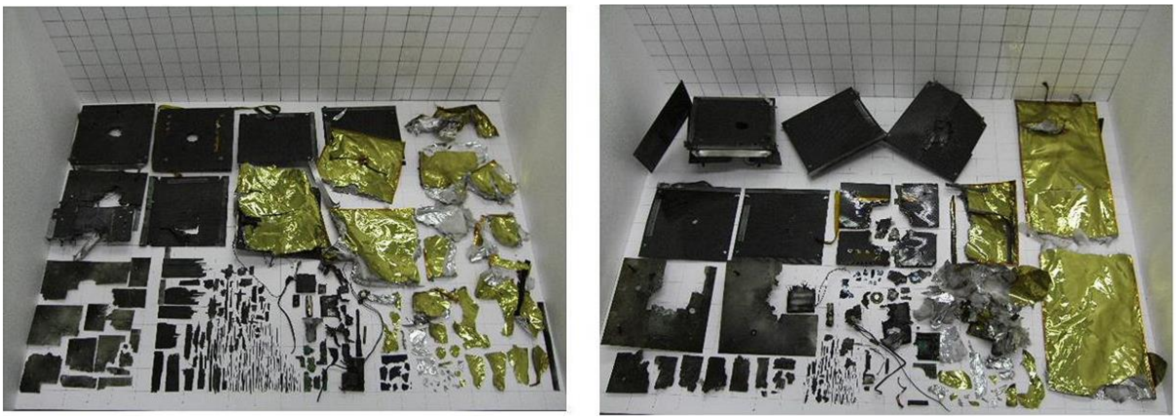

a) b)

**Figure 1.7 Overall of fragments a) Shot F b) Shot R[23].**

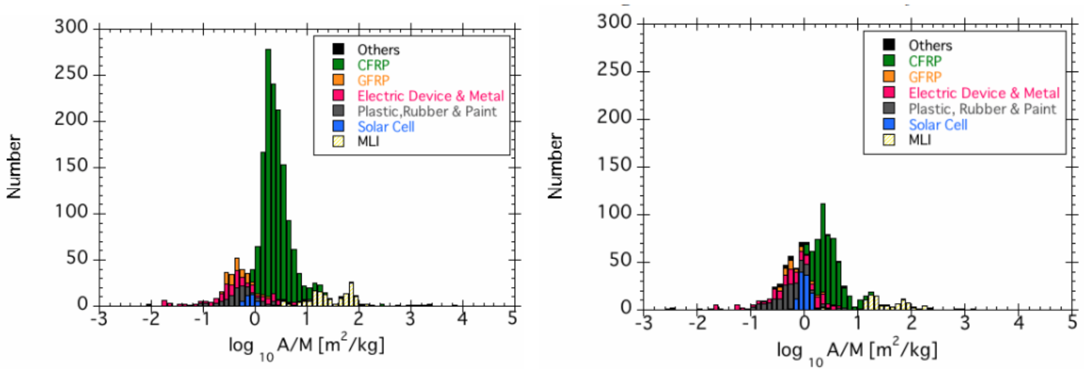

**Figure 1.8 Area to mass ratio from shot a) Short F b)Shot R (Graphic by Murakami, J., et al. [23]).**

### 1.3.1 The investigation of orbital dynamics of High Area-to-Mass Ratio debris

Having identified the HAMR debris population, the efforts were then focused on the investigation of the long term orbital dynamics under perturbations (solar radiation pressure and luni-solar third body attraction). Initially, the HAMR objects are assumed follow a simple cannonball model, which allows to neglect attitude motion and varying AMR values.

Firstly, Liou [17] studied the orbital dynamics of HAMR objects in GEO using two numerical solvers: SPCM and PROP3D high fidelity orbit integrators based on Encke's method. The coefficient of reflectivity, $C_r$ (dimensionless radiation pressure coefficient), of the surface was considered to study the eccentricity and inclination evolution over extremely long periods by Anselmo [21]. Results showed that the $C_r$ as a function of the AMR affected the variation of inclination. Another study of the orbital motion by Valk [24-26] applied a Hamiltonian formulation of averaged equations of motion to develop a semi-analytical theory for this type of debris over short-, mid- and long-term orbital motion in GEO environments, which included the Earth shadow effect (cylindrical model). This approach was faster than traditional numerical integration and much more accurate than analytical theories. All investigations agreed that the amplitude of inclination was proportional to the AMR values and the resulted in periodic significant changes in term of eccentricity.

In conclusions, all the above studies approximated HAMR debris to the cannonball model, which treats the object as a sphere with constant reflection properties and ignores the coupling of orbital dynamics with attitude dynamics.

### 1.3.2 Coupled attitude and orbital dynamic and light curve

In order to improve the accuracy of orbital prediction of HAMR debris, Früh analyzed the coupled attitude and orbital motion of GEO HAMR debris over short time periods [14]. In this study, MLI objects were assumed to be a single sheet of MLI in a different geometry (flat plate or curled plate) and the substrate of MLI materials are assumed to be PET® and Kapton®. The equations of motions were modelled under full GEO environment (gravitational field, direct solar radiation pressure, Earth magnetic field and the influence of the Earth shadow effect). The result demonstrated that rapid attitude motion due to solar torque led to significant changes in the eccentricity and inclination of the orbits when compared with the cannonball model. Furthermore, the self-shadowing effect by means of the tessellation technique [27] provided further changes to both attitude and orbital elements evolution. Coupling the attitude and orbital dynamics was shown to improve the accuracy prediction of the debris orbital evolution.

However, the oversimplification of a rigid body due to assumption of a constant AMR value (no deformation) led to inaccurate propagation of the orbital dynamics for this debris type [14]. This is supported by the studies on AMR variation of the HAMR debris by Musci and Früh [16, 28]. The results of the observations suggest a complicated attitude motion and deformation of the debris, which results on an actual change in the AMR values over time. In addition, the investigation from Sakva [29], which compared the observation data of a known object with simulation results based on cannonball model, showed that the SRP cannonball model was not appropriate for either short or long term orbit prediction of HAMR objects.

McMahon [30] studied the solar radiation effects on HAMR objects with varying geometries. The HAMR model was capable of assuming one of five configurations as shown in Figure 1.9. The basic idea behind this work is that as the object increases its spin rate, it would relax into an increasingly flatter shape. The debris would then behave as a perfectly flat rigid object (Figure 1.9(c)). The results of this study agreed with previous investigations [17, 24-26, 31] in that SRP can induce very fast tumbling. There are however some limitations with this work most notably that the deformed mode requires integration time steps several orders less than those typical of orbital motion and hence long term propagation becomes exceedingly expensive in computational terms. Additionally, this model does not behave like a continuously deformed object but only as a discrete set of 5 possible configurations.

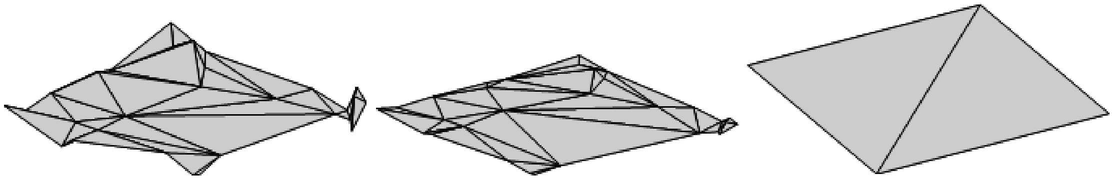
a) b) c)

**Figure 1.9 Show some changing shape moving from the initial geometry a)1st shape(initial shape) b) 4th shape c) 5th shape(flat pate) [30].**

## 1.4 Research motivation and objectives

A new debris type was discovered in 2004 with HAMR, reflection properties, fast tumbling and significantly perturbed orbital motions in GEO environment [11, 12, 16, 32]. Following detailed observations and laboratory-based analysis, it is believed that these objects could be MLI pieces that delaminated from spacecraft due to aging, explosions or collisions [19, 22, 23].

The orbital evolutions of HAMR objects by approximation through the cannonball model, with constant AMR and no consideration for attitude motion, have been studied in GEO under perturbations over short and long term periods. The orbital dynamics of HAMR objects are highly perturbed due to direct solar radiation pressure and even small changes in the effective AMR, which can lead to significant changes in the orbital evolution [17, 24-26, 31]. However, observations indicated that the AMR values change over time and hence the objects exhibit rapid attitude changes. This means that more accurate HAMR modelling is required to consider the 6 Degrees of Freedom (DoF) motion by coupling orbital and attitude dynamics. The SRP torque will be responsible for the fast attitude dynamics of this debris type. Additionally, a more accurate model of the varying shape of the HAMR debris will provide a more precise prediction because of more the better modelling of the SPR effects on the object. It is therefore desirable to model a simple yet effective, flexible model that can account for variations of the cross-sectional area while keeping the computational complexity low. This model will be a more accurate long term orbital prediction [14, 27, 30, 33].

In recent studies by Channumsin et al.[34, 35], the HAMR debris is modeled as a simple, flexible model based on finite element method and multibody dynamics. Both models are able to adapt to a continuous changing shape. The results of this investigation have shown irregular and fast rotation including each time step of the propagation. Solar radiation pressure significantly perturbs the orbital dynamics, generates unstable attitude motion and leads to deformation of the geometry of the object. In order to validate these flexible model two experiments performed in a vacuum chamber to reduce air friction, have been carried out. The first experiment allowed the determination of the bending stiffness and damping ratio of the membrane by means of free motion. Then, forced motion is achieved by exposing the membrane to high power spotlight, representing SRP, and measuring the displacement. The experimental results show a good agreement with the numerical simulations of the multibody model, and FEA model.

In summary, the main objectives of this doctoral thesis are the following:

**1. Development of a simple yet effective model for flexible debris**

- Develop a model flexible debris based on Finite Element Method and multibody dynamics

- Investigate the orbital dynamics of flexible debris under GEO perturbations (Earth gravitation, luni-solar third body attractions and solar radiation pressure) and compare the results with a rigid model.

- Investigate the attitude and orbital dynamics as well as varying geometry of the flexible model under self-shadowing effect.

**2. Validations of the flexible model**

- Design and perform an experiment to determine the damping ratio of a real multilayer insulation membrane.

- Perform an experiment to simulate solar radiation pressure displacement and compare the results with the analytical methods (multibody dynamics, normal mode theory and Finite Element Analysis (FEA).

## 1.5 Thesis structure

This doctoral thesis is divided into six main chapters that cover different aspects of the study. The main goal of this thesis is to develop and a simple yet effective, model of flexible, low strength debris. The orbital dynamics of the new model are then compared to the classic model, based on rigid object and cannonball assumptions. Experimental data will then be used to validate the analytical models.

Chapter 2 is to model the coupling of orbital and attitude dynamics of a rigid object. Orbital motion subject to environmental perturbations from the Earth’s gravitation, third body perturbations (Sun and Moon) and solar radiation pressure in GEO environment are presented in this chapter. The simulated section presents the orbital dynamics of the cannonball model (neglecting attitude motion) and flat rigid plate (coupled attitude and orbital motions).

Chapter 3 introduces a simplified but effective model to represent the deformation flexible HAMR debris, subject in particular to torques caused by solar radiation pressure and the Earth gravitational field, by means of Finite Element Method (FEM). This model adds a further set of dynamical equations, which accounts for the flexibility of the object, into the attitude and orbital equations; the resulting system is then numerically integrated to better evaluate the coupling between orbital and attitude dynamics. Due to a more precise estimation and prediction of the actual shape and orientation of the debris at any given time than by simply assuming the case of a rigid body, the effects of the perturbations on the orbit can be computed more precisely leading to improvements in the long-term prediction of the orbital evolution. Results show that the eccentricity changes of flexible debris are different than for equivalent rigid bodies and their attitude motions are unique.

Chapter 4 presents a flexible model as a series of lump mass, connected through flexible joints, representing the flexibility of the membrane itself. The mass of the membrane, albeit low, is taken into account with lump masses in the joints. The equations of motion, including the constraints defined by the connecting rigid rod, are derived using fundamental Newtonian mechanics. The physical properties of the objects required by the model (membrane density, reflectivity, composition, etc.), are assumed to be those of real multilayer insulation. This flexible membrane model is then propagated together with classical orbital and attitude equations of motion near a GEO region to predict the orbital evolution under the perturbations of solar radiation pressure, Earth gravity field, luni-solar third bodies and self-shadowing effect. Firstly, when comparing with a rigid model, the orbital elements over 12 days of are significantly different. The second study, a Monte Carlo simulation over 100 days with varying initial attitude dynamics (yaw ($\psi$), pitch ($\theta$), and roll ($\phi$)) and deformation angle ($\theta_d$) leads to significantly different orbital motion.

Chapter 5 presents a methodology to determine the dynamic properties of thin membranes with the aim to validate the deformation of the flexible model. Experiments are performed in a high-vacuum chamber ($10^{-4}$ mbar) to significantly decrease air friction, inside which a thin membrane is hinged at one end but free at the other. A free motion test is used to determine the damping characteristics and natural frequency of the thin membrane via logarithmic decrement and frequency response. The membrane is allowed to freely swing in the chamber and the motion is tracked by a static camera. A Kalman filter technique is implemented in the tracking algorithm to reduce noise and increase the tracking accuracy of the oscillating motion. Then, the effect of the solar radiation pressure on the thin membrane is investigated: a high power spotlight (500-2000 W) is used to illuminate the sample and any displacement of the thin membrane is measured by means of a high-resolution laser sensor. Analytic methods from the natural frequency response and Finite Element Method including multibody simulations of both experimental setups are used for the validation of the flexible model by comparing with the experimental results of amplitude decay, natural frequencies and deformation. The experimental results show good agreement with finite element methods.

Chapter 6 concludes the overall of outcomes of this thesis. In the end, this chapter describes limitation of this thesis and future research plans.

# 2

# 2 Orbital dynamics of rigid object

The main objective of this chapter is to investigate and compare the orbital dynamics of HAMR rigid objects (cannonball and flat plate) under conservative perturbations from the Sun, Moon and Earth gravitations and non-conservative perturbations from solar radiation pressure (SRP) over short term and long term periods in the GEO region. Section 2.1 presents the fundamental concepts of orbital motion and perturbing accelerations relevant to this study. Section 2.2 and 2.3 describe the attitude dynamics rotational kinematics respectively while section 2.4 provides the integration approach to the propagation of the equation of motion. Finally, section 2.5, presents and discusses the results.

## 2.1 The perturbed equation of motion

The general equation of orbital evolution per unit mass, under perturbations in GEO environment can be expressed in Cartesian coordinates as:

$$\ddot{\vec{r}}_{tot} = \vec{a}_{\oplus} + \vec{a}_{\odot} + \vec{a}_{☾} + \vec{a}_{SRP} \tag{2.1}$$

Where $\ddot{\vec{r}}_{tot}$ is the total acceleration vector of the object, $\vec{a}_{\oplus}$ is the acceleration from the Earth gravity, the perturbing accelerations of $\vec{a}_{\odot}$ and $\vec{a}_{☾}$ are the results of the third-body attraction induced by the Sun and Moon respectively, $\vec{a}_{SRP}$ is induced by the solar radiation acceleration.

### 2.1.1 Two-Body Problem

Newton’s law of gravitation determines that every point mass attracts every single point mass by a force, which is proportional to the product of the two masses and inversely proportional to the square of the distance between them. In this research, we focus on the natural debris orbiting around the Earth. The force of gravity acting on the object from the Earth is written as:

$$\vec{F}_{\oplus} = \frac{-(GM_{\oplus} m_{obj})}{r^2}\left(\frac{\vec{r}}{r}\right) \tag{2.2}$$

Where $m_{obj}$ is mass of the debris, $M_{\oplus}$ is the mass of the Earth (5.9742×$10^{24}$ kg), $G$ is the universal gravitation constant (6.67259×$10^{-11}$ $m^3/kg/s^2$), $\vec{r}$ is the position vector of the debris in an Earth Centred Inertial (ECI) frame (inertial frame of this dissertation $(\hat{I},\hat{J},\hat{K})$).

As the mass of the debris ($m_{obj}$), is significantly less than the mass of the Earth, $m_{\oplus}$. Then, the quantity of $Gm_{\oplus}$ can be replaced with the Earth gravitational constant ($\mu$ =3.986×$10^5$ $km^3/s^2$). The relative acceleration can be therefore written as:

$$\ddot{\vec{r}} = -\frac{\mu}{r^2}\left(\frac{\vec{r}}{r}\right) \tag{2.3}$$

## 2.1.2 Luni-solar perturbation

For a debris orbiting in GEO regions, the main third-body gravitational perturbing forces acting on the space debris are the Sun and Moon as shown in Figure 2.1.

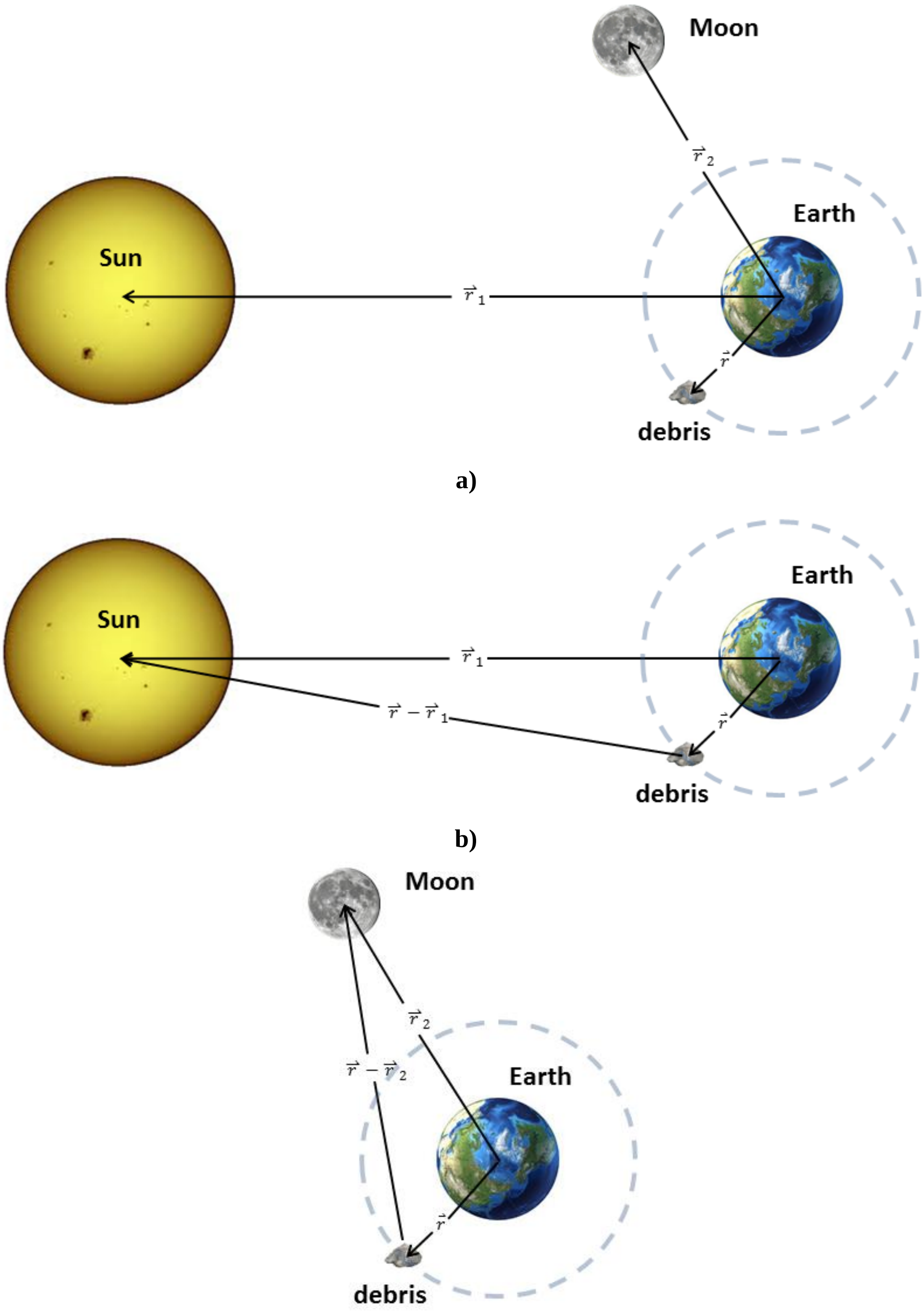

**a)**

**b)**

**c**

**Figure 2.1 Geometry the for third bodies in an reference frame a) Geometry of the Sun and Moon b) Geometry of the Sun vector c) Geometry of the Moon vector.**

The accelerations of the third body gravitational perturbations from the Sun and Moon [36] are given by:

$$\ddot{\vec{r}}_k = -\mu_k \frac{\vec{r}-\vec{r}_k}{\left\|\vec{r}-\vec{r}_k\right\|^3} \tag{2.4}$$

Where $\vec{r}$ is the ECI position of the space debris, $\vec{r}_k$ is the position vector of the third body (the subscript of $k$ $(k=1,2)$ are the Sun and Moon respectively (Note: the position vector from the Earth to the Sun and Moon changing over time are required because it is important to calculate both third body gravitational perturbations and solar radiation pressure. It is been described in Appendix A), the quantity $\mu_k = GM_k$ is the gravitational constants of the third body from the Sun and Moon ($\mu_1$= 1.32712438x$10^{20}$ $m^3/s^2$ and $\mu_2$ = 4.902794x$10^{12}$ $m^3/s^2$ respectively), $M_k$ is the third body mass of the Sun and Moon respectively ($M_1$= 1.9891×$10^{30}$ kg and $M_2$= 7.348×$10^{22}$ kg). Eq.(2.4) cannot be used directly for describing the motion of space debris with respect to the centre of the Earth. It is required to add the another term as:

$$\ddot{\vec{r}}_k = -\mu_k \frac{\vec{r}_k}{\left\|\vec{r}_k\right\|^3} \tag{2.5}$$

As a consequence, the acceleration of the space debris expressed with respect to the Earth's centre of mass is given as:

$$\ddot{\vec{r}}_k = -\mu_k \left( \frac{\vec{r}-\vec{r}_k}{\left\|\vec{r}-\vec{r}_k\right\|^3} - \frac{\vec{r}_k}{\left\|\vec{r}_k\right\|^3} \right) \tag{2.6}$$

The first term of the third-body perturbation is known as the *direct effect* and the second term is the *indirect effect* accounting for the inertial acceleration of the ECI frame. In this doctoral dissertation, the starting date of all simulations is January 1, 2012. Figure 2.2 shows the Sun and the Moon positions in ECI coordinates. The Sun and Moon vectors are scaled 1000 and 10 times respectively.

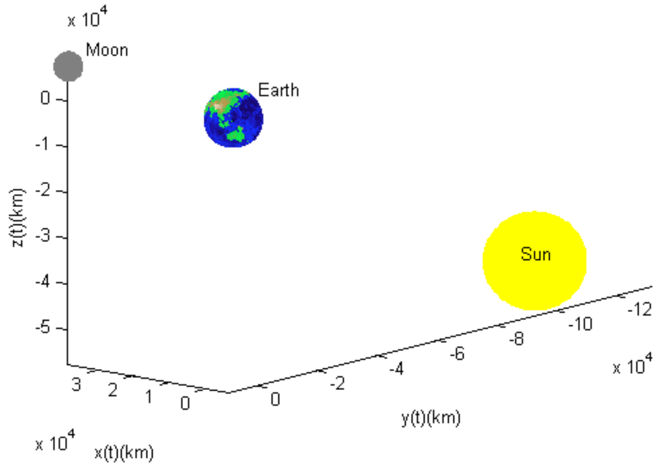

**Figure 2.2 The Sun and Moon positions in ECI frame on January 1, 2012 by scaling of the sun and moon vectors 1,000 and 10 times respectively.**

### 2.1.3 Solar Radiation Pressure

Solar radiation pressure caused by the incident ray of light from the Sun is a non-conservative perturbation. For HAMR object, this perturbation in GEO is dominant perturbation while the Earth radiation, thermal forces effect and atmospheric drag can be negligible in that altitude [11, 12, 17, 37, 38]. The model of SRP acceleration depends on many factors. Firstly, the solar flux generally varies throughout the year and over the 11 years solar activity cycle. In all the numerical simulations through this dissertation, the solar flux is assumed to be constant ($E$ = 1,353 W/m$^2$) [36]. Secondly, the reflective properties of material will directly affect how much force of SRP imparts on the debris. Thirdly, the cross-sectional area of the space debris is directly proportional to the solar radiation pressure force. In addition, the development of an accurate SRP model should also include the correct position of the Sun with respect to the object and the Earth.

In this chapter, we assume the HAMR debris to be a flat rigid plate and the SRP perturbation will include absorption and reflection of the solar radiation solar on an effective cross-sectional area ($A_{eff}$) as shown in Figure 2.3. The solar radiation incident shows the incident angle ($\theta_{inc}$) defined as the angle between the normal unit vector ($\hat{N}$) and the sun unit vector ($\hat{S}$) defining the direction from the Sun to the debris surface.

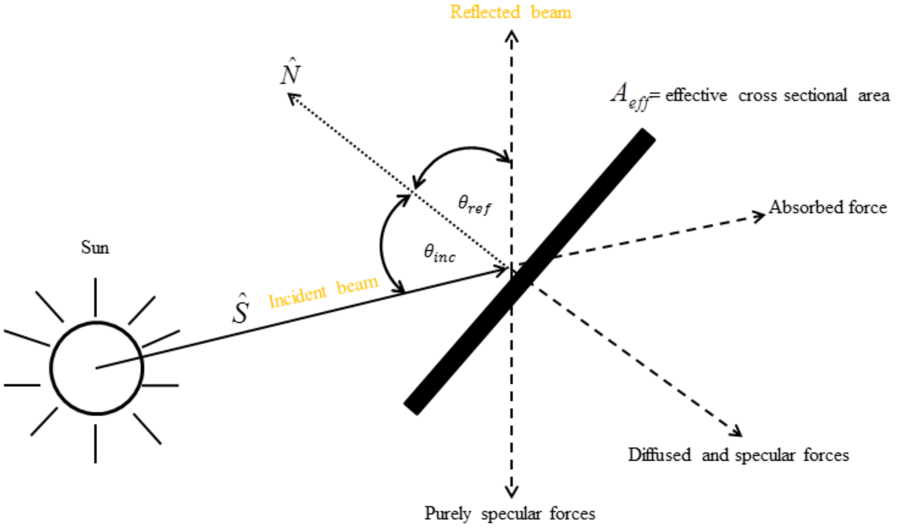

**Figure 2.3 The incident angle between the normal vector and the sun vector. Geometry of the incident, reflected, diffused and absorbed radiation.**

The SRP perturbing acceleration expressed by means of the Lambertian diffusion to model the diffuse and specular solar radiation forces that expose on a space debris [39] is given by:

$$\vec{a}_{SRP} = \frac{A}{m_{obj}}\frac{E}{C}\frac{AU^2}{|\vec{r}-\vec{r}_1|^2}\cos(\theta_{inc})\left\{2\left(\frac{C_{Rd}}{3}+C_{Rs}\cos(\theta_{inc})\right)\hat{N}+(1-C_{Rs})\hat{S}\right\} \tag{2.7}$$

Where $m_{obj}$ is the mass of the debris, $C_{Rd}$ ,$C_{Rs}$ and $C_{Ra}$ are the coefficients of diffuse, specular and absorbed reflectivity respectively and $A$ is the maximum area of flat plate. The relationship between $C_{Rs}$, $C_{Ra}$ and $C_{Rd}$ is 1 = $C_{Ra}+C_{Rs}+C_{Rd}$, $c$ is velocity of light (299,792,458 m/s), $AU$ is the astronomical unit (149,597,870 km).

For SRP of a spherical body with uniform reflection properties, attitude motion does not have any effect on the orbital evolution. The cannonball model is commonly used as the default solar radiation pressure model in orbit analysis programs in GEODYN-II [40]. The debris is assumed to be a uniform sphere and the direct radiation acceleration is given by:

$$\vec{a}_{cannon} = -\frac{A_{sphere}}{m_{obj}}\frac{E}{C}\frac{AU^2}{|\vec{r}-\vec{r}_1|^2}\cdot\left(1+\frac{4}{9}C_{Rd}\right)\hat{S} \tag{2.8}$$

Where $A_{sphere}$ is cross-sectional area of the sphere.

Finally, the equation of motion of a debris is given by:

$$\ddot{\vec{r}} = -\mu\left(\frac{\vec{r}}{\vec{r}^3}\right) - G\sum_{k=1}^{2} M_k \left(\frac{\vec{r}+\vec{r}_k}{\left|\vec{r}+\vec{r}_k\right|^3} + \frac{\vec{r}_k}{r_k^3}\right) + \vec{a}_{SRP} \tag{2.9}$$

The SRP acceleration ($\vec{a}_{SRP}$) in Eq.(2.9) depends on the model, which Eq.(2.7) and (2.8) are for flat rigid plate and cannonball models respectively

## 2.2 Attitude Dynamics

Euler's rotation equations are the most common method to describe the rotation of a rigid body using a rotating frame of reference with its axis fixed to the body and parallel to the principal axis of inertia.

### 2.2.1 Angular momentum

The net total torque on a rigid body is related to the time derivative of the angular momentum is given as:

$$\dot{\vec{H}} = I\dot{\vec{\omega}} = \vec{\tau}_t - \vec{\omega}\times(I\vec{\omega}) \tag{2.10}$$

Where $\dot{\vec{H}}$ is the time derivative of the angular momentum vector of a rigid body, $\vec{\tau}_t$ is the total sum of all external torques acting on the body, $I$ is the moment of inertia of the rigid body, $\vec{\omega}$ is the angular velocity and $\dot{\vec{\omega}}$ is the angular acceleration.

Throughout this thesis, the total external torques considered for the attitude of HAMR debris are those due to solar radiation pressure and gravity gradient torques. Thus, the total torque can be defined as:

$$\vec{\tau}_t = \vec{\tau}_{SRP} + \vec{\tau}_{Grav} \tag{2.11}$$

Where $\vec{\tau}_t$ is the total external torque from solar radiation torque ($\vec{\tau}_{SRP}$) and gravitational torque ($\vec{\tau}_{Grav}$).

The solar radiation torque ( $\vec{\tau}_{SRP}$ ) is given by:

$$\vec{\tau}_{SRP} = \vec{\rho}_{SRP} \times ([T] \cdot \vec{F}_{SRP}) \tag{2.12}$$

Where $\vec{\rho}_{SRP}$ is the vector from the geometric centre of the objects to the centre of pressure, $\vec{F}_{SRP}$ is solar radiation pressure and $[T]$ is the transformation matrix from the inertial frame to the body frame describing in section 2.3.

The gravitational torque [41] for a rigid body is derived by determining the gravitational force as:

$$\vec{\tau}_{Grav} = \frac{3GM_{\oplus}}{R^3}\left[\vec{R} \times I\vec{R}\right] \tag{2.13}$$

Where $\vec{R} = [T] \cdot \vec{r}$ is the unit vector of the object in the inertial system transforming to the unit vector in a body frame.

## 2.3 Rotational Kinematics

### 2.3.1 Direction cosine matrix

The attitude of a rigid body is most conveniently expressed through a set of axis fixed to the body frame. The transformation of the inertial coordinate frame ( $\vec{N}$ ) to the body coordinate frame ( $\vec{B}$ ) is given as:

$$\begin{bmatrix} B_x \\ B_y \\ B_z \end{bmatrix} = \begin{bmatrix} T_{11} & T_{12} & T_{13} \\ T_{21} & T_{22} & T_{23} \\ T_{31} & T_{32} & T_{33} \end{bmatrix} \begin{bmatrix} N_x \\ N_y \\ N_z \end{bmatrix} \tag{2.14}$$

The rotation matrix ( $[T]$ ) consists of three angular rotations of yaw ( $\psi$ ), pitch ( $\theta$ ) and roll ( $\phi$ ), in a 3-1-3 sequence. The rotation matrix can be written as the product of the three successive rotation matrices:

$$[T]=\begin{bmatrix}\cos\psi & \sin\psi & 0\\ -\sin\psi & \cos\psi & 0\\ 0 & 0 & 1\end{bmatrix}\begin{bmatrix}1 & 0 & 0\\ 0 & \cos\theta & \sin\theta\\ 0 & -\sin\theta & \cos\theta\end{bmatrix}\begin{bmatrix}\cos\phi & \sin\phi & 0\\ -\sin\phi & \cos\phi & 0\\ 0 & 0 & 1\end{bmatrix} \tag{2.15}$$

Which can be expressed as:

$$\begin{aligned}[T] &= R_3(\phi)R_1(\theta)R_3(\psi)\\ &= \begin{bmatrix} c(\phi)\mathrm{c}(\psi)-s(\phi)\mathrm{c}(\theta)s(\psi) & c(\phi)s(\psi)+s(\phi)\mathrm{c}(\theta)c(\psi) & s(\phi)s(\theta)\\ -s(\phi)\mathrm{c}(\psi)-c(\phi)\mathrm{c}(\theta)s(\psi) & -s(\phi)s(\psi)+\mathrm{c}(\phi)\mathrm{c}(\theta)c(\psi) & c(\phi)s(\theta)\\ \mathrm{s}(\theta)s(\psi) & -\mathrm{s}(\theta)c(\psi) & c(\theta)\end{bmatrix}\end{aligned} \tag{2.16}$$

Where cos is abbreviated by “ $c$ ” and sin by “ $s$ ” and

$$\begin{aligned}\phi &= \tan^{-1}\left(\frac{T_{13}}{T_{23}}\right)\\ \theta &= \cos^{-1}(T_{33})\\ \psi &= \tan^{-1}\left(\frac{-T_{31}}{T_{32}}\right)\end{aligned} \tag{2.17}$$

There is however one drawback to using the Euler angle rotations in that there may be a singularity. To avoid this we can makes use of a different attitude parametrisation method by means of quaternions.

### 2.3.2 Quaternions

The properties of quaternions is that the summation of squares of each quaternion unit must always equal 1. It can assist to validate the calculated quaternions.

$$q_1^2+q_2^2+q_3^2+q_4^2=1 \tag{2.18}$$

The elements of the quaternions are presented in terms of the principal eigenvector, $\vec{e}$ , and the singular rotation angle, $\alpha$ , is written as:

$$q_1 = e_1\sin\left(\frac{\alpha}{2}\right) \tag{2.19}$$

$$q_2 = e_2\sin\left(\frac{\alpha}{2}\right) \tag{2.20}$$

$$q_3 = e_3 \sin(\frac{\alpha}{2}) \tag{2.21}$$

$$q_4 = \cos(\frac{\alpha}{2}) \tag{2.22}$$

And then, it can be written in matrix form:

$$\vec{q} = \begin{bmatrix} q_1 \\ q_2 \\ q_3 \\ q_4 \end{bmatrix} \tag{2.23}$$

Euler's eigenaxis rotation theorem [42] states that it is possible to rotate a fixed frame onto any arbitrary frame with a simple rotation of an angle $\alpha$, around an axis $\vec{e}$ that is fixed in both frames called the Euler axis of rotation. With this representation, the transformation matrix can be written as:

$$[R] = \cos(\alpha)[\mathrm{I}] + \left[[\mathrm{I}] - \cos(\alpha)\right][e_1 \quad e_2 \quad e_3][e_1 \quad e_2 \quad e_3]^T - \sin(\alpha)[E] \tag{2.24}$$

Where $[\mathrm{I}]$ is identity matrix and

$$[E] = \begin{bmatrix} 0 & -e_3 & e_2 \\ e_3 & 0 & -e_1 \\ -e_2 & e_1 & 0 \end{bmatrix} \tag{2.25}$$

Substituting Eq.(2.25) into Eq. (2.24), yields:

$$[R] = \begin{bmatrix} c(\alpha) + e_1^2 - e_1^2 c(\alpha) & e_1e_2 - e_1e_2c(\alpha) + e_3s(\alpha) & e_1e_3 - e_1e_3c(\alpha) - e_2s(\alpha) \\ e_1e_2 - e_1e_2c(\alpha) - e_3s(\alpha) & c(\alpha) + e_2^2 - e_2^2c(\alpha)) & e_2e_3 - e_2e_3c(\alpha) + e_1s(\alpha) \\ e_1e_3 - e_1e_3c(\alpha) + e_2s(\alpha) & e_2e_3 - e_2e_3c(\alpha) - e_1s(\alpha) & c(\alpha) + e_3^2 - e_3^2c(\alpha)) \end{bmatrix} \tag{2.26}$$

Where cos is abbreviated by "$c$" and sin by "$s$" and

The unit vectors of the eigenvector can be expressed in terms of the angular rotation and elements of the transformation matrix in Eq. (2.16):

$$e_1 = \frac{(T_{23} - T_{32})}{2\sin(\alpha)} \tag{2.27}$$

$$e_2 = \frac{(T_{31} - T_{13})}{2\sin(\alpha)} \tag{2.28}$$

$$e_3 = \frac{(T_{12} - T_{21})}{2\sin(\alpha)} \tag{2.29}$$

The direction cosine matrix in Eq. (2.16) can be expressed in term of quaternions:

$$\begin{bmatrix} T_{11} & T_{12} & T_{13} \\ T_{21} & T_{22} & T_{23} \\ T_{31} & T_{32} & T_{33} \end{bmatrix} = \begin{bmatrix} 1-2(q_2^2+q_3^2) & 2(q_1q_2+q_3q_4) & 2(q_1q_3-q_2q_4) \\ 2(q_1q_2-q_3q_4) & 1-2(q_1^2+q_3^2) & 2(q_2q_3+q_1q_4) \\ 2(q_1q_3+q_2q_4) & 2(q_2q_3-q_1q_4) & 1-2(q_1^2+q_2^2) \end{bmatrix} \tag{2.30}$$

Then

$$\begin{bmatrix} B_x \\ B_y \\ B_z \end{bmatrix} = \begin{bmatrix} 1-2(q_2^2+q_3^2) & 2(q_1q_2+q_3q_4) & 2(q_1q_3-q_2q_4) \\ 2(q_1q_2-q_3q_4) & 1-2(q_1^2+q_3^2) & 2(q_2q_3+q_1q_4) \\ 2(q_1q_3+q_2q_4) & 2(q_2q_3-q_1q_4) & 1-2(q_1^2+q_2^2) \end{bmatrix} \begin{bmatrix} N_x \\ N_y \\ N_z \end{bmatrix} \tag{2.31}$$

The quaternion matrix can be converted back into a direction cosine matrix from:

$$q_1 = \frac{\left(T_{23} - T_{32}\right)}{4q_4} \tag{2.32}$$

$$q_2 = \frac{\left(T_{31} - T_{13}\right)}{4q_4} \tag{2.33}$$

$$q_3 = \frac{\left(T_{12} - T_{21}\right)}{4q_4} \tag{2.34}$$

$$q_4 = \sqrt{\frac{T_{11} + T_{22} + T_{33} + 1}{2}} \tag{2.35}$$

We can also express the rate of change of the quaternions as:

$$\dot{\vec{q}} = \frac{1}{2}\Omega \cdot \vec{q} \tag{2.36}$$

with

$$\Omega = \begin{bmatrix} 0 & \omega_3 & -\omega_2 & \omega_1 \\ -\omega_3 & 0 & \omega_1 & \omega_2 \\ \omega_2 & -\omega_1 & 0 & \omega_3 \\ -\omega_1 & -\omega_2 & -\omega_3 & 0 \end{bmatrix} \tag{2.37}$$

## 2.4 Numerical integration

In this thesis, the numerical integrator used to solve the propagation of this thesis is the Runge-Kutta method in MATLAB®. The command ODE45 performs a direct numerical integration of a set of 1st order differential equations y' = f(t,y), $y(t_o) = y_o$ from start time ($t_o$) to some final time ($t_f$). ODE45 varies the size of the step of the independent variable in order to meet the accuracy you specify at any particular point along the solution. If ODE45 can take "big" steps and still meet this accuracy, it will do so and will therefore move quickly through regions where the solution does not "change" greatly. In regions where the solution changes more rapidly, ODE45 will take "smaller" steps. While this strategy is good from an efficiency or speed point of view, it means that the solution does not appear at a fixed set of values for the variable (as a fixed-step method would) and sometimes the solution curves look a little ragged. In my thesis, I had changed only RelTol: 1e6 (default = 1e3) in order to improve the speed of simulation. Then, the propagation of the 2nd order differential equations of orbital and attitude equations is converted to an equivalent system of the 1st order equations. The new system of orbital dynamics is then written as:

$$\begin{aligned} \dot{\vec{r}} &= \vec{v} \\ \dot{\vec{v}} &= \vec{a}_{\oplus} + \vec{a}_{\odot} + \vec{a}_{☾} + \vec{a}_{SRP} \end{aligned} \tag{2.38}$$

In case of coupled attitude and orbital dynamics, the equations of motion are given by:

$$\begin{aligned} \dot{\vec{r}} &= \vec{v} \\ \dot{\vec{v}} &= \vec{a}_{\oplus} + \vec{a}_{\odot} + \vec{a}_{☾} + \vec{a}_{SRP} \\ \dot{\vec{\omega}} &= \vec{\tau}_t - \vec{\omega} \times (I\vec{\omega}) \\ \dot{\vec{q}} &= \frac{1}{2}\Omega \cdot \vec{q} \end{aligned} \tag{2.39}$$

All simulations in this chapter are performed on a PC with CPU @ 1.80 GHz and 8GB RAM. The validation results of MATLAB® code developed by the author yield reasonable results as compared to System Tool Kit (STK) software in case of cannonball. The other cases in the thesis were unable to be generated in STK due to the coupling attitude and deformation dynamics.

## 2.5 Simulation analysis

This section investigates the short and long term orbital evolution of different rigid objects modelled either as cannonball or flat rigid plate shown in Figure 2.4. For preliminary investigation, both objects have been assumed as the same as reflection properties [18] $C_{Rs} = 0.6$, $C_{Rd} = 0.26$ and $C_{Ra} = 0.14$ and the same AMR set to 20 $m^2/kg$. The cannonball rigid body is used to represent the standard model. The flat rigid plate consists of one substrate aluminized with an extremely thin layer (25.4 micron) on both sides and an area of one square meter. The motion of this flat rigid plate coupled attitude and orbital motion is propagated twice: the first time with no any torque disturbing on this simulation called “fixed attitude”, the second considering a torque with propagations called “coupled attitude”. The initial values of the orbital elements and initial Euler angles are shown in Table 2.1 and Table 2.2. The attitude motion has been calculated by means of quaternions to avoid singularities but shown in terms of Euler angles to allow for a clearer.

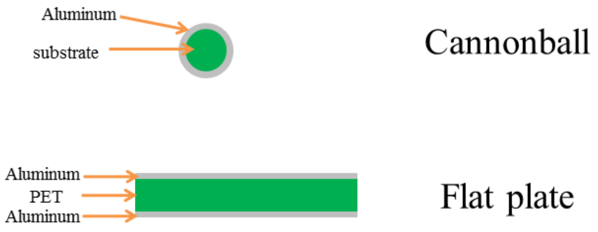

**Figure 2.4 Cross-section of cannonball and thin flat plate.**

**Table 2.1 The initial Kepler elements.**

| Semi-major axis(km) | Eccentricity | Inclination (degree) | Argument of perigee (degree) | Longitude of ascending node (degrees) | Mean anomaly (degree) |
|---|---|---|---|---|---|
| 42,164 | 0.0001 | 1.0 | 1.0 | 30.0 | 5.0 |

**Table 2.2 The initial Euler's angle and angular velocities.**

| Euler's angle | 1st rotation<br>($\psi$) | 2nd rotation<br>($\theta$) | 3rd rotation<br>($\phi$) |
|---|---|---|---|
| Angle(degree) | 15.5 | 32 | 43 |
| Angular velocity(degree/s) | 0 | 0 | 0 |

### 2.5.1 Short term evolution

Figure 2.5 shows the periodic short term evolution of the inclination and eccentricity in GEO environments (Earth's gravity, third body from the sun and the moon and solar radiation pressure) of cannonball, fixed attitude and coupled attitude, in which a secular trend towards high values of the two orbital parameters can clearly be seen. All evolutions of the orbital parameters are typical of HAMR objects. The results show that the eccentricity of cannonball has the highest secular trend but the eccentricity of coupled attitude lies between the cannonball and the fixed attitude. The inclinations of cannonball and fixed attitude show a similar periodic trend with smaller amplitude for the fixed attitude. The coupled attitude presents non-pattern of inclination, which is significantly different from the others because the variations of SRP forces in Figure 2.6, are due to the change of effective cross-sectional area subjecting to the fluctuation of SRP acceleration. It is because the gravity gradient torque induced to significantly change the attitude motion as shown in Figure 2.7. There is however no SRP torque disturbing because the centre of pressure is on the same as the centre of mass (no deformation). For fixed attitude, which is no any torque to disturb, the SRP accelerations slightly decrease because the cross-sectional area depends on the sun vector and initial attitude sets while the SRP acceleration of cannonball is almost constant during the 6 days. This can be explained in that the acceleration of the cannonball model depends solely on the direction of the sun vector.

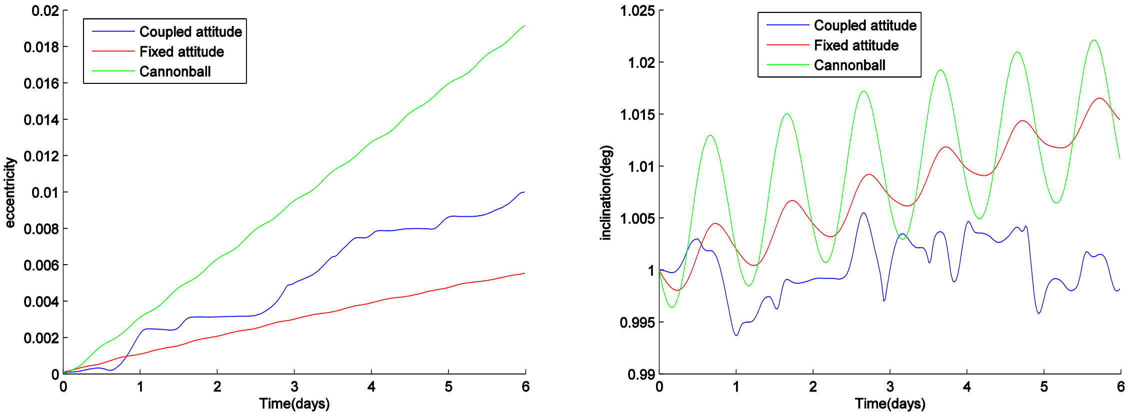

a) b)

**Figure 2.5 Comparison inclination and eccentricity evolution of coupled attitude, fixed attitude and cannonball over 6 days under conservative perturbations (Earth's gravity, third body from the sun and the moon) and non- conservative perturbation (SRP) a) Eccentricity evolution b) Inclination evolution.**

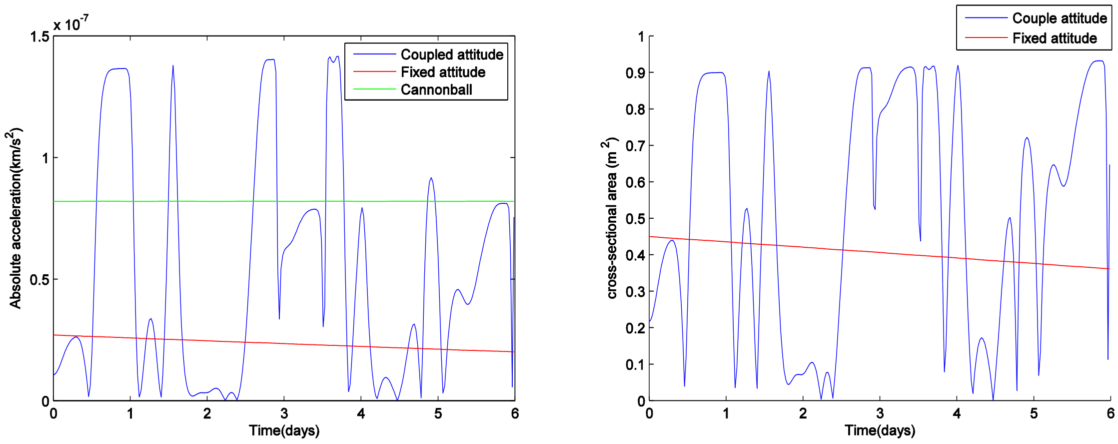

**Figure 2.6 Comparison of the total absolute acceleration and cross-sectional area of cannonball and flat rigid plate over 6 days.**

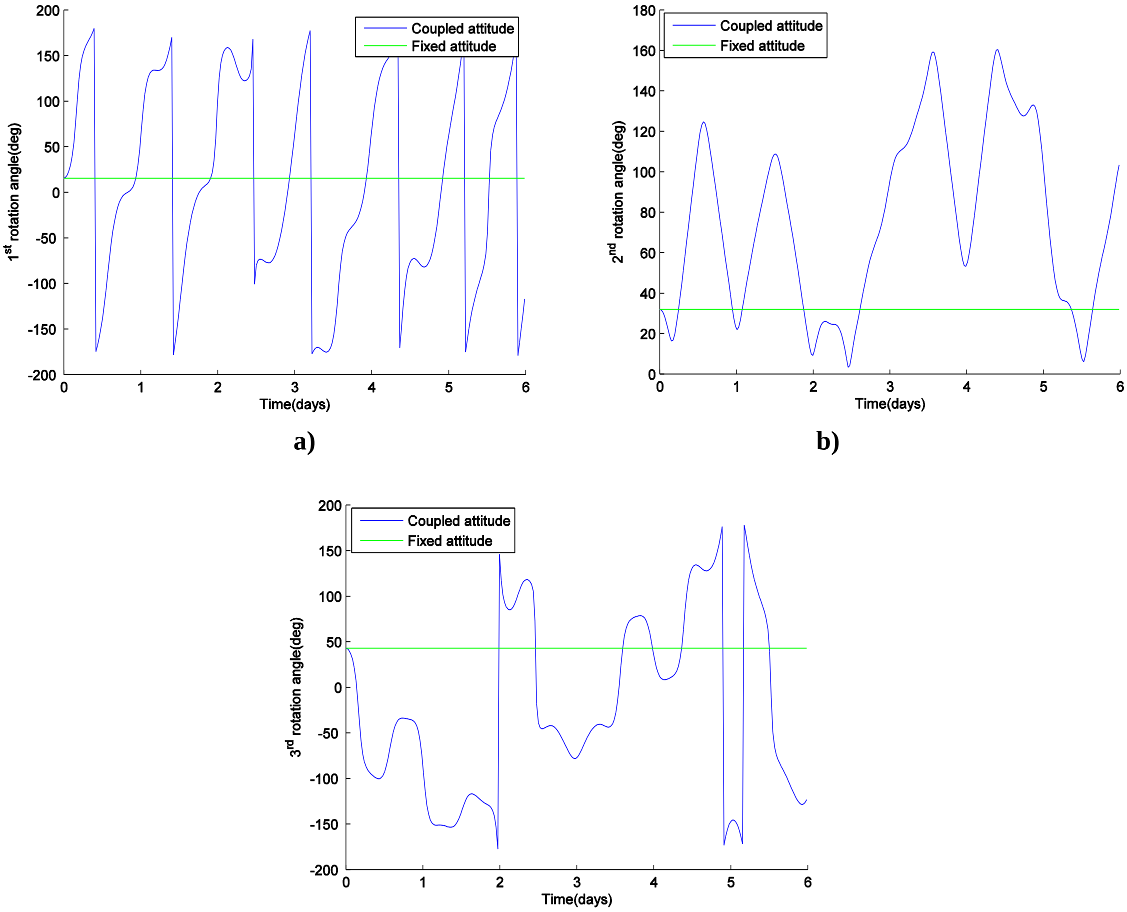

a) b)

c)

**Figure 2.7 Comparisons of Euler angle evolutions of coupled attitude and fixed attitude over 6 days under conservative perturbations Earth's gravity, third body from the sun and the moon and non-conservative perturbations (SRP) a) the 1st Euler rotation ( $\psi$ ) b) the 2nd Euler rotation ( $\theta$ ) c) the 3rd Euler rotation ( $\phi$ ).**

### 2.5.2 Long term evolution

The evolutions of eccentricity and inclination over a period of 100 days for the two rigid bodies are shown in Figure 2.8. The eccentricity trend of the cannonball and coupled attitude increases in different rate that it appears to be linear but coupled attitude tapers off towards the end day while the fixed attitude shows an oscillating behaviour, increasing until the 28th day, then decreasing before growing up rapidly. The inclination evolutions show the significantly different trends for all objects due to the differences of SRP accelerations as shown in Figure 2.9. For coupled attitude, the absolute SRP acceleration trend (blue line) significantly fluctuates, which the range is between $1.65\times10^{-7}$ km/s$^2$ and $1.25\times10^{-11}$ km/s$^2$, and relates to the variations of cross-sectional area but the change of total absolute acceleration of fixed attitude (red line) is going down since starting simulation until the 28.53th day is the lowest SRP acceleration ($1.315\times10^{-11}$ km/s$^2$) because the normal vector is almost perpendicular to the Sun vector (cross-sectional area = 0.0003231 m$^2$) after that the cross-sectional area trend grows up, which coherent with the absolute SRP accelerations. Comparing the both simulations of flat rigid plate with cannonball, the total absolute accelerations (green line) of cannonball do not significantly change over 100-day evolutions. In conclusion, this investigation supports that the HAMR debris is very sensitive to SRP model and a different orientation of the object leads to importantly change the orbital dynamics.

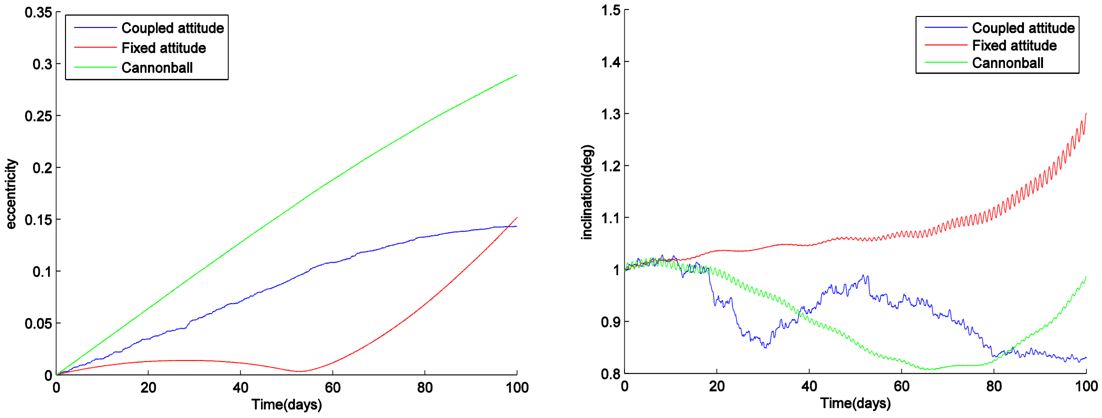

a) b)

**Figure 2.8 Comparison inclination and eccentricity evolutions of coupled attitude, fixed attitude and cannonball over 100 days under conservative perturbations (Earth's gravity, third body from the sun and the moon) and non-conservative perturbation (SRP) a) Eccentricity evolution b) Inclination evolution.**

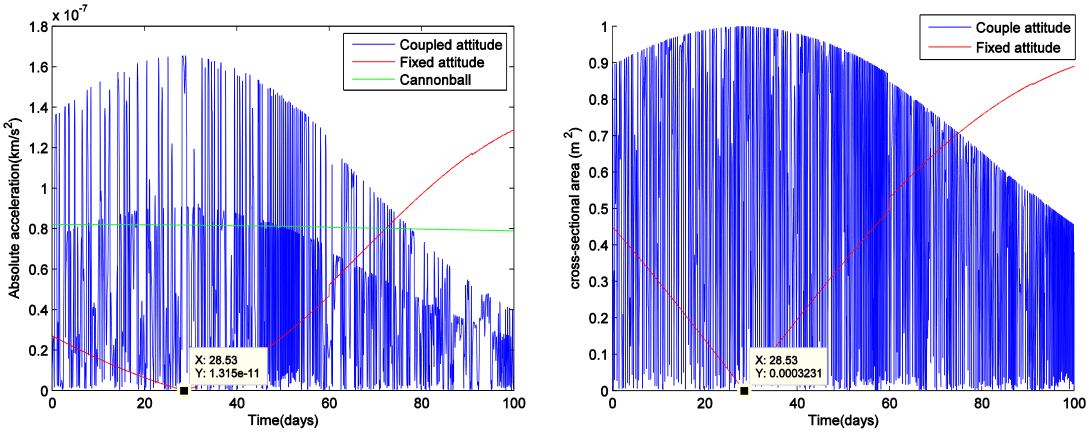

**Figure 2.9 Comparison of the total absolute acceleration and variations of cross-sectional area of coupled attitude, fixed attitude and cannonball over 100 days.**

## 2.6 Summary

This chapter presented the analysis of the short and long term evolution of the orbital elements of two different rigid body models: cannonball and flat rigid plate in near geostationary orbits. The attitude motion of flat rigid plate (fixed attitude, coupled attitude), leading to vary of SRP exposed area, effects to different orbital dynamics in short and long term evolutions although coupled attitude has only a gravity gradient torque disturbing to the attitude. However, assumption of flat object is an oversimplification of the problem. The combination of orbital, light curve and spectral measurements suggest that AMR is not stable (deformation) and fast complex rotation [16, 30]. The deformation of HAMR model that leads to varieties of the AMR value itself over time and induces the faster attitude motion due to SRP torque, highly effecting to change both orbital elements and attitude motions as the investigations of Früh and McMahon, is necessary to combine in the orbital propagation. Therefore, the next chapter will investigate the attitude-orbit motions of the new model based on Bernoulli-Euler theory that can be changed a shape during propagation in order to increase the accuracy of prediction.

# 3

# 3 Flexible model with Bernoulli-Euler theory

This chapter introduces a simplified model to represent the deformation of HAMR debris by means of Bernoulli-Euler theory which underpins Finite Element Analysis (FEA). The Euler eigenaxis rotation theorem loses its validity when a body is deformed leading to changes in its centre of mass and moments of inertia. The attitude representation for the flexible model is therefore presented in this chapter. This model adds a further set of dynamical equations, which accounts for the flexibility of the body, into the attitude and orbital equations; the resulting system is then numerically integrated to evaluate the coupling between orbital and attitude dynamics over 6 and 100 days and the ensuing results are then compared with two rigid models of similar objects (cannonball and a flat rigid body) in GEO.

## 3.1 Bernoulli-Euler theory

Bernoulli-Euler theory [43] is used here to investigate the deformation of the flexible debris. Figure 3.1(a) represents a one beam element with two nodes (two end of beam) and 12 degrees of freedom (three linear and three angular at each node) in the inertial frame $(\hat{I}, \hat{J}, \hat{K})$.

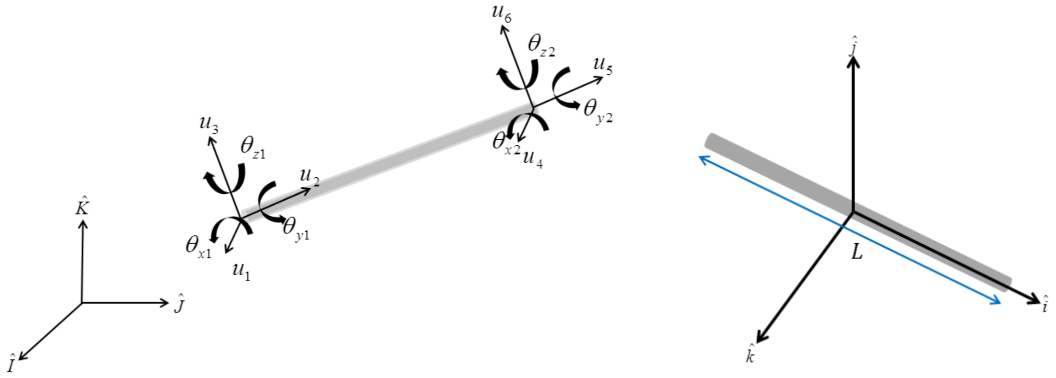

**a)** **b)**

**Figure 3.1 Bernoulli beam element with 2 nodes in a) inertial frame $(\hat{I}, \hat{J}, \hat{K})$ . b) body frame $(\hat{i}, \hat{j}, \hat{k})$**

The nodal displacements for an element consisting of the 1st and 2nd node are given by:

$$\vec{U}^T = \begin{bmatrix} u_1 & u_2 & u_3 & \theta_{x1} & \theta_{y1} & \theta_{z1} & u_4 & u_5 & u_6 & \theta_{x2} & \theta_{y2} & \theta_{z2} \end{bmatrix} \tag{3.1}$$

Where $u_i$ are linear displacements and $\theta$ are angular displacements.

### 3.1.1 Mass and stiffness matrix in body frame

The standard mass matrix of the Bernoulli-Euler beam element in the body frame ($\left[\overline{M}\right]$) is expressed as:

$$\left[\overline{M}\right] = \rho AL \begin{bmatrix}
\frac{1}{3} & 0 & 0 & 0 & 0 & 0 & \frac{1}{6} & 0 & 0 & 0 & 0 & 0 \\
0 & \frac{13}{35} & 0 & 0 & 0 & \frac{11L}{210} & 0 & \frac{9}{70} & 0 & 0 & 0 & -\frac{13L}{420} \\
0 & 0 & \frac{13}{35} & 0 & -\frac{11L}{210} & 0 & 0 & 0 & \frac{9}{70} & 0 & -\frac{13L}{420} & 0 \\
0 & 0 & 0 & \frac{I_y + I_z}{3A} & 0 & 0 & 0 & 0 & 0 & \frac{I_y + I_z}{6A} & 0 & 0 \\
0 & 0 & -\frac{11L}{210} & 0 & \frac{L^2}{105} & 0 & 0 & 0 & \frac{6EI_y}{L^2} & 0 & -\frac{L^2}{140} & 0 \\
0 & \frac{11L}{210} & 0 & 0 & 0 & \frac{L^2}{105} & 0 & -\frac{6EI_z}{L^2} & 0 & 0 & 0 & -\frac{L^2}{140} \\
\frac{1}{6} & 0 & 0 & 0 & 0 & 0 & \frac{1}{3} & 0 & 0 & 0 & 0 & 0 \\
0 & \frac{9}{70} & 0 & 0 & 0 & \frac{13L}{420} & 0 & \frac{13}{35} & 0 & 0 & 0 & -\frac{11L}{210} \\
0 & 0 & \frac{9}{70} & 0 & \frac{-13L}{420} & 0 & 0 & 0 & \frac{13}{35} & 0 & \frac{11L}{210} & 0 \\
0 & 0 & 0 & \frac{I_y + I_z}{6A} & 0 & 0 & 0 & 0 & 0 & \frac{I_y + I_z}{3A} & 0 & 0 \\
0 & 0 & \frac{13L}{420} & 0 & \frac{-L^2}{140} & 0 & 0 & 0 & \frac{11L}{210} & 0 & \frac{L^2}{105} & 0 \\
0 & \frac{-13L}{420} & 0 & 0 & 0 & \frac{-L^2}{140} & 0 & -\frac{11L}{210} & 0 & 0 & 0 & \frac{L^2}{105}
\end{bmatrix} \tag{3.2}$$

Where $E$ is Young's modulus of the material, $L$ is length of the element, $\rho$ is density of the material, $A$ is the cross-sectional area of the beam, $I_y$ and $I_z$ are the mass moments of inertia with respect to the y axis and z axis respectively.

In this investigation, we assume the deformation of beam in terms of small deformations and the material stiffness does not change during loading. Assuming a large displacement would imply a change to the stiffness of the body which would need to be updated at every time step leading to high computational requirements. The standard stiffness matrix for a Bernoulli-Euler beam element in the body frame $\left[\bar{K}\right]$ is given by:

$$\left[\bar{K}\right]=\begin{bmatrix} \frac{EA}{L} & 0 & 0 & 0 & 0 & 0 & -\frac{EA}{L} & 0 & 0 & 0 & 0 & 0 \\ 0 & \frac{12EI_z}{L^3} & 0 & 0 & 0 & -\frac{6EI_z}{L^2} & 0 & \frac{12EI_z}{L^3} & 0 & 0 & 0 & \frac{6EI_z}{L^2} \\ 0 & 0 & \frac{12EI_y}{L^3} & 0 & \frac{6EI_y}{L^2} & 0 & 0 & 0 & -\frac{12EI_y}{L^3} & 0 & -\frac{6EI_y}{L^2} & 0 \\ 0 & 0 & 0 & \frac{GJ}{L} & 0 & 0 & 0 & 0 & 0 & -\frac{GJ}{L} & 0 & 0 \\ 0 & 0 & -\frac{6EI_y}{L^2} & 0 & \frac{4EI_y}{L} & 0 & 0 & 0 & \frac{6EI_y}{L^2} & 0 & \frac{2EI_z}{L} & 0 \\ 0 & \frac{6EI_z}{L^2} & 0 & 0 & 0 & \frac{4EI_z}{L} & 0 & -\frac{6EI_z}{L^2} & 0 & 0 & 0 & \frac{2EI_z}{L^2} \\ -\frac{EA}{L} & 0 & 0 & 0 & 0 & 0 & \frac{EA}{L} & 0 & 0 & 0 & 0 & 0 \\ 0 & -\frac{12EI_z}{L^3} & 0 & 0 & 0 & -\frac{6EI_z}{L^2} & 0 & \frac{12EI_z}{L^3} & 0 & 0 & 0 & -\frac{6EI_z}{L^2} \\ 0 & 0 & -\frac{12EI_y}{L^3} & 0 & \frac{6EI_y}{L^2} & 0 & 0 & 0 & \frac{12EI_y}{L^3} & 0 & \frac{6EI_y}{L^2} & 0 \\ 0 & 0 & 0 & -\frac{GJ}{L} & 0 & 0 & 0 & 0 & 0 & \frac{GJ}{L} & 0 & 0 \\ 0 & 0 & -\frac{6EI_y}{L^2} & 0 & \frac{2EI_y}{L^2} & 0 & 0 & 0 & \frac{6EI_y}{L^2} & 0 & \frac{4EI_y}{L^2} & 0 \\ 0 & \frac{6EI_z}{L^2} & 0 & 0 & 0 & \frac{2EI_z}{L^2} & 0 & -\frac{6EI_z}{L^2} & 0 & 0 & 0 & \frac{6EI_z}{L} \end{bmatrix} \qquad (3.3)$$

Where $G$ is the shear modulus and $J$ is the polar moment of inertia of the cross section area of beam.

### 3.1.2 Coordinate transformation

The body frame can be transformed onto an inertial frame of reference (Figure 3.2) by using the following transformation matrix:

$$T_e = \begin{bmatrix} \lambda_{3x3} & 0 & 0 & 0 \\ 0 & \lambda_{3x3} & 0 & 0 \\ 0 & 0 & \lambda_{3x3} & 0 \\ 0 & 0 & 0 & \lambda_{3x3} \end{bmatrix} \qquad (3.4)$$

Where $\lambda = \begin{bmatrix} C_{Xx} & C_{Yx} & C_{Zx} \\ C_{Xy} & C_{Yy} & C_{Zy} \\ C_{Xz} & C_{Yz} & C_{Zz} \end{bmatrix}$ and $C_{Xx} = \cos\theta_{Xx}$

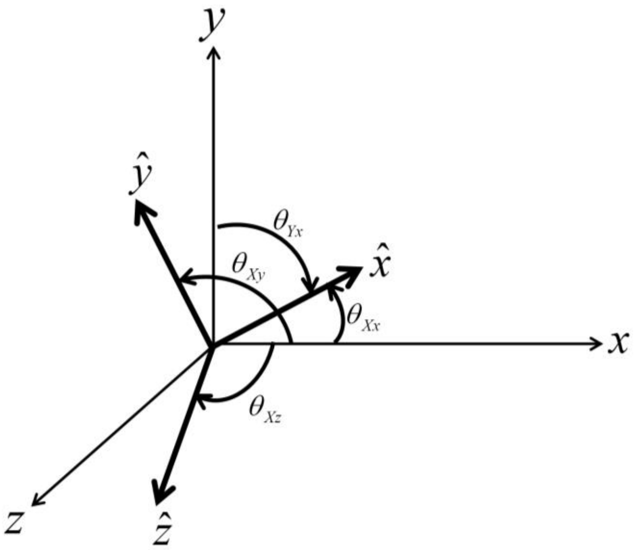

**Figure 3.2 Direction cosines associated with the x axis**

Where $\theta_{Xx}$, $\theta_{Yx}$ and $\theta_{Zx}$ are measured from inertial axes $\hat{I}$, $\hat{J}$ and $\hat{K}$ with respect to the local axis x respectively.

Thus, the stiffness matrix and mass matrix in inertial coordinates are obtained as:

$$[K]=T_e^T\left[\bar{K}\right]T_e \text{ and } [M]=T_e^T\left[\bar{M}\right]T_e \tag{3.5}$$

Finally, the most common and convenient approach is to define the damping matrix ($[C]$) is through Rayleigh damping [44], which assumes a proportionality to the mass matrix ($[M]$) and stiffness matrix ($[K]$) given by:

$$[C]=\alpha[M]+\beta[K] \tag{3.6}$$

Where $\alpha$ and $\beta$ are coefficients related to the mass and stiffness of the system. In the formulation of Rayleigh damping, the mass p damping effect is dominant at the lower frequencies while the stiffness damping is dominant at the higher frequencies. $\alpha$ and $\beta$ are therefore the attributes of the lower and higher resonant frequencies, respectively. In this investigation, $\alpha$ and $\beta$ are defined as 0.0334 s$^{-1}$ and 0.0475 s. (See more information in Appendix C).

### 3.1.3 Dynamical equation

The analysis of the dynamical equations of the beam element requires the description of 12 degrees of freedom, expressed as:

$$[M]\ddot{\vec{U}}+[C]\dot{\vec{U}}+[K]\vec{U}=\vec{F} \tag{3.7}$$

where $\left[M\right]$is mass matrix of the beam element in the inertial frame, $\left[C\right]$ is damping matrix of the beam element in the inertial frame, $\left[K\right]$ is stiffness matrix of the beam element in the inertial frame. $\vec{U}$, $\dot{\vec{U}}$ and $\ddot{\vec{U}}$ are the vectors of position, velocity and acceleration in the inertial frame respectively as:

$$\begin{aligned}\dot{U}^T &= \begin{bmatrix}\dot{u}_1 & \dot{u}_2 & \dot{u}_3 & \dot{\theta}_{x1} & \dot{\theta}_{y1} & \dot{\theta}_{z1} & \dot{u}_4 & \dot{u}_5 & \dot{u}_6 & \dot{\theta}_{x2} & \dot{\theta}_{y2} & \dot{\theta}_{z2}\end{bmatrix}\\ \ddot{U}^T &= \begin{bmatrix}\ddot{u}_1 & \ddot{u}_2 & \ddot{u}_3 & \ddot{\theta}_{x1} & \ddot{\theta}_{y1} & \ddot{\theta}_{z1} & \ddot{u}_4 & \ddot{u}_5 & \ddot{u}_6 & \ddot{\theta}_{x2} & \ddot{\theta}_{y2} & \ddot{\theta}_{z2}\end{bmatrix}\end{aligned} \tag{3.8}$$

The external force ( $\vec{F}$ ) is the external column force vector, which consists of translational force $(F_x, F_y, F_z)$ and torsion moment $(M_x, M_y, M_z)$ along the x, y and z axis: Also, the external forces are applied at the nodes of beam elements. If external forces are applied between nodes, they are replaced by work-equivalent nodal forces.

$$\vec{F}^T = \begin{bmatrix}F_{x1} & F_{y1} & F_{z1} & M_{x1} & M_{y1} & M_{z1} & F_{x2} & F_{y2} & F_{z2} & M_{x2} & M_{y2} & M_{z2}\end{bmatrix} \tag{3.9}$$

## 3.2 Deformation Analysis

In this section, we analyse the deformation of a flat thin plate modelled by means of beam elements as shown in Figure 3.3. PET® is selected as substrate material of a membrane. Reflection and material properties of PET®, shown in Table 3.1, are based on the red book [18]. The basic structure of MLI is composed of a single sheet of PET®, with thickness of 6 μm and an aluminium coating of 1000 Å thick on both sides. This investigation assumes the model to be a single layer of PET®.

**Table 3.1 Properties of PET® material**[18].

| Type material | Mass Density [kg/m$^3$] | Young's Modulus [N/m$^2$] | Poisson's ratio ($\nu$) | *Cs, Cd, Ca* |
|---|---|---|---|---|
| PET | 1,390 | 8.81x10$^9$ | 0.38 | 0.6 0.26 0.14 |

In the initial test, we model a thin flat plate ($1\times1$ m$^2$) with 12 beam elements as shown in Figure 3.4. There are 9 nodes and 54 DOFs. Then, we test the model by applying a force at the geometric centre of the model as shown in Figure 3.4. The results show that the shape is deformed in the direction of the force and the tension force causes the nodes to move.

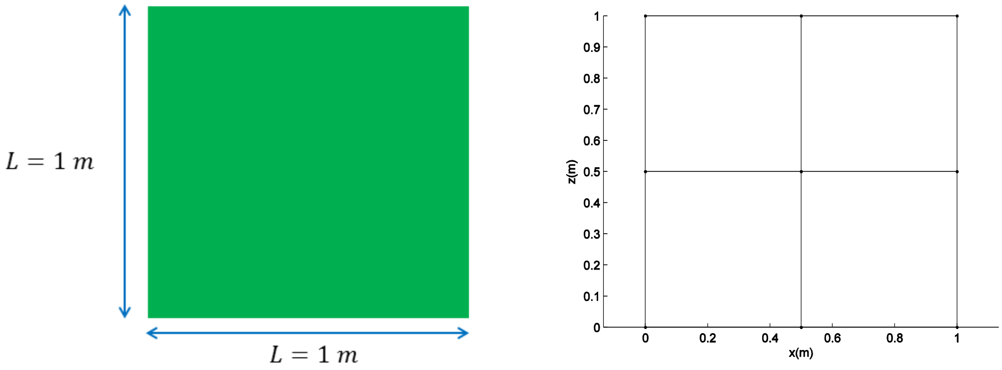

**a)** **b)**

**Figure 3.3 Comparison thin flat plate with flexible model based on FEA a) thin flat pate b) flexible model (12 beam elements, 9 nodes, 54 DOFs)**

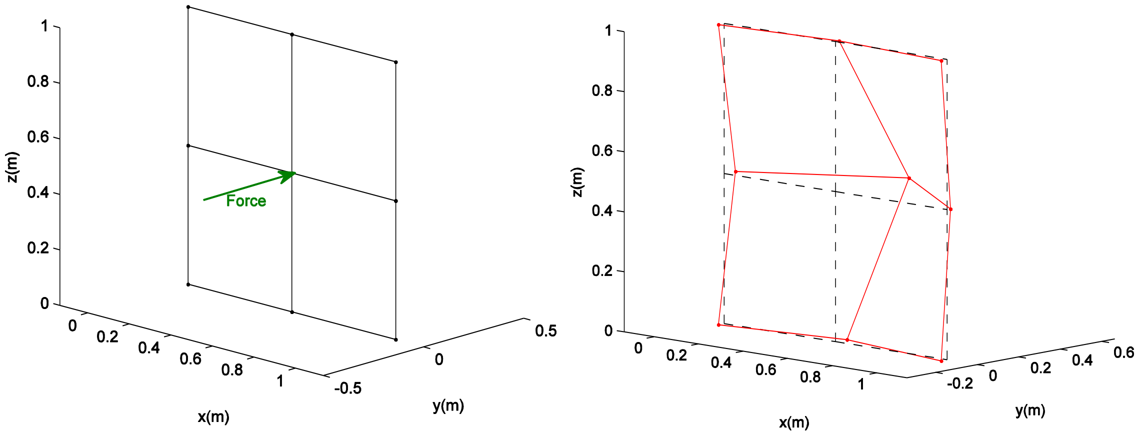

a) b)

**Figure 3.4 The simulated results of the thin flat plate by applying the sudden force -7.000E-5 N in the centre of a membrane for one second a) Initial shape b) the simulated results.**

### 3.2.1 Simplification of flexible model

In order to reduce the computational cost when coupling flexible modes with attitude and orbital motions, a simple model is initially analysed. This consists of 3 nodes, connected with 2 beam elements representing the plate of a membrane as shown in Figure 3.5. The mass of the flat sheet is distributed on both beam elements. The model will have 18 degrees of freedom. The length of each beam element ($L_1 = L_2$) is 0.5 m. This model is called “Bernoulli model”.

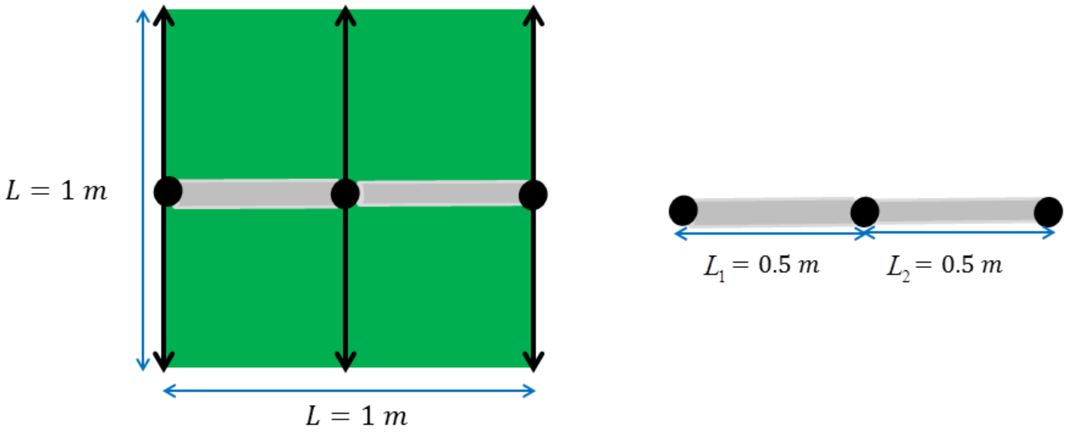

a) b)

**Figure 3.5 Simplification flexible model a) beam element represents a plate of a membrane b) side view.**

### 3.2.2 Deformation of Bernoulli model

In order to test the deformation of the Bernoulli model, we perform two numerical simulations; the first with the same stiffness of PET and the second with a stiffness 100 times higher than that of PET.

We assume two different initial shapes, triangular and flat as shown in Figure 3.6. These configurations are then subjected to a force of magnitude 8.011E-5 N on the 1st node acting first along the x axis and then along the y axis (x and y directions respectively). In Figure 3.7(a), the 1st node displacement moves to the right side while the 3rd node move downwards. The 1st node of the flat plate in Figure 3.8(a) moves down and results pulls with it the 2nd and 3nd nodes due to tension forces. These results are used to validate the simple model of the natural displacements of low weight and thin material. Due to the deformation in Figure 3.7(b) and Figure 3.8(b), it effects to shift the centre of mass from its initial position. As a result, it affects the method to define the attitude motion of the Bernoulli model is as shown in a section 3.2.5.

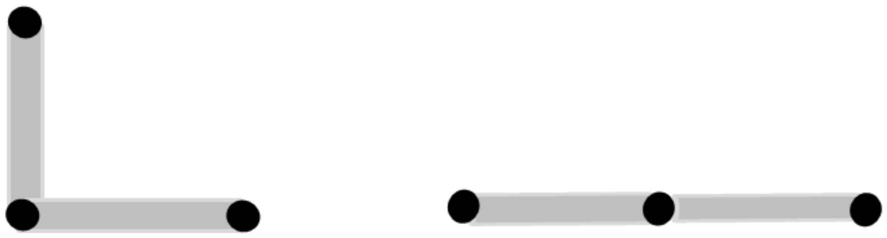

a) b)

**Figure 3.6 Initial shape of Bernoulli body a) triangular shape b) flat plate.**

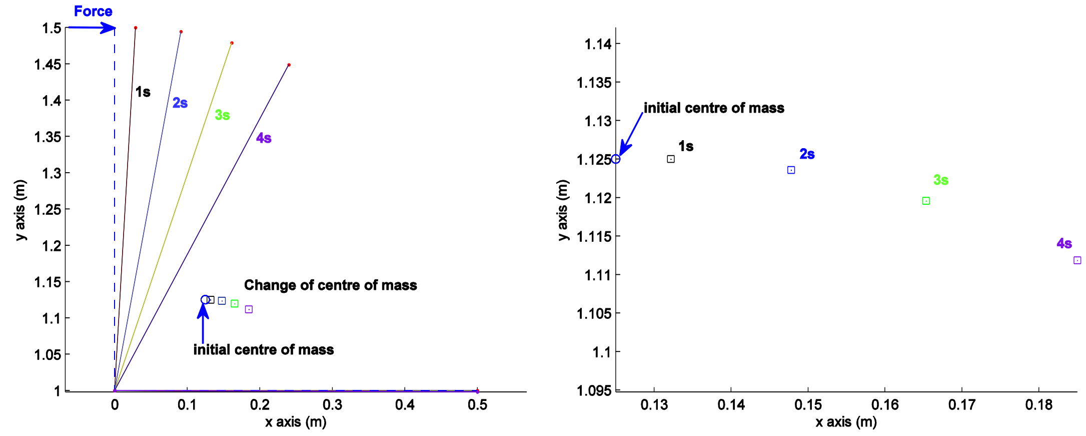

a) b)

**Figure 3.7 Numerical results of triangular shape and change of centre of mass over 4 seconds by a force 8.011E-5 N (blue arrow) in the first node in x direction axis a) simulated results b) change of centre of mass.**

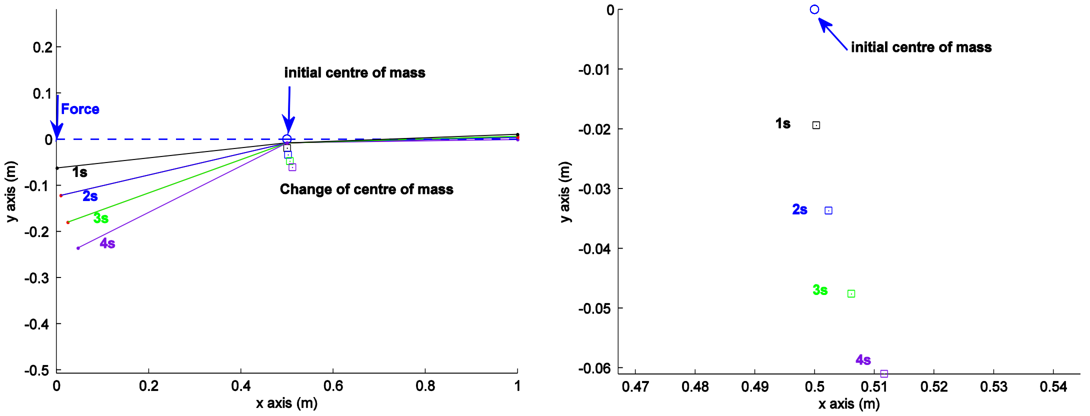

**a) b)**

**Figure 3.8 Numerical results of flat plate and change of centre of mass over 4 seconds by force 8.011E-5 N (blue arrow) in the first node in negative y direction axis a) simulated results b) change of centre of mass.**

The second numerical analysis is performed by increasing Young's modulus to 8.81E11 (100 times of PET® as equal as a metal [45]) and the initial shape is set to be a flat shape. Figure 3.9 shows that when applying a force of same magnitude as before along the negative y direction the body rotates around the centre of mass and there appears to be no deformation. In fact, the centre of mass moves only by a few millimetres as shown in Figure 3.9(b). It can be seen that by increasing the stiffness of the model leads to the behaviour as a rigid plate.

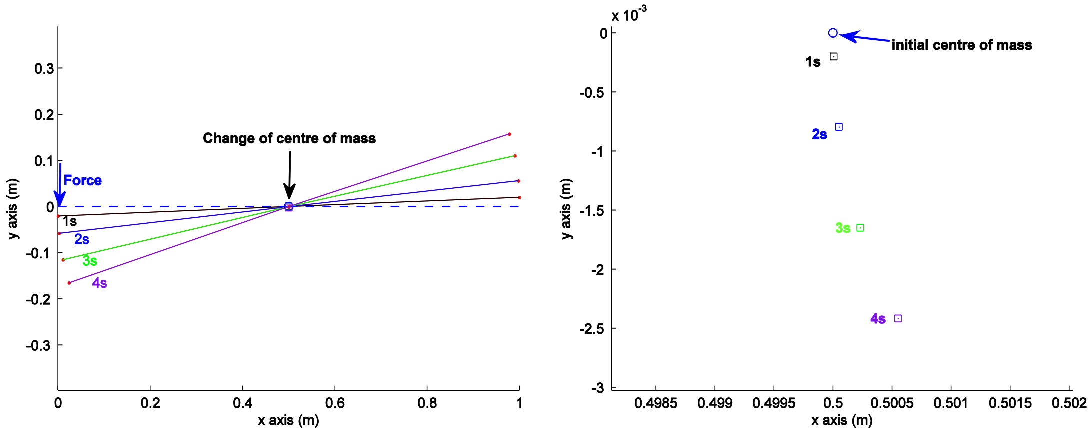

a) b)

**Figure 3.9Numerical results with $E$ = 8.81E11 N/m$^2$ of flat plate and change of centre of mass over 4 seconds are forced (8.011E-5 N) (blue arrow) in the first node in y direction axis a) simulated results b) change of centre of mass**.

### 3.2.3 Solar radiation pressure for Bernoulli model

Solar radiation pressure will act upon both beam elements and defined as:

$$\vec{F}_{SRP,j} = A_j \frac{E}{C} \frac{A_\oplus^2}{\left|\vec{x}_j - \vec{x}_1\right|^2} \hat{S}_j \hat{N}_j \left[ (1 - C_{Rs,j}) \hat{S}_j + 2 (C_{Rs,j} \cdot \hat{S}_j \hat{N}_j + \frac{1}{3} C_{Rd,j}) \hat{N}_j \right] \qquad (3.10)$$

According to Bernoulli-Euler theory, this SRP force acting on the centre of a beam element will pass through on the two nodes connected with that beam element in the same direction. The SRP acceleration of $j^{th}$ and $j+1^{th}$ nodes (Figure 3.10) can be defined as:

$$\vec{a}_{SRP,j,j+1} = \frac{\vec{F}_{SRP,j} / 2}{m_j} \qquad (3.11)$$

where $\vec{x}_j$ and $\vec{x}_1$ are the position vector of the geometric centre of $j^{th}$ beam element and the Sun vector in ECI frame respectively, $E$ is the solar constant (1,353 W/m$^2$), $C$ is speed of light (299,792,458 m/s), $A_j$ is the area of the $j^{th}$ beam element, $m_j$ is the mass of the $j^{th}$ beam element, $C_{Rs,j}$, $C_{Rd,j}$ and $C_{Ra,j}$ are the coefficients of specular, diffuse and absorbed reflectivity for the $j^{th}$ beam element respectively. The surface normal unit vector, $\hat{N}_j$, and the solar incidence unit vector, $\hat{S}_j$, are required to specify the orientation of the Bernoulli body on the centre of pressure of the $j^{th}$ beam element.

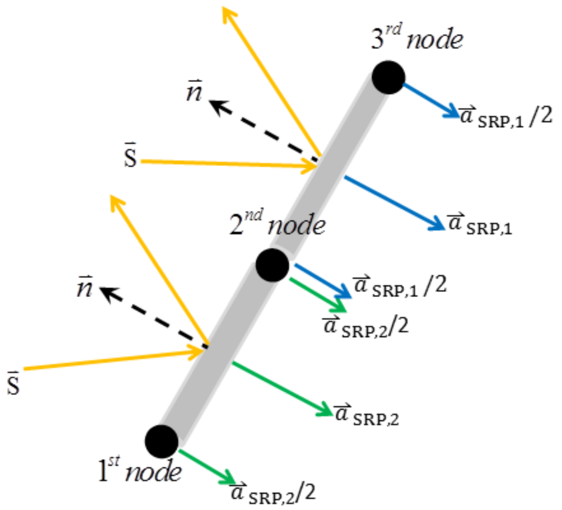

**Figure 3.10 Solar radiation pressure on each node in side view.**

### 3.2.4 Gravitational forces for Bernoulli model

The gravitation forces (Earth's gravity and third body perturbations from the Sun and the Moon as introduced in Chapter 2) will act on each node as shown in Figure 3.11 in the case of the Earth's gravity forces ( $\vec{F}_{\oplus}$ ).

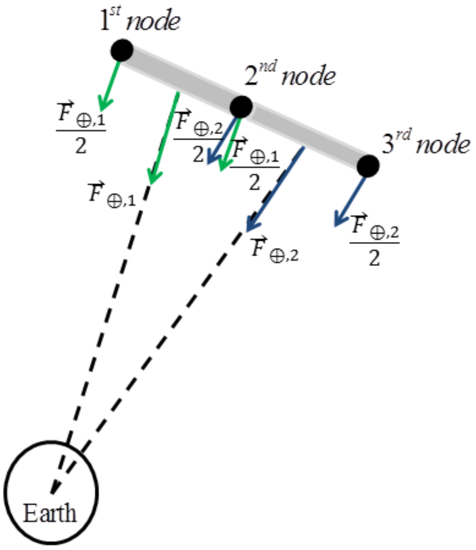

**Figure 3.11 The Earth gravity forces on each node in side view.**

### 3.2.5 Attitude dynamics of the Bernoulli model

As shown in Chapter 2, Euler angles can be used to describe the attitude of a rigid body. The attitude is referenced to the centre of mass but in the case of a Bernoulli model, the centre of mass and moments of inertia will change when the body is deformed from its initial configuration. Therefore, Euler angles cannot be used and we must determine the origin of the body reference frame on the second node as shown in Figure 3.12.

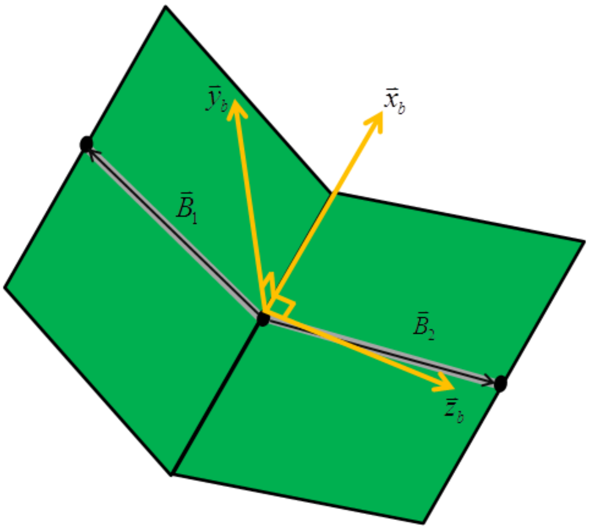

**Figure 3.12 Attitude motion of Bernoulli model in body frame ( $\vec{x}_b$ , $\vec{y}_b$ , $\vec{z}_b$ ).**

The $\vec{B}_1$ and $\vec{B}_2$ are vectors from the 2nd node to 1st node and 3rd node in body frame respectively. The $\vec{x}_b$ is the cross product between $\vec{B}_1$ and $\vec{B}_2$. The y-axis ($\vec{y}_b$) is perpendicular to the x axis and the z-axis ($\vec{z}_b$) is cross product between $\vec{x}_b$ and $\vec{y}_b$ We define the transformation matrix following a 3-1-3 sequence, ($\psi, \theta, \phi$) and then use quaternions to determine the attitude representation of the Bernoulli body.

### 3.2.5.1 Gravity gradient torque

The gravitational forces acting on each node are illustrated in Figure 3.12(a). The difference in the normal component of the gravitational forces results in a gravitational torque at each node, given by:

$$\vec{M}_{G,j} = (\vec{F}_{G(j)\perp} - \vec{F}_{G(j+1)\perp})L_j \tag{3.12}$$

Where $\vec{M}_{G,j}$ is the gravitational torque of $j$th beam element ($j$ =1 and 2) and $\vec{F}_{G(j)\perp}$ is a perpendicular gravitational force of the $j$th node on $j$th beam element, $\vec{F}_{G(j+1)\perp}$ is a perpendicular gravitational force of the $j$+1th node on $j$th beam element.

### 3.2.5.2 Solar radiation torque

We consider the solar rays acting on each beam element as shown in Figure 3.12 (b). The SRP torque on each beam element is generated when the perpendicular SRP forces on the two nodes on the same beam are different:

$$\vec{M}_{sun,j} = (\vec{F}_{sun(j)\perp} - \vec{F}_{sun(j+1)\perp})L_j \tag{3.13}$$

Where $\vec{M}_{sun,j}$ is the solar radiation torque of $j^{th}$ rod, $\vec{F}_{sun(j)\perp}$ is a perpendicular SRP force of the $j^{th}$ node on $j^{th}$ beam element and $\vec{F}_{sun(j+1)\perp}$ is a perpendicular SRP force of the $j+1^{th}$node on $j^{th}$ beam element.

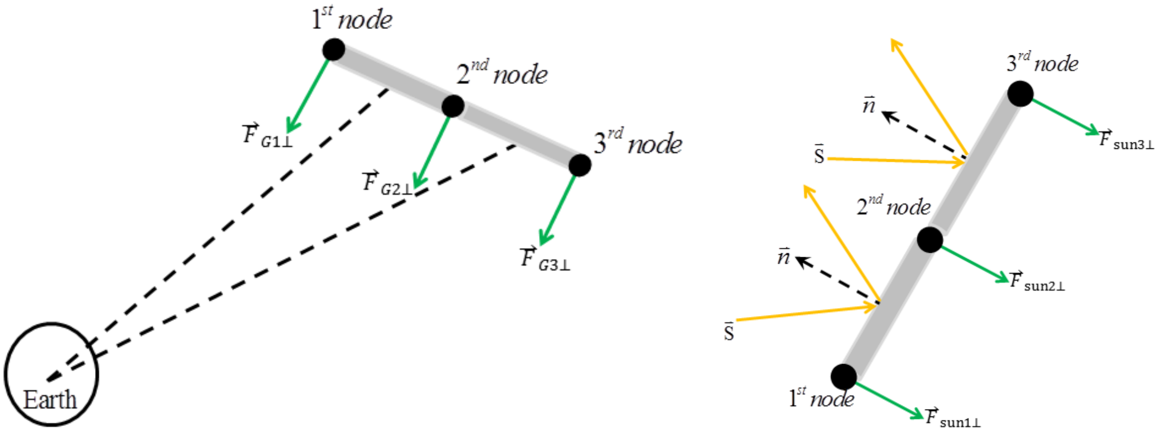

**a)** **b)**

**Figure 3.13 External torque acting on the flexible model a) Gravity gradient torque b) Solar radiation torque.**

## 3.3 Numerical Analysis

The aim of this analysis is to compare the orbit propagation of three bodies: two of which are rigid, cannonball and flat plate, and a flexible body, Bernoulli model, in GEO environment (under Earth's gravity, third body gravitations from the Sun and Moon and SRP) by using attitude and dynamics equations from chapter 2. Initial orbital parameters and initial Euler angle and angular velocities are presented in Table 3.2 and Table 3.3.

**Table 3.2 Keplerian's elements.**

| Semi-major axis(km) | Eccentricity | Inclination (degree) | Argument of perigee(degree) | Longitude of ascending node(degree) | Mean anomaly (degree) |
|---|---|---|---|---|---|
| 41,164 | 0.0001 | 2.0 | 10.0 | 3.0 | 270.0 |

**Table 3.3 The initial Euler's angle and angular velocities.**

| Euler's angle | 1st rotation ( $\psi$ ) | 2nd rotation ( $\theta$ ) | 3rd rotation ( $\phi$ ) |
|---|---|---|---|
| Angle(degree) | 5 | 20 | 10 |
| Angular velocity(degree/s) | 0 | 0 | 0 |

The initial shape is that of a flat sheet for both rigid and flexible models. All models have the same material properties [46, 47], as shown in Table 3.1.

## 3.4 Numerical Integration methods

The numerical integration to solve the propagation of the second order differential equations of orbital and attitude equations for the flexible model used here is the Runge-Kutta method in MATLAB. Since ODE45 can only solve a first order ODE. The dynamics equation of FEA has to be converted to first order ODE. We therefore introduce 2 new state variables $y_1$ and $y_2$ defined as:

$$\begin{aligned} y_1 &= \vec{U} \\ y_2 &= \dot{\vec{U}} \end{aligned} \tag{3.14}$$

Then, we take the 1st order derivative in Eq.(3.14) such that:

$$\begin{aligned} \dot{y}_1 &= \dot{\vec{U}} \\ \dot{y}_2 &= \ddot{\vec{U}} \end{aligned} \tag{3.15}$$

The above gives two new first order ODE's by substituting $\dot{\vec{U}}$ and $\ddot{\vec{U}}$ into Eq.(3.7):

$$\begin{aligned} \dot{y}_1 &= y_2 \\ \dot{y}_2 &= [M]^{-1}(\vec{F} - [K]y_1 - [C]y_2) \end{aligned} \tag{3.16}$$

Finally, we can couple with FEA with orbital dynamics are expressed:

$$\begin{aligned}
\dot{r} &= \vec{v} \\
\dot{v} &= \vec{a}_{\oplus} + \vec{a}_{\odot} + \vec{a}_{☾} + \vec{a}_{SRP} \\
\dot{y}_1 &= y_2 \\
\dot{y}_2 &= \left[M\right]^{-1}(\vec{F} - \left[K\right]y_1 - \left[C\right]y_2)
\end{aligned} \tag{3.17}$$

All simulations in this chapter are performed on a PC with CPU @ 1.80 GHz and 8GB RAM.

## 3.5 Results

Figure 3.14 shows the comparison in the evolutions of eccentricity and inclination between the two rigid bodies (cannonball (green line), flat rigid plate (blue line)) and the Bernoulli model (red line) over a period of 6 days. The inclination of the flat rigid sheet is non-periodic and the increasing rate of eccentricity evolution is the lowest. For Bernoulli model, the inclination is the same periodic as the cannonball but the amplitude is higher. The attitude motion of a flat rigid plate in Figure 3.15 is significantly slower than the results of the Bernoulli model in Figure 3.16. This is because of both gravity and SRP torques acting on the Bernoulli model while the flat rigid body is subjected only to gravity torque. According to results on the orbital dynamics of HAMR debris from Schildknecht and Scheeres [48, 49], they suggest that the rapid tumbling of a flat plate is averaged and leads to the same effective surface as a cannonball behaviour under conditions of rigid object. This is however not the case in this study. The change of cross-sectional area of the deformation of the Bernoulli model leads to provide dominant orbital prediction because different SRP forces on each beam element can support or erase the total SPR forces, which generated SRP torque. It is worthy noting that the constant cross-sectional area (cannonball) and constant area-to-mass ratio (flat rigid plate) are not good to approximate for HAMR debris. The next paragraph will describe how SPR forces vary due to the deformation of the Bernoulli model.

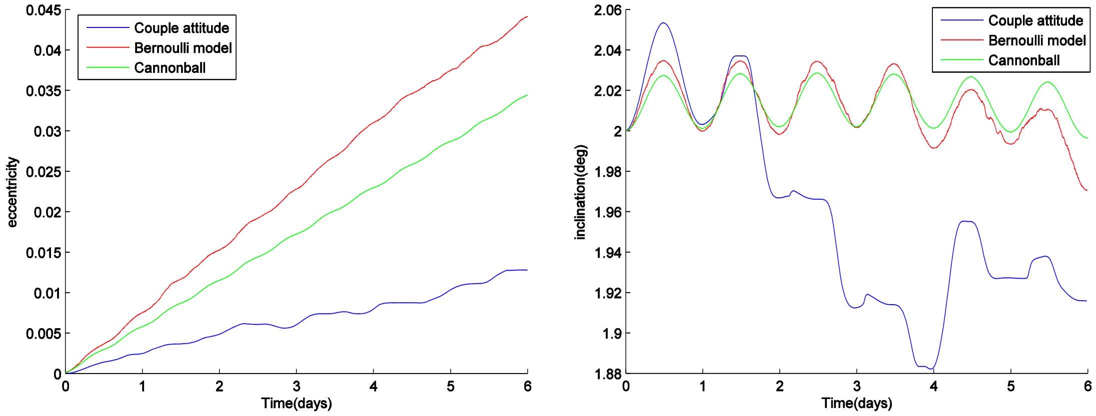

a) b)

**Figure 3.14 Comparison of inclination (a) and eccentricity (b) evolutions of Bernoulli model, flat rigid plate and cannonball under over 6 days under conservative perturbations (Earth's gravity and third body attractions from the sun and moon) and non-conservative perturbation (SRP).**

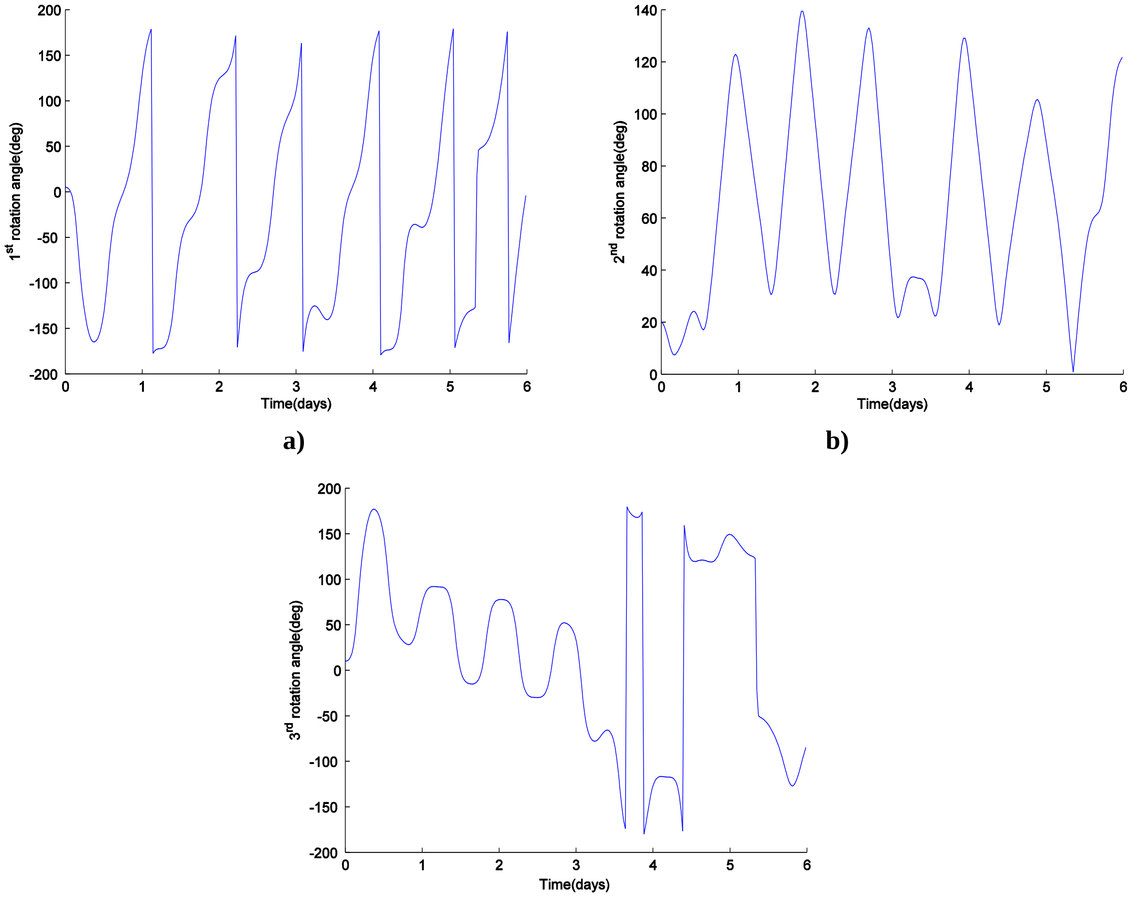

a) b)

c)

**Figure 3.15 Euler angle evolutions over 6 days of flat rigid plate under conservative perturbations and non-conservative perturbations a) the 1st Euler rotation ( $\psi$ ) b) the 2nd Euler rotation ( $\theta$ ) c) the 3rd Euler rotation ( $\phi$ ).**

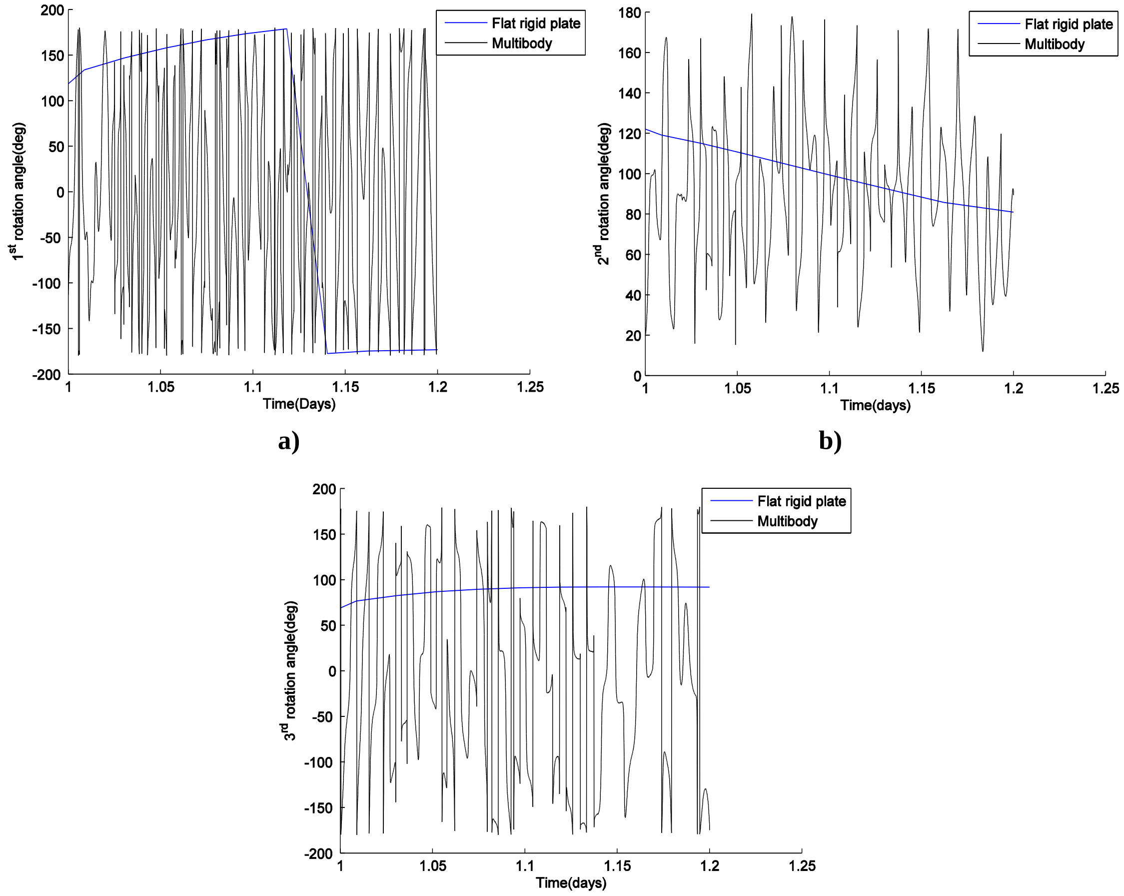

a) b)

c)

**Figure 3.16 Comparison Euler angle evolutions 1-1.2 days of both Bernoulli model and flat rigid plate under conservative perturbations and non-conservative perturbations a) the 1st Euler rotation ( $\psi$ ) b) the 2nd Euler rotation ( $\theta$ ) c) the 3rd Euler rotation ( $\phi$ ).**

Next, we analyse the behaviours of SRP forces and the deformation of the Bernoulli model by sampling 10 minutes from 6-day propagations. There are three possible directions for the sun unit vector (red arrow) to act on both beam elements. For examples, the first and second cases in Figure 3.17(a) and Figure 3.17(b) are the sun vector acting along the same sides and different sides of Bernoulli model respectively. The last case in Figure 3.17(c) shows that the sun unit vector passes through on the front side because a self-shadowing effect is being ignored at this moment. All cases lead to the different SRP acceleration acting on each beam element (blue and red lines for the 1st and 2nd beams in Figure 3.18 respectively) and the SRP summation of both beam elements (black line) are able to be supported or erased. The unbalance SRP accelerations of each beam element lead to the deformation of the model and generate SRP torque (Figure 3.18(d)), which causes a fast tumbling as shown in Figure 3.16. It is worthwhile to be noted that deformation of the Bernoulli model leads to highly vary SRP accelerations and induce SRP torque causing rapid rotation. In addition, the ignorance of a self-shadowing may lead to reduce the accuracy of prediction of both attitude and orbital motions that will be investigated in the next chapter.

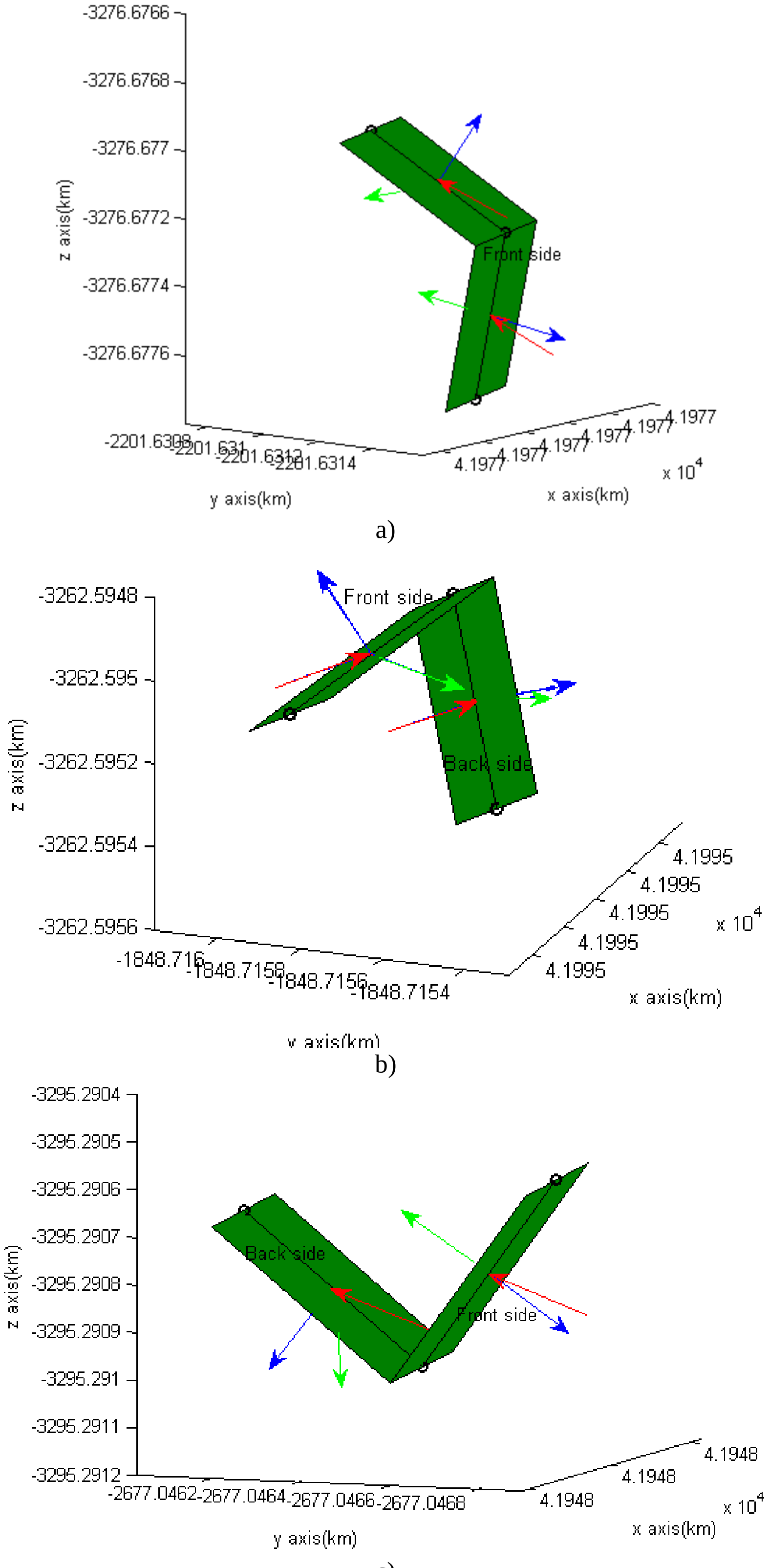

a)

b)

c)

**Figure 3.17 Some configurations of Bernoulli model over 6 days in the inertial frame a) Solar radiation acting on the same sides (1st case) b) SRP force acting on front side and back side (2nd case) c) Over SRP force on the backside due to ignorance of self-shadowing effect (3rd case). (a blue arrow is a normal unit vector, green arrow is a unit SRP force vector and red arrow is a unit sun vector).**

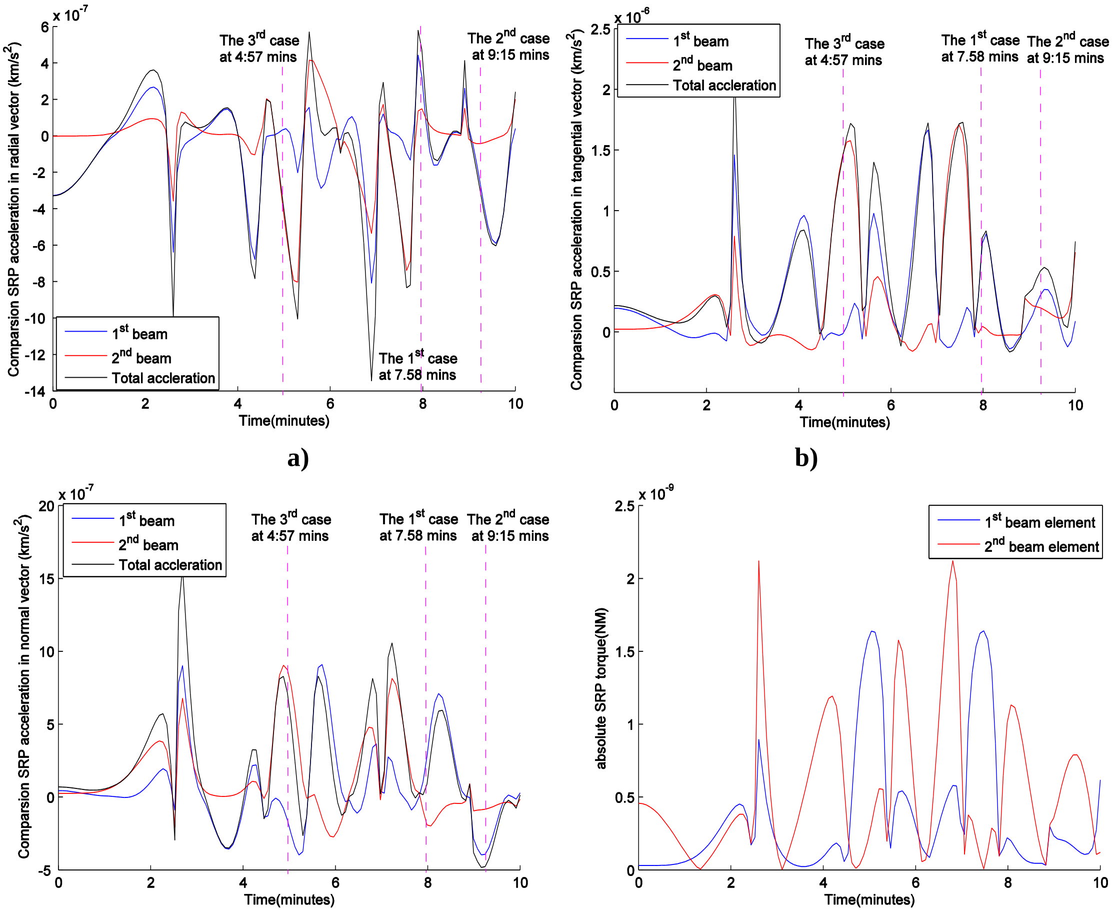

**a)** **b)**

**c)** **d)**

**Figure 3.18 The results of SRP accelerations and absolute SRP torques in radial-tangential and normal frame $(\hat{R},\hat{T},\hat{N})$ of both beam elements in 10 minutes a) radial acceleration b) tangential acceleration c) normal accelerations d) SRP torques.**

In the 100-day investigations in Figure 3.19, the eccentricity of cannonball lies between flat rigid sheet and Bernoulli model while the changed range of the inclination of the rigid flat sheet is narrow range between 1.61 and 2.03 degrees when comparing with Bernoulli model and cannonball. In overall, the prediction of orbital dynamics of Bernoulli model, which is coupled both deformation and attitude-orbit dynamics, significantly differs with rigid models due to deformed shapes. However, the computational cost of 100 days propagation is highly expensive. The CPU consumes 10.34 minutes/day evolution for CPU 1.80 GHz. It will take longer time for the propagation of many years.

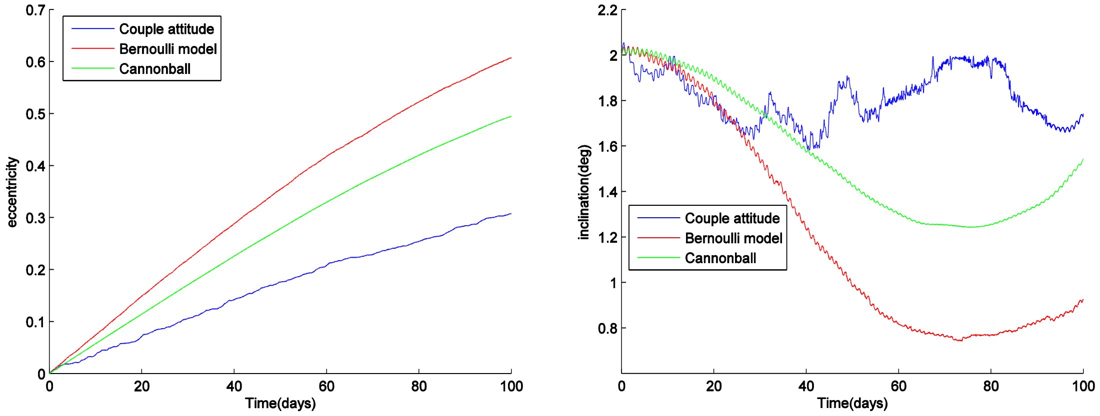

**a) b)**

**Figure 3.19 Comparison inclination and eccentricity evolution of Bernoulli model, flat rigid plate and cannonball models under over 100 days under conservative perturbations (Earth's gravity and third body attractions from the sun and moon) and non- convective perturbation (SRP) a) Eccentricity evolution b) Inclination evolution.**

## 3.6 Summary

This chapter investigated the 6 DoF motion of the flexible HAMR object based on Finite Element Analysis (Bernoulli-Euler theory) in geostationary region over short and long term periods. The material properties of all models are assumed as PET® (multilayer insulation). As a result of this study, the deformation of the object leads to fast tumbling of the Bernoulli model due to SRP torque as support the investigation from McMahon [30]. The very fast attitude motion effects to the differences of both inclination and eccentricity from both rigid objects (flat rigid plate and cannonball). However, the computational time is high cost that will consume the long propagation time when predicting over many decades, although we consider the small displacement (stiffness constant), which is loosen some accuracies of deformation dynamics effecting to attitude and orbital dynamics. Therefore, the next chapter will be introduced the flexible model based on a multibody dynamics in order to reduce the computational cost and stiffness constant by using suitable constraint equation instead. In addition, the self-shadowing effect and imperfect reflection properties will be investigated to predict attitude-orbit dynamics in over 12 and 100 days.

4

# 4 Flexible model with multibody dynamics

This chapter models the MLI debris through a systematic treatment of the dynamic behaviour of interconnected bodies. The results of this chapter include not only the prediction of the orbital evolution, but also the attitude and the deformation state of the membrane. The two substrates of MLI debris considered here are PET® and Kapton®. The orbital and attitude motions are studied under perturbations due to Earth's gravity field ($J_2$), solar radiation pressure and third body gravity from the Sun and Moon in the GEO region, and compared with the orbital dynamics of two rigid body models (cannonball and flat rigid plate) under the same environmental conditions. Due to their deformations, HAMR objects may self-shade leading to changes in the effective cross-sectional area and thus the effects of SRP. This investigation considers self-shadowing, adapting the algorithm used in the case of planar shadow projection to address planar surfaces. The last study consists of Monte Carlo simulations by varying the initial conditions (attitude dynamics and variable shape) and compares the results of the propagation of a conventional rigid body or cannonball model.

## 4.1 Flexible multibody model

A thin and highly flexible body is modelled in this chapter by using multibody dynamics and solved by means of Newtonian mechanics. The thin membrane in Figure 4.1 is modelled as a series of lump masses, interconnected with rigid rods at the centre of horizontal plate. The lump masses act as rotational joints for the plates and include rotational springs and dampers to simulate the bending stiffness of the membrane. The folding lines represented by each lump mass are all parallel to each other and the plane of deformation is described in a two-dimensional plane perpendicular to the folding lines. For this preliminary study, three lump masses are considered (Figure 4.2(a)), connected through two rigid rods in order to simplify the model and reduce the computational cost. The mass in the middle acts as a rotational hinge with spring and damper. Essentially, this model concentrates the distributed mass of the MLI sheet on lump masses, and its stiffness and damping properties on the central hinge. The sheet is assumed infinitely rigid in the plane of the membrane itself. The deformed geometry of multibody model is defined through the deformation angle ($\theta_d$) as shown in Figure 4.2(b). The dimensions are 1 x 1 m$^2$ in width and length respectively and the length of both rigid rods ($l_1 = l_2 = l$) is 0.5 m as shown in Figure 4.2.

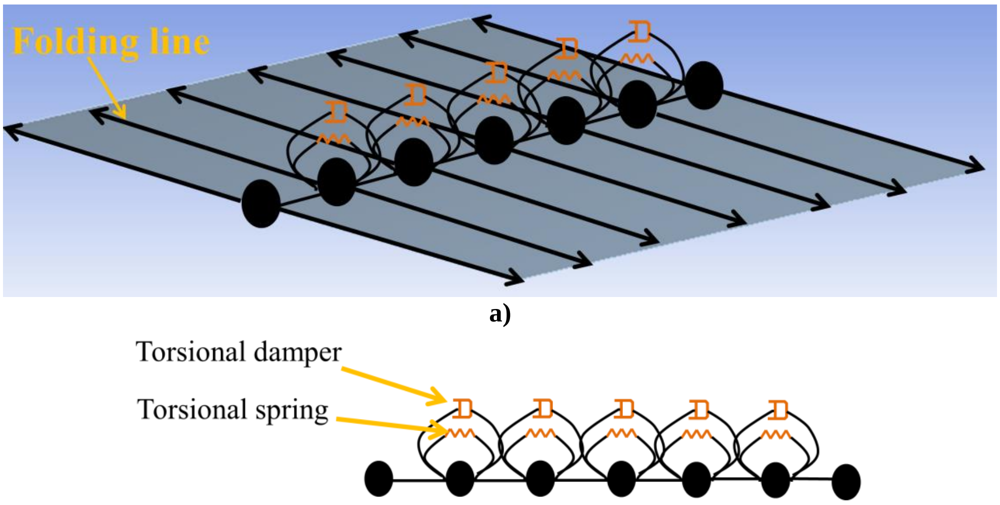

a)

b)

**Figure 4.1 Comparing a multibody model with a thin membrane a) flat plate in 3D view b) side view.**

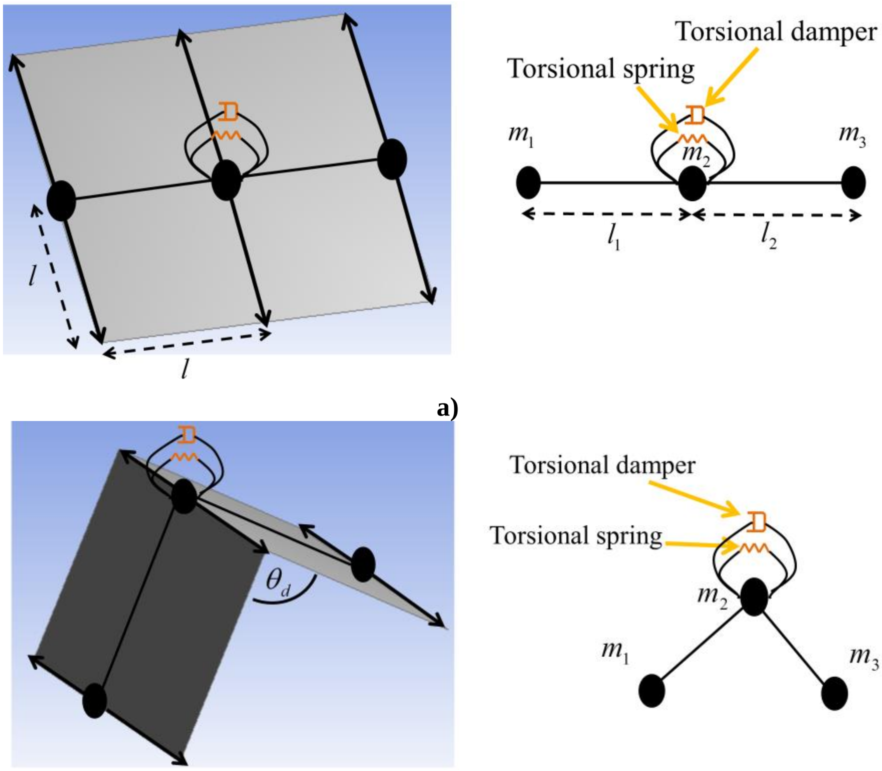

a)

b)

**Figure 4.2 Simplified models as three lump masses installed with torsional damper and spring in 3D view and side view a) flat plate shape b) deformed shape.**

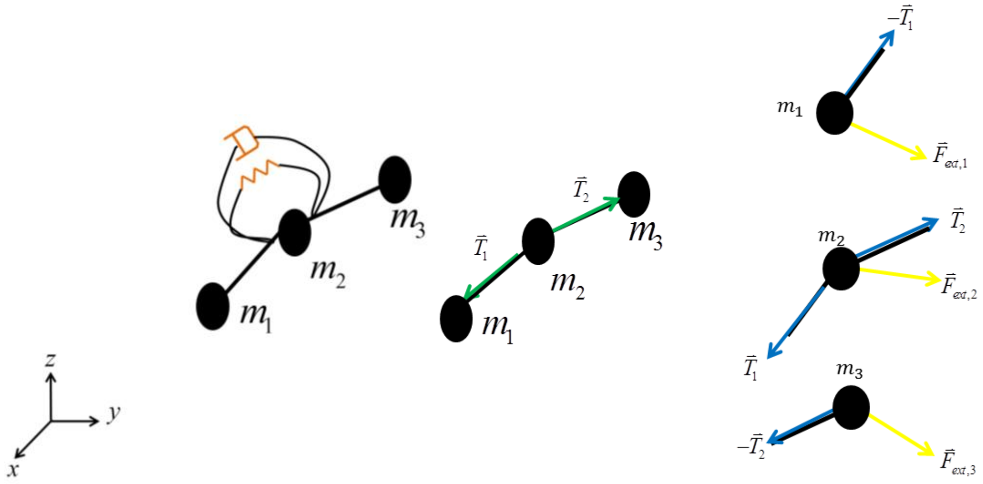

a) b)

**Figure 4.3 Multibody model a) The model in the inertial frame b) Free body diagram on each lump mass.**

To analyse the forces acting on each mass in Figure 4.3, Newton's second law of motion leads to:

$$\vec{F}_{total,1} - \vec{T}_1 = m_1 \ddot{\vec{x}}_1 \tag{4.1}$$

$$\vec{F}_{total,2} + \vec{T}_1 + \vec{T}_2 = m_2 \ddot{\vec{x}}_2 \tag{4.2}$$

$$\vec{F}_{total,3} - \vec{T}_2 = m_3 \ddot{\vec{x}}_3 \tag{4.3}$$

From these equations, we can calculate acceleration for each mass:

$$\ddot{\vec{x}}_1 = (\vec{F}_{total,1} - \vec{T}_1) / m_1 \tag{4.4}$$

$$\ddot{\vec{x}}_2 = (\vec{F}_{total,2} + \vec{T}_1 + \vec{T}_2) / m_2 \tag{4.5}$$

$$\ddot{\vec{x}}_3 = (\vec{F}_{total,3} - \vec{T}_2) / m_3 \tag{4.6}$$

Where $m_i$ is $i^{\text{th}}$ lump mass ($i$ = 1, 2 and 3), $\vec{F}_{total,i}$ is total force vector acting on the $i^{\text{th}}$ lump mass ($\vec{F}_{total,i} = \vec{F}_{ext,i} + \vec{F}_{s,i} + \vec{F}_{d,i}$), $\vec{F}_{ext,i}$ is the external force vector from conservative and non-conservative perturbations ($J_2$, SRP and the third-body from the Sun and the Moon), $\vec{T}_j$ is the tension force generated by the $j^{\text{th}}$ rod ( $j$ = 1 and 2), $\vec{F}_{s,i}$ is the rotational spring force vector of $i^{\text{th}}$ mass, $\vec{F}_{d,i}$ is the rotational damper force vector of $i^{\text{th}}$ mass, $\ddot{\vec{x}}_i$ is total acceleration vector of $i^{\text{th}}$ lump mass. The rotational spring force is:

$$\vec{F}_{s,i} = k_s \theta_d / l \qquad (4.7)$$

$$k_s = E_y I / l$$

Where $k_s$ is rotational spring constant, $E_y$ is Young modulus of material, $I$ is the moment of inertia of cross section area, $l$ is the length of rod. The rotational damping force vector is:

$$\vec{F}_{d,i} = c_s \dot{\theta}_d / l \qquad (4.8)$$

$$c_s = D_F \sqrt{M k_s}$$

Where $c_s$ is the rotational damping constant, $\dot{\theta}_d$ is angular velocity of the deformation, $D_F$ is dissipation factor of the material [50], $M$ is total mass of membrane. To enforce that the distance between the masses shall be constant (as the membrane cannot stretch in its own plane, but only bend out of it), the constraint equations is:

$$(x_{j+1} - x_j)^2 + (y_{j+1} - y_j)^2 + (z_{j+1} - z_j)^2 = l_j^{\,2} \qquad (4.9)$$

Then, the 2nd order differential of Eq.(4.9) is expressed as:

$$\begin{aligned} &2(\ddot{x}_j - \ddot{x}_{j+1})(x_j - x_{j+1}) + 2(\ddot{y}_j - \ddot{y}_{j+1})(y_j - y_{j+1}) \\ &\quad + 2(\ddot{z}_j - \ddot{z}_{j+1})(z_j - z_{j+1}) + 2(\dot{x}_j - \dot{x}_{j+1})^2 + 2(\dot{y}_j - \dot{y}_{j+1})^2 + 2(\dot{z}_j - \dot{z}_{j+1})^2 = 0 \end{aligned} \qquad (4.10)$$

Finally, in order to complete the dynamic equations, we substitute the acceleration vectors of each mass in Eq.(4.10)) in both rigid rods ( $j = 1$ and 2) to find the tension of both rods ($\vec{T}_1$ and $\vec{T}_2$) and write in matrix form as:

$$\begin{bmatrix} C_1 & C_2 \\ C_3 & C_4 \end{bmatrix} \begin{bmatrix} \vec{T}_1 \\ \vec{T}_2 \end{bmatrix} = \begin{bmatrix} A_1 \\ A_2 \end{bmatrix} \qquad (4.11)$$

Where

$$C_1 = (\vec{x}_1 - \vec{x}_2)(\frac{1}{m_1} + \frac{1}{m_2})$$
$$C_2 = -\frac{(\vec{x}_1 - \vec{x}_2)}{m_2}$$
$$C_3 = -\frac{(\vec{x}_2 - \vec{x}_3)}{m_2}$$
$$C_4 = (\vec{x}_2 - \vec{x}_3)(\frac{1}{m_2} + \frac{1}{m_3})$$
$$A_1 = -(\dot{x}_1 - \dot{x}_2)^2 - (\dot{y}_1 - \dot{y}_2)^2 - (\dot{z}_1 - \dot{z}_2)^2 - \vec{F}_{total,1}\frac{(\vec{x}_1 - \vec{x}_2)}{m_1} + \vec{F}_{total,2}\frac{(\vec{x}_1 - \vec{x}_2)}{m_2}$$
$$A_2 = -(\dot{x}_2 - \dot{x}_3)^2 - (\dot{y}_2 - \dot{y}_3)^2 - (\dot{z}_2 - \dot{z}_3)^2 - \vec{F}_{total,2}\frac{(\vec{x}_2 - \vec{x}_3)}{m_2} + \vec{F}_{total,3}\frac{(\vec{x}_2 - \vec{x}_3)}{m_3}$$

Then, we can find $\vec{T}_1$ and $\vec{T}_2$ by left-multiplying by $\left[C\right]^{-1}$

$$\begin{bmatrix} \vec{T}_1 \\ \vec{T}_2 \end{bmatrix} = \begin{bmatrix} C_1 & C_2 \\ C_3 & C_4 \end{bmatrix}^{-1} \begin{bmatrix} A_1 \\ A_2 \end{bmatrix} \tag{4.12}$$

Finally, we obtain the accelerations of each lump mass, which can be found through Eq.(4.4) - (4.6) to study the orbital evolution.

## 4.2 Model test

The first test is to analyse the deformations arising from the presence of a rotational spring and damper and then the model will be forced to simulate a movement and rotation of the multibody model. In this section, each lump mass is defined as 1 kg and the characteristic parameters for the rotational spring and damper are assumed to be $k_s$ = 0.01 N·m/rad and $c_s$ = 0.05 N·m·s/rad respectively.

### 4.2.1 Rotational spring and damper test

In order to test the rotational spring and damper of the model, it is required to set a non-flat geometry as an initial condition (triangular shape in Figure 4.4(a)). Firstly, we consider the case of spring only. The continuous oscillation of the model in Figure 4.4(b) is forced by the rotational spring. If we consider both spring and damper in Figure 4.4(c), then it can be seen that the damper reduces the amplitude of the oscillation until it motion stops completely.

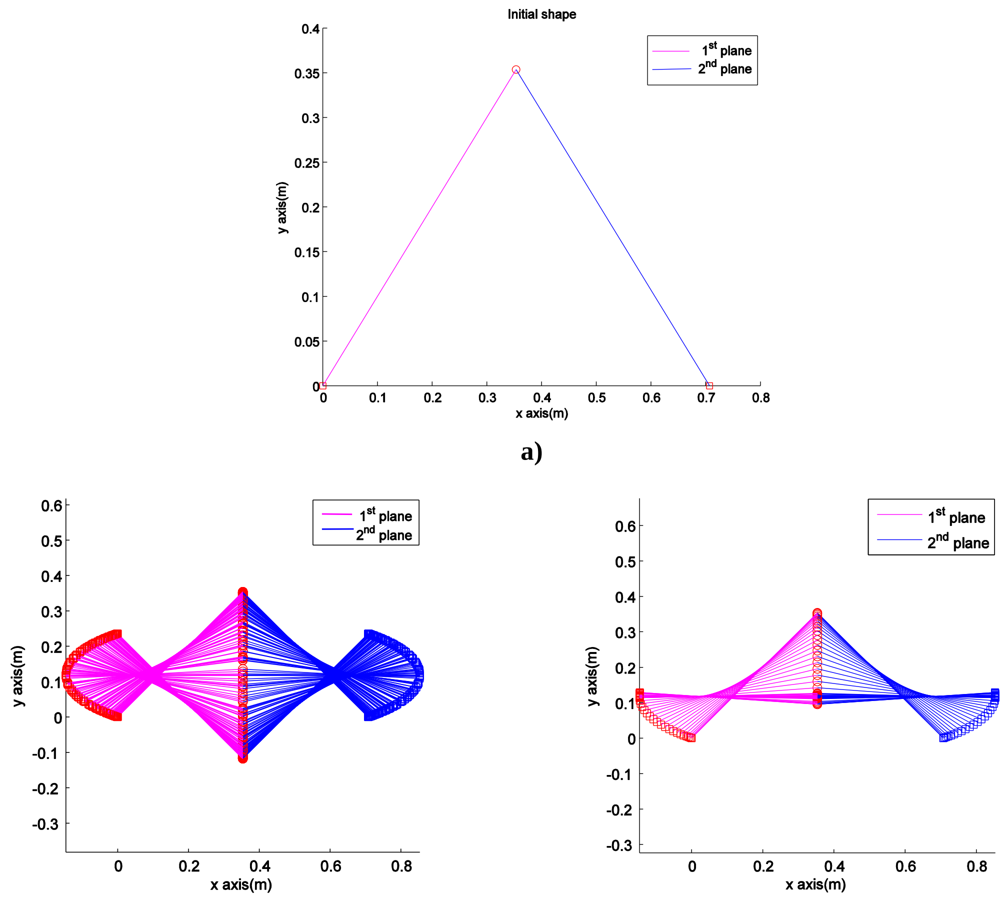

a)

b) c)

**Figure 4.4 Simulation of multibody model without external force a) initial geometry before simulation (triangular shape) b) time-lapse of the deformation when only the spring is considered, leading to continuous oscillations c) time-lapse of the deformation when both spring and damper are considered. The damper quickly reduces s the oscillation in 10 seconds (1 plot/0.1440 second).**

### 4.2.2 Displacement and rotation test

This model is tested in 4 different cases. In the first and second test (Figure 4.5 and Figure 4.6), a continuous force of 1 N in the y direction and 1 N in both x and y directions is applied. The multibody model will not show any deformation due to the fact that the same force is acting on each lump mass. The body moves in the direction of the force with increasing velocity. In the third case in Figure 4.7(a) a force of 1 N is applied for 1 second, only on the central mass in the z direction. The results show that the two plates move up and down due to the presence of the spring in Figure 4.7(b). In the last test in Figure 4.8(a) a force of 1 N is applied for 1 second in both on the first mass in both x and z directions. The results show that in this case the model rotates and translates following the applied force direction in Figure 4.8(b). The results show that the multibody model is capable of describing 7 DOFs (3 linear, 3 angular and 1 deformation) when different force vectors are acting on the lump masses.

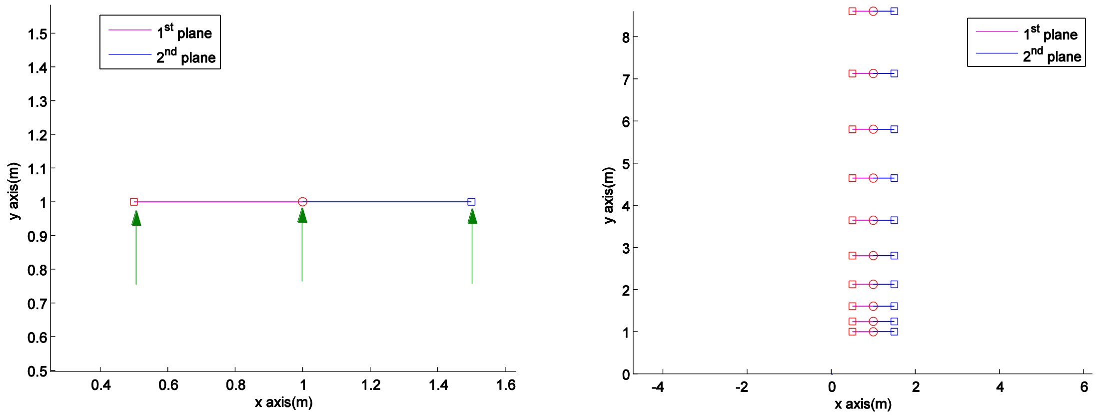

a) b)

**Figure 4.5 Simulation of multibody model in 4 seconds with external force, 1 N (green arrow) in y direction on each lump mass continuously a) initial position in 2D view b) direction of movement in 2D view (1 plot/0.6 seconds).**

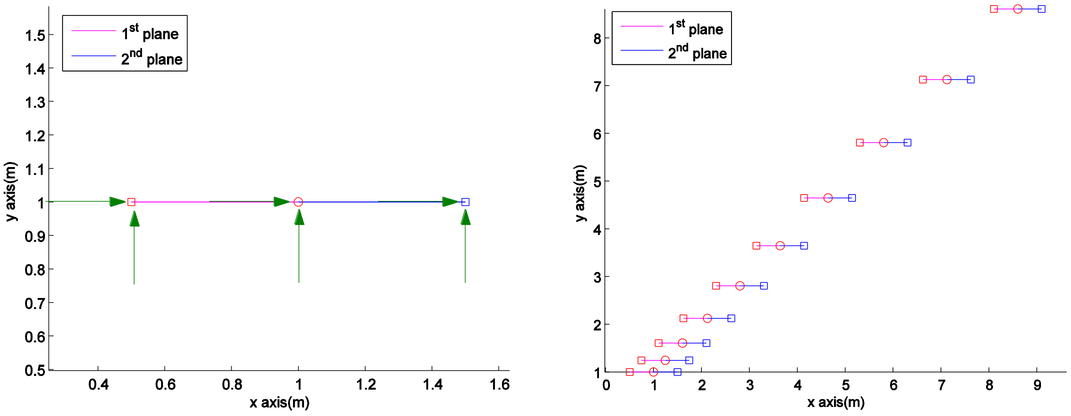

a) b)

**Figure 4.6 Simulation of multibody model in 4 seconds with external force, 1 N (green arrow) in y direction on each lump mass continuously a) initial position in 2D view b) direction of movement in 2D view (1 plot/0.6 second).**

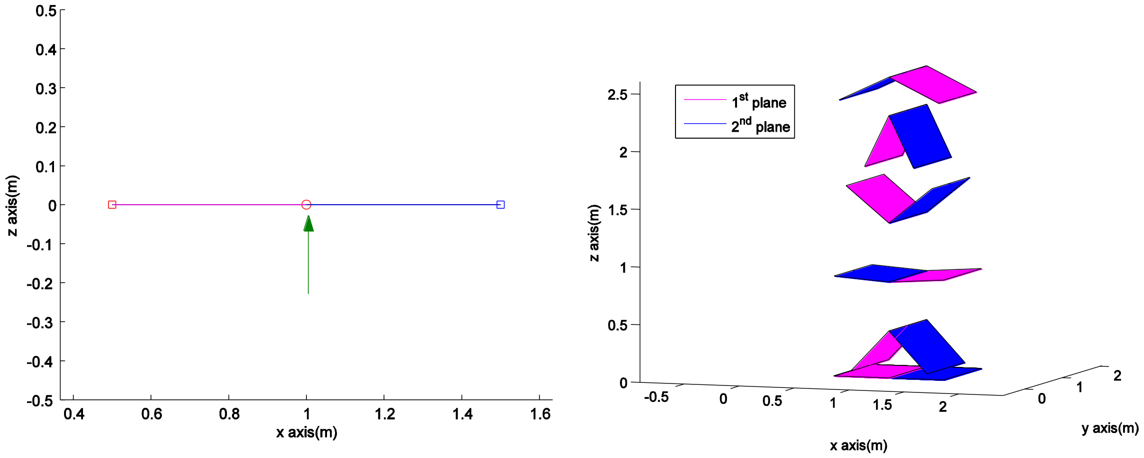

a) b)

**Figure 4.7 Simulation of multibody model for 8 seconds with external force 1 N (green arrow) for one second in x and y directions on each lump mass a) initial position in 2D view b) direction of movement in 2D view (1 plot/1.33 seconds).**

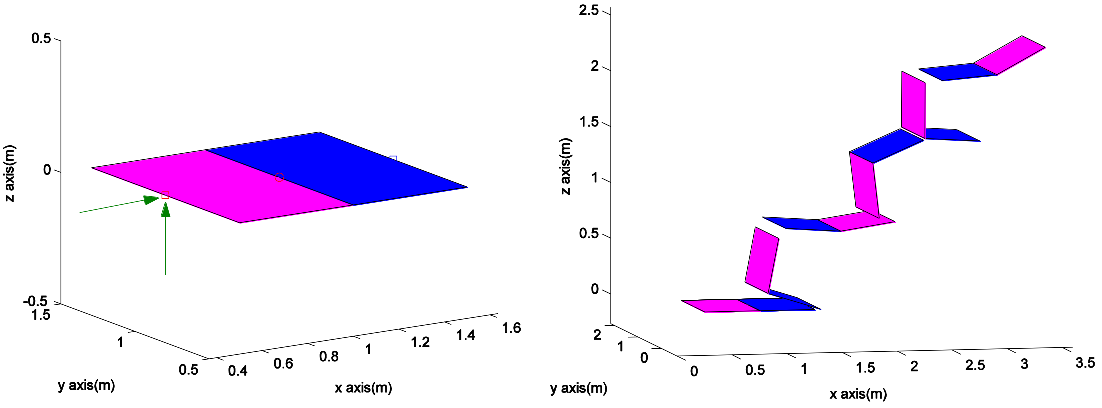

**a)** **b)**

**Figure 4.8 Simulation of multibody model in 8 seconds with external force 1 N for one second (green arrow) in x and z directions on each lump mass a) initial position in 3D view b) direction of movement in 3D view (1 plot/1.33 seconds).**

## 4.3 Modified Equinoctial Elements

The set of orbital elements, described by Gaussian variation of parameters (VOP), are chosen to study all dynamic evolutions in this chapter. This method has a singularity problem, when the eccentricity and orbital inclination equal to 1 and 90 degrees respectively. To avoid this singularity, the modified equinoctial orbital elements (MEE) [51] were introduced. The set of MEE equations are defined in terms of the equinoctial orbital elements (EQU) as follows:

$$\begin{aligned} p &= a(1-e^2) \\ f &= e\cos(\omega+\Omega) \\ g &= e\sin(\omega+\Omega) \\ h &= \tan(i/2)\sin\Omega \\ k &= \tan(i/2)\sin\Omega \\ L &= \Omega+\omega+\nu \end{aligned} \tag{4.13}$$

Where $\mu$ is gravitational constant, $a$ is the semi-major axis (km), $e$ is the eccentricity, $i$ is the inclination (degree), $\omega$ is the argument of perigee (degree), $\Omega$ is right ascension of ascending node (degree) and $\nu$ is true anomaly (degree), $p$ is semilatus rectum (km) and $L$ is true longitude (degree). The variation of the modified equinoctial elements is expressed in:

$$
\begin{aligned}
\dot{p} &= \frac{2p}{w}\sqrt{\frac{p}{\mu}}\Delta_t \\
\dot{f} &= \sqrt{\frac{p}{\mu}}\left(\Delta_r \sin L + [(w+1)\cos L + f]\frac{\Delta_t}{w} - (h\sin L - k\cos L)\frac{g\Delta_n}{w}\right) \\
\dot{g} &= \sqrt{\frac{p}{\mu}}\left(-\Delta_r \cos L + [(w+1)\cos L + g]\frac{\Delta_t}{w} - (h\sin L - k\cos L)\frac{f\Delta_n}{w}\right) \\
\dot{h} &= \sqrt{\frac{p}{\mu}}\frac{s^2}{2w}\cos L\Delta_n \\
\dot{k} &= \sqrt{\frac{p}{\mu}}\frac{s^2}{2w}\sin L\Delta_n \\
\dot{L}_i &= \sqrt{\mu p}\left(\frac{w}{p}\right)^2 + \frac{1}{w}\sqrt{\frac{p}{\mu}}(h\sin L - k\cos L)\Delta_{i,n}
\end{aligned}
\tag{4.14}
$$

Where $\Delta_r, \Delta_t, \Delta_n$ are non-two-body perturbations in the radial ($\hat{R}$), tangential ($\hat{T}$) and normal ($\hat{N}$) directions respectively, $s = \sqrt{1+h^2+k^2}$ and $w = 1 + f\cos L + g\sin L$.

## 4.4 Perturbations

In this chapter, we consider J$_2$, third body perturbations from the Sun and Moon and SRP perturbations. Therefore, the total perturbing acceleration is expressed as:

$$\vec{\Delta} = \vec{a}_{J_2} + \vec{a}_{\odot} + \vec{a}_{☾} + \vec{a}_{SRP} \tag{4.15}$$

### 4.4.1 J$_2$ perturbation

Planetary oblateness is considered through the J$_2$ harmonic [52]. The gravitational potential of the Earth due to the oblateness effect is expressed as:

$$R_{2,0} = -\frac{1}{2}\mu J_2 \frac{R_{\oplus}^2}{\vec{r}^3}(3\sin^2\varphi - 1) \tag{4.16}$$

Where $J_2$ is the 2th zonal harmonic coefficient (1.0826269x10$^{-3}$), $R_{\oplus}$ is the radius of the Earth (6,378.137 km), $\vec{r}$ is the geocentric position of the debris and $\varphi$ is the geocentric latitude of the object in the Earth fixed frame. Therefore, the 2nd differential of Eq.(4.16) are $J_2$ acceleration ($\vec{a}_{J_2}$) along each component of inertial reference frame ($\hat{I}$, $\hat{J}$, $\hat{K}$) as:

$$\begin{aligned}
a_{j2,I} &= \frac{\partial R_2}{\partial r_I} = -\frac{3\mu J_2 R_\oplus^2 r_I}{2r^5}\left(1-\frac{5r_K^2}{r^2}\right)\\
a_{j2,J} &= \frac{\partial R_2}{\partial r_J} = -\frac{3\mu J_2 R_\oplus^2 r_J}{2r^5}\left(1-\frac{5r_K^2}{r^2}\right)\\
a_{j2,K} &= \frac{\partial R_2}{\partial r_K} = -\frac{3\mu J_2 R_\oplus^2 r_K}{2r^5}\left(3-\frac{5r_K^2}{r^2}\right)
\end{aligned} \tag{4.17}$$

### 4.4.2 Solar radiation pressure of multibody model

For the multibody model based on multibody dynamics, solar radiation pressure depends on the area and its orientation with respect to the radiation coming from the Sun. The SRP equation is similar as the SRP equation using with Bernoulli-Euler model in chapter 3 by applying SRP force on lump masses instead of nodes as:

$$\vec{F}_{SRP,j} = A_j \frac{E}{c}\frac{AU^2}{\left|\vec{r}_j-\vec{r}_1\right|^2}\hat{S}_j\hat{N}_j\left((1-C_{s,j})\hat{S}_j + 2(C_{s,j}\cdot\hat{S}_j\hat{N}_j+\frac{1}{3}C_{d,j})\hat{N}_j\right) \tag{4.18}$$

Thus, the SRP acceleration of both lump masses of the $j^{\text{th}}$ rod ($\vec{a}_{SRP,j,j+1}$) can be defined as:

$$\vec{a}_{SRP,j,j+1} = \frac{\vec{F}_{SRP,j}/2}{m_{j,j+1}} \tag{4.19}$$

where $A_j$ is the cross sectional area of the $j^{\text{th}}$ rod, $m_{j,j+1}$ is the lump mass of the $j^{\text{th}}$ and $j+1^{\text{th}}$ lump mass, $E$ is the solar constant (1,353 W/m$^2$), $c$ is speed of light (299,792,458 m/s) and $C_{s,j}$, $C_{d,j}$ and $C_{a,j}$ are the coefficients for specular, diffuse reflectivity and absorption for the $j^{\text{th}}$ rod respectively. The Sun unit vector ($\hat{S}_j$) and the surface normal unit vector ($\hat{N}_j$) are required to specify the orientation of debris on the centre of pressure of the $j^{\text{th}}$ rod and $\vec{r}_j$ and $\vec{r}_1$ are the geocentric position of centre of rigid rod and the Sun respectively.

### 4.4.3 Average solar radiation pressure of rigid flat plate

The attitude motion will alter the effects of solar radiation pressure due to the changing size of the effective cross-sectional area. For flat rigid debris, the average of SRP force over the possible tumbling motion is considered and this averaged force is then propagated.

The benefits of this approach are to reduce computational cost by decoupling attitude and orbital dynamics.

In order to model a tumbling piece of debris, we can assume that any orientation in the inertial space will have equal probability of occurring. Therefore, the average force is obtained by integrating over the latitude and longitude of the Sun. It is useful to integrate in terms of a spherical coordinate frame:

$$\vec{F}_{avg} = \frac{1}{4\pi}\int_0^{\pi}\int_0^{2\pi} \vec{F}_{SRP}\, d\lambda_s\, d\delta_s \tag{4.20}$$

We set the unit Sun vector as:

$$\hat{S} = \begin{bmatrix} 1 \\ 0 \\ 0 \end{bmatrix} \tag{4.21}$$

And a general normal vector can be described as:

$$\hat{N} = \begin{bmatrix} \cos\lambda_s \sin\delta_s \\ \sin\lambda_s \sin\delta_s \\ \cos\delta_s \end{bmatrix} \tag{4.22}$$

Therefore, the equivalent area is expressed:

$$A_{eq} = \frac{\vec{F}_{avg}}{P_{SP}} \tag{4.23}$$

Where $P_{SP} = \frac{E}{c}$ is solar radiation pressure per square unit metre.

Then, the average SRP acceleration of the flat rigid sheet can be calculated as:

$$\vec{a}_{AVG} = -\frac{A_{eq}}{M} P_{SP}\hat{\vec{S}} \tag{4.24}$$

However, the disadvantage of the spherical integration coordinates is that when we perform to integrate on the two angles, the results of points are not uniform distributions on the sphere surface but they are concentrated on the pole, which may reduce some of all possible solar latitude and longitude that effects the value of average SRP force [53].

## 4.5 Self-shadowing

There are three main methods commonly used in real-time 3D computer graphics to represent shadowing effects. These are: planar shadow, shadow volume and shadowing mapping. In this thesis, the planar shadow method, first developed by Blinn [54] is applied to generate shadows by projecting the shadow casting object's polygons onto a plane. This method is suitable to calculate self-shadowing of the multibody model because it is the easiest and fastest to implement and the multibody model has a simple geometry but the disadvantage of a shadow casted on a plane does not create soft shadow (penumbra), which SRP will not be nil because of partial illumination. In Figure 4.9, the point ( $\vec{p}$ ) is the projection of each vertex ($\vec{v}$) onto the plane P: $\vec{n}_p \cdot \vec{x}_p + d_p = 0$ due to a light source vector ($\vec{l}$). The shadow cast the on plane can be defined as:

$$\vec{p} = \vec{l} - \frac{d + \vec{n} \cdot \vec{l}}{\vec{n} \cdot (\vec{v} - \vec{l})}(\vec{v} - \vec{l}) \tag{4.25}$$

This can be written into a projection matrix ( $\vec{p} = M\vec{v}$ ) [55].

$$M = \begin{bmatrix} n.l + d - l_x n_x & -l_x n_y & -l_x n_z & -l_x d \\ -l_y n_x & n.l + d - l_y n_y & -l_y n_z & -l_y d \\ -l_z n_x & -l_z n_y & n.l + d - l_z n_z & -l_z d \\ -n_x & -n_y & -n_z & n.l \end{bmatrix} \tag{4.26}$$

The self-shadowing algorithm has two main steps. Firstly, when two planes are oriented in space, it will perform a check to determine which plane, if any, casts a shadow on the other. The vector from the Sun to the centre of mass on the plane will determined which plane is closer to it. The algorithm then determines if an area of the plane is exposed to SRP by checking the intersection between the shadow and the plane. In case of the non-intersection, SRP forces of both planes are normally calculated. This algorithm is calculated at each integration step.

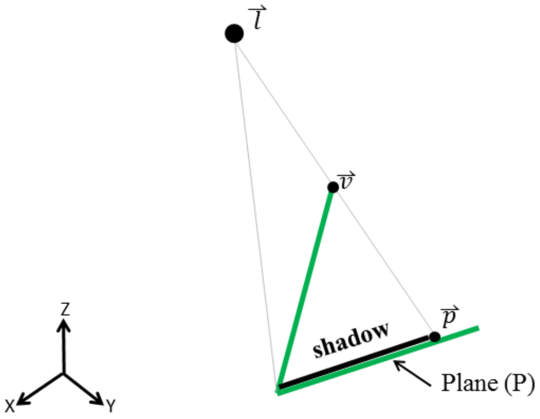

Figure 4.9 Planar shadow projection.

Figure 4.10(a) presents a self-shadowing simulation test. The above plane (pink: 1st plane) acts as a shading plane. The bottom plane (blue: 2nd plane) has a shadow (grey) cast upon its surface. The light source is at coordinates (5, 1, 4) in x, y, z axis. The shaded area depends on the position of the light source and the object's shape. Figure 4.10(b) and Figure 4.10(c) show different shadows created by moving the light source coordinates at (5, -1, 2) and (-1, 0, 4.5) as well as the orientation of the object. It can clearly be seen that different orientations and relative positions cause significant changes in the solar radiation pressure on a shaded plane.

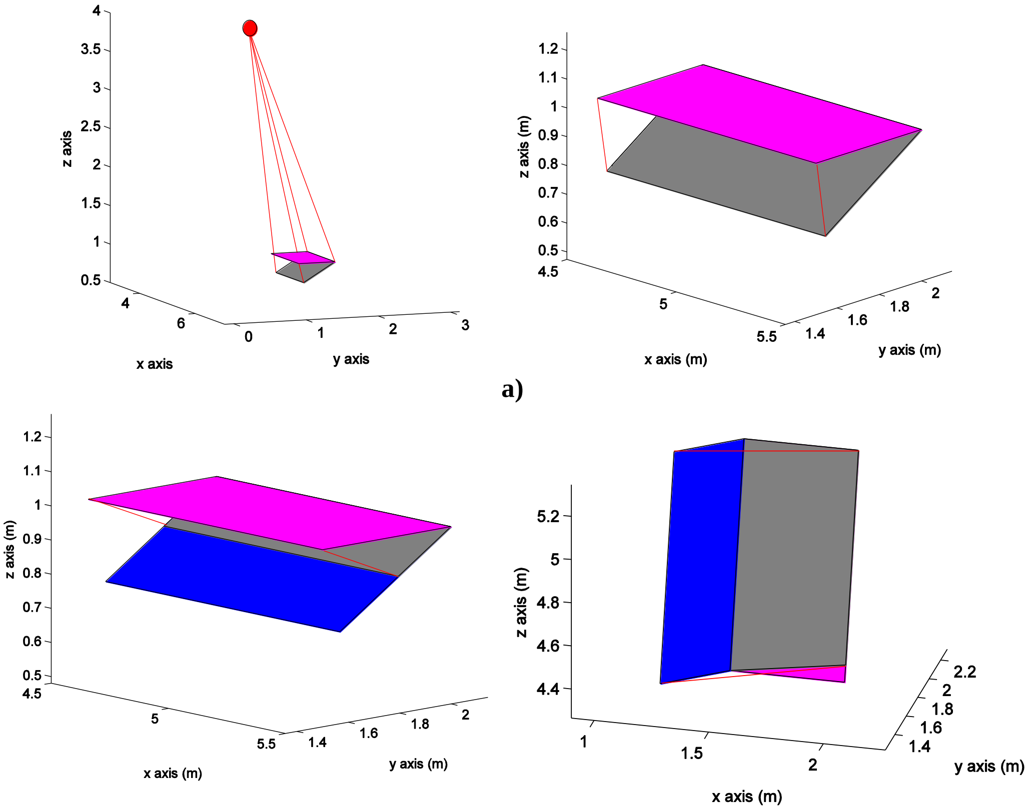

a)

b)

c)

Figure 4.10 Self-shadowing area simulations a) light source above the model and full shadow on the second plane b) shadow area after moving light source position c) shadow area after rotating.

## 4.6 Simulation Analysis

Two different kinds of MLI [18] are selected for analysis: PET® and Kapton®. PET® (perfect reflection properties) is coated aluminium on both sides while Kapton® is coated only on one side (imperfect reflection properties) as shown in Figure 4.11. There are three models types considered for these investigations (cannonball, flat rigid plate and multibody). The material properties are listed in

Table 4.1 and the initial geometries of both rigid flat plate and multibody model are assumed to be that of a flat sheet (Figure 4.11). All objects start with the same set of Keplerian elements as shown in Table 4.2 and the starting date of the simulation is the same used in section 2.1.2 of chapter 2. Initial Euler angles measured at the second lump mass that is assumed to be the origin of body frame of reference are chosen to be 50, 9 and 85 degrees (3-1-3 rotation sequence) respectively and the initial angular velocity set to zero for all components. The attitude dynamics of the multibody model refers to the attitude dynamic first presented in section 3.2.4 of chapter 3. The numerical integration used to solve the differential equations in this study is the ODE45 in MATLAB®.

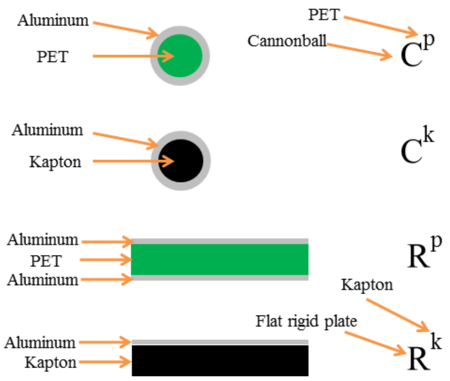

**Figure 4.11 Cross-sectional objects of cannonball model and flat rigid object.**

**Table 4.1 Properties of PET and Kapton [18]**

| Material type | | AMR [m$^2$/kg] | Young's Modulus ($E$) [N/m$^2$] | $C_{Rs}$ , $C_{Rd}$ , $C_{Ra}$ | $k_s$ (N · m/rad) | $c_s$ (N · m · s/rad) |
|---|---|---|---|---|---|---|
| PET | Coated | 111.11 | 8.81x10$^9$ | 0.60 0.26 0.14 | 0.0043 | 1.2388E-05 |
| Kapton | Coated | 26.30 | 2.50x10$^9$ | 0.60 0.26 0.14 | 0.0051 | 1.3904E-05 |
| | uncoated | 26.30 | | 0.00 0.10 0.90 | | |

**Table 4.2 Initial orbital elements.**

| Semi-major axis(km) | Eccentricity | Inclination (degrees) | Argument of perigee(degrees) | Longitude of ascending node(degrees)) | Mean anomaly (degrees) |
|---|---|---|---|---|---|
| 41,254 | 0.0001 | 5.0 | 9.0 | 30.0 | 270.0 |

The orbital and attitude evolutions of both debris models have been investigated under selected perturbation regimes. $J_2$ perturbation only is labelled with subscript "j", the third body gravitational perturbations from the Sun and the moon are labelled with subscript "g", while SRP force is labelled with subscript "s". Self-shadowing of multibody model is denoted by subscript "h". The capital letters "C", "R" and "M" indicate the cannonball model, rigid body and multibody body respectively. The material of the model is labelled with superscript "p" and "k" standing for PET® and Kapton® respectively. The summary of the objects and their characteristics used in the numerical simulations is shown in Table 4.3.

**Table 4.3 Summary of letters to describe simulated objects.**

| Model | Letter | Material | Superscript | Perturbations | Subscript |
|---|---|---|---|---|---|
| Cannonball | C | PET | p | $J_2$ | j |
| Rigid flat sheet | R | Kapton | k | Third body | g |
| Multibody model | M | | | SRP | s |
| | | | | Shadow effect | h |

## 4.7 Results and Discussion

In this section, we present the physical dynamics and orbital parameters of the multibody model and compare that with the flat rigid sheet and cannonball model (reference object) for two material types (PET® and Kapton®) over a period of 12 days. In order to analyse the effects of each perturbation, we investigate three scenarios: $J_2$ and SRP, gravitational ($J_2$ and third body) and finally consider all perturbations. All investigations are simulated with a personal PC CPU @ 1.80 GHz. Then, in order to investigate different initial conditions for the attitude dynamics and deformed shape, Monte Carlo simulations with 300 different initial conditions are run on a Linux-based parallel computing cluster with 50 processor cores.

### 4.7.1 Dynamics under $J_2$ and solar radiation pressure

Figure 4.12 shows the dynamical evolution for the PET® over 12 days for four different scenarios: $M_{js}^{p}$, $M_{js,h}^{p}$, $R_{js}^{p}$ and $C_{js}^{p}$. The variations of the orbital elements are significantly different for each object. Both eccentricity of $M_{js}^{p}$ and $M_{js,h}^{p}$ lie between $C_{js}^{p}$ and $R_{js}^{p}$ while the inclination of $C_{js}^{p}$ show the largest amplitudes in variations of inclination. It can be seen that the inclination of $M_{js}^{p}$ and $M_{js,h}^{p}$ present almost similar periodic behaviours. The reason for this is that the SRP accelerations of multibody model depends on variations of the effective cross-section area throughout the orbital revolution due to tumbling and self-shading effect while the SRP accelerations of both rigid bodies are caused only by the varying distance to the Sun, which does not significantly change in the short period of the simulation.

In the same simulation with Kapton® ($M_{js}^{k}$, $M_{js,h}^{k}$, $R_{js}^{k}$ and $C_{js}^{k}$), Figure 4.13 shows that the orbital evolutions of the $C_{js}^{k}$ exhibits the highest secular trend in eccentricity and the largest amplitude in variations of the inclination. It is, therefore, worthy to note that cannonball model is not suitable to approximate the orbital motion of an object with imperfect reflection properties. The inclination evolutions of $M_{js}^{k}$ and $M_{js,h}^{k}$ are larger than $R_{js}^{k}$ due to variations in the effective cross sectional area of the flexible model as the previously mentioned for the case of PET®. Comparing both material types for the multibody model, the evolutions of Kapton® are obviously smaller due to AMR, which is around 5 times lower and imperfect reflection properties.

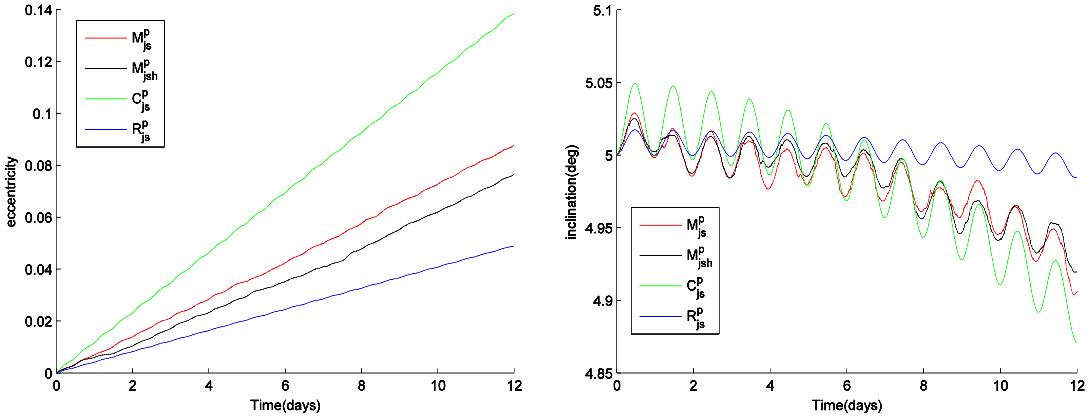

**Figure 4.12 Comparison in eccentricity and inclination evolution of $M_{js}^{p}$, $M_{js,h}^{p}$, $R_{js}^{p}$ and $C_{js}^{p}$ under $J_2$ and solar radiation pressure over 12 days.**

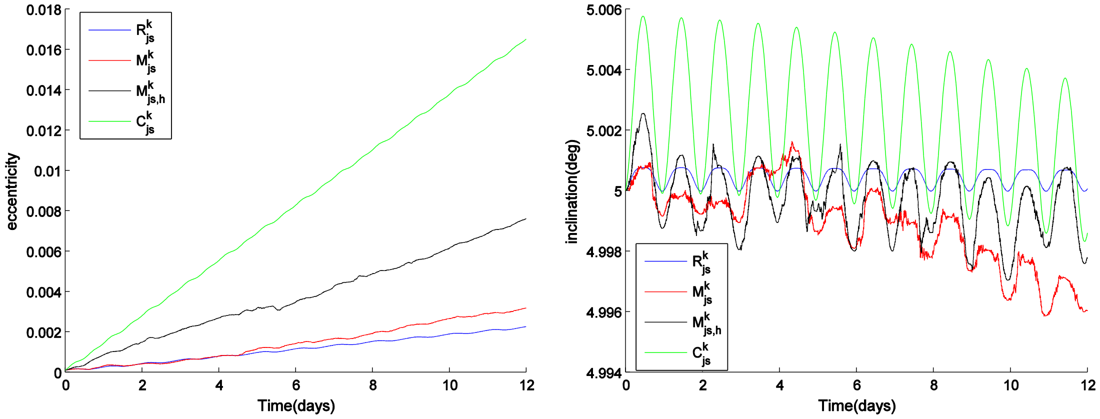

**Figure 4.13 Comparison in eccentricity and inclination evolutions of $M^k_{js}$, $M^k_{js,h}$, $R^k_{js}$ and $C^k_{js}$ under J$_2$ and solar radiation pressure over 12 days.**

In order to better understand the dynamics of the multibody model, we restrict the time of the investigation to 10 minutes and start from the same initial configuration in Figure 4.14 (deformed angle: 30 degrees) and same initial positions and velocities for both PET® and Kapton®. Figure 4.15(a) shows the physical dynamics of $M^p_{js}$ without considering the self-shadowing effect. In this case, the absolute accelerations of both planes ($M^p_{js}$) in Figure 4.15(b) do not reach zero. Comparing with the evolution of $M^p_{js,h}$ in Figure 4.16(a), we can notice that the self-shadowing effect leads to different deformation and tumbling when comparing with $M^p_{js}$. The first plane, $M^p_{js,h}$ is not exposed to direct solar radiation pressure due to self-shadowing effect and the overall absolute accelerations of both planes in Figure 4.16(b) show a null or small accelerations. The rotations of $M^p_{js}$ is different when comparing the rotations of $M^p_{js,h}$ as shown in Figure 4.15(c) and Figure 4.16 (c) respectively. Self-shading effect causes both different deformations and unique rapid non-stable attitude motion of $M^p_{js}$ and $M^p_{js,h}$. This is due to the fact that self-shadowing reduces the amount of SRP acting one side of the plate leading to a difference in the force vectors between the two sides.

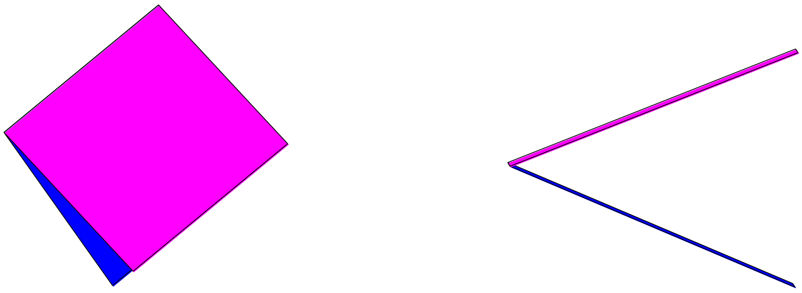

a) b)

**Figure 4.14 Initial geometry in the inertial frame of investigation in 10 minutes under $J_2$ and solar radiation pressure a) 2D view b) side view.**

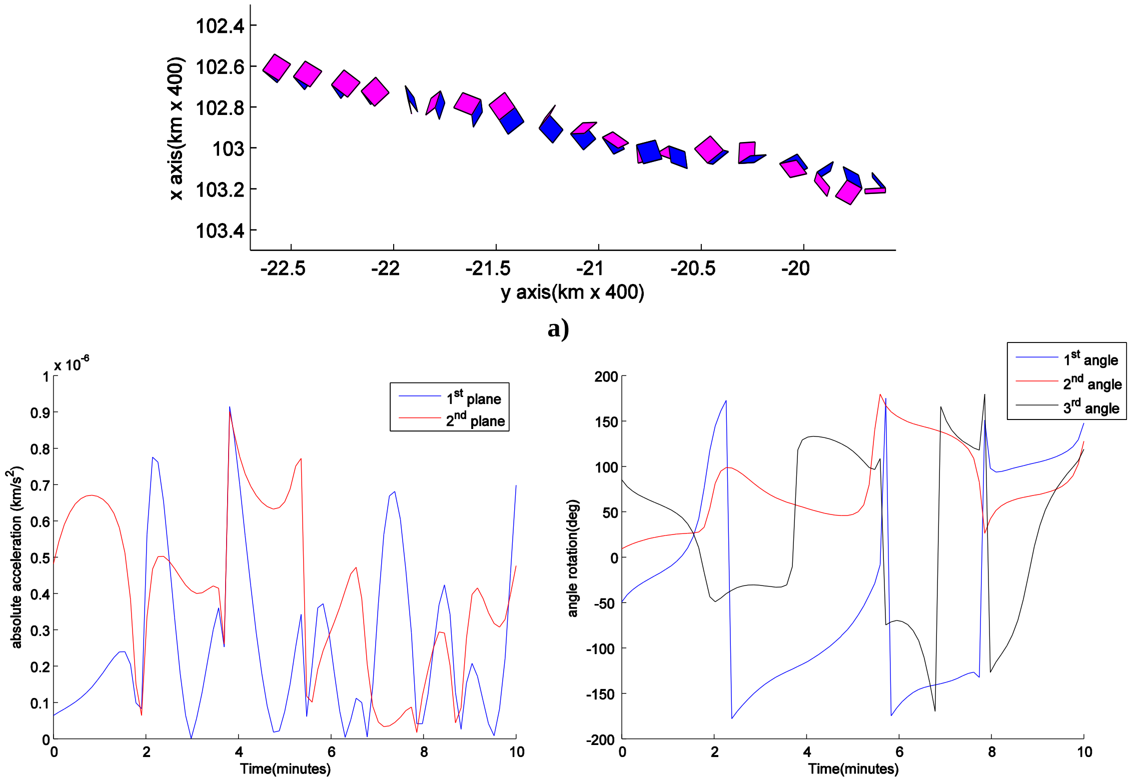

a)

b) c)

**Figure 4.15 Simulation results of PET® under $J_2$ and solar radiation pressure without self-shadowing ( $M_{js}^{p}$ ) in 10 minutes a) time-lapse of deformation in the inertial frame (1 plot/ 30 seconds) b) absolute acceleration of both planes c) Euler angle evolution.**

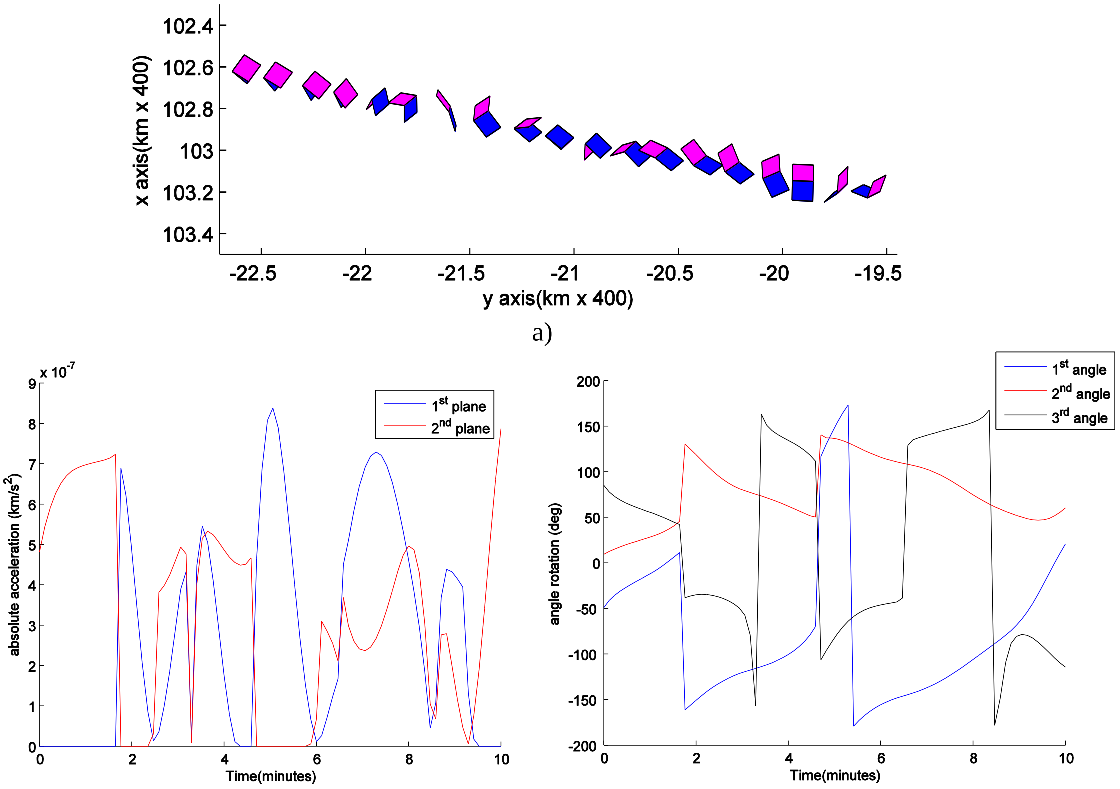

a)

b)

c)

**Figure 4.16 Simulation results of PET® under $J_2$ and solar radiation pressure with self-shadowing ($M_{js,h}^{p}$) in 10 minutes a) time-lapse of deformation in the inertial frame (1 plot/ 30 seconds) b) absolute acceleration of both planes c) Euler angle evolution.**

The analysis of the motion of Kapton® model under the effects of $J_2$ and SRP over a period of 10 minutes is shown in Figure 4.17 and Figure 4.18. Due to the non-uniform reflection properties of Kapton®, the front surface is coated with highly reflective aluminium while the back side does not have any coating and hence has significantly lower reflectivity. There are three possible scenarios for the perturbations forces acting on the model. Firstly, the SRP acts on the aluminium-coated surfaces and the object moves subject to both SRP and $J_2$ perturbations. Secondly, if SRP acts on the uncoated sides then the motion of the object is dominated by gravitational perturbation rather than SRP. Lastly, when SRP acts on the coated side of one plane and non-coated side of another one, then the effect on the two planes is going to be significantly different. This leads to the deformation of the geometry and rotations as shown in Figure 4.17(a). This mechanism is similar to the self-shadowing effect. Comparing the absolute acceleration of both $M_{js}^{k}$ and $M_{js,h}^{k}$, the complete shading plane ($M_{js,h}^{k}$) on the first plane in Figure 4.18(b) is found at the start due to zero absolute acceleration as initial conditions while $M_{js}^{k}$, shows that SRP forces acts on both planes. These mechanisms of self-shadowing are as similar to the case of PET® in the previous case study.

To summarise, the short term period analysis of both PET® and Kapton®, the self-shadowing causes a variation in the SRP forces acting on the body which results in different deformations and tumbling of the multibody model when compared to the results without considering self-shadowing effects. The rotation of $M^{p}_{js,h}$ is however faster than $M^{k}_{js,h}$ due to lighter weight and uniform reflection properties.

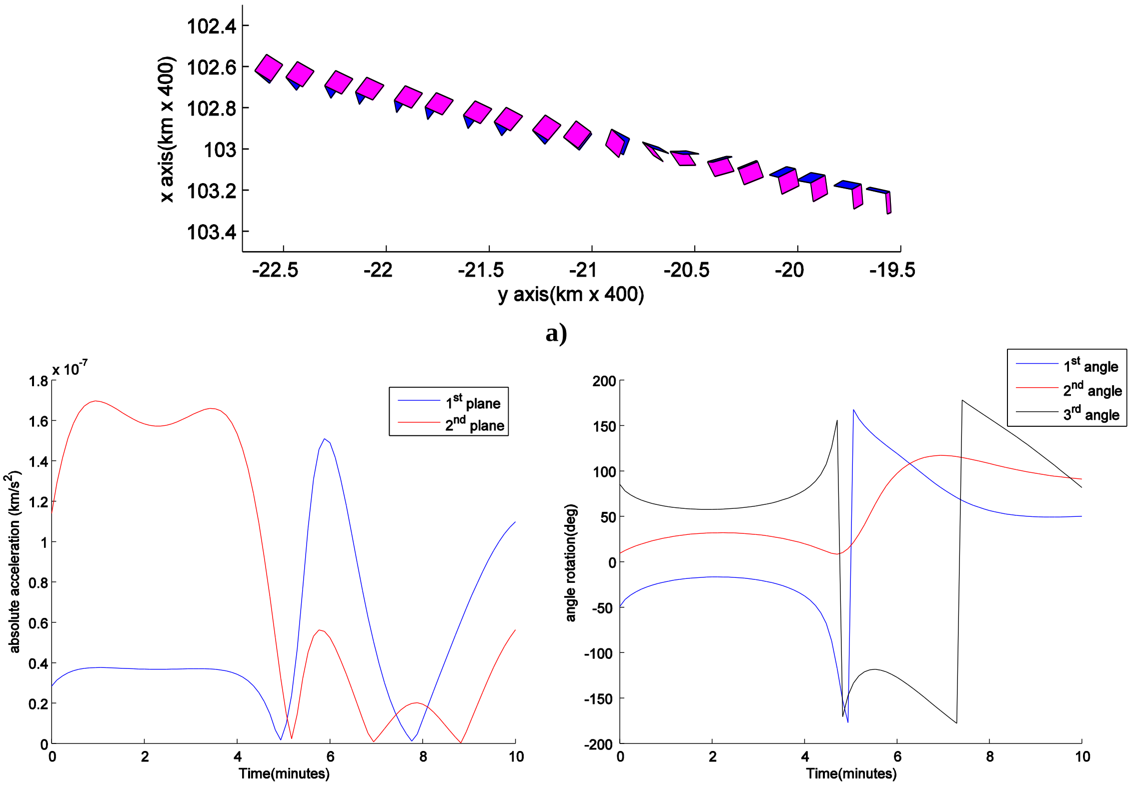

a)

b) c)

**Figure 4.17 Simulation results of Kapton® under $J_2$ and solar radiation pressure without self-shadowing ($M^{k}_{js}$) in 10 minutes a) time-lapse of deformation in inertial frame (1 plot/ 30 seconds) b) absolute acceleration of both planes c) Euler angle evolution.**

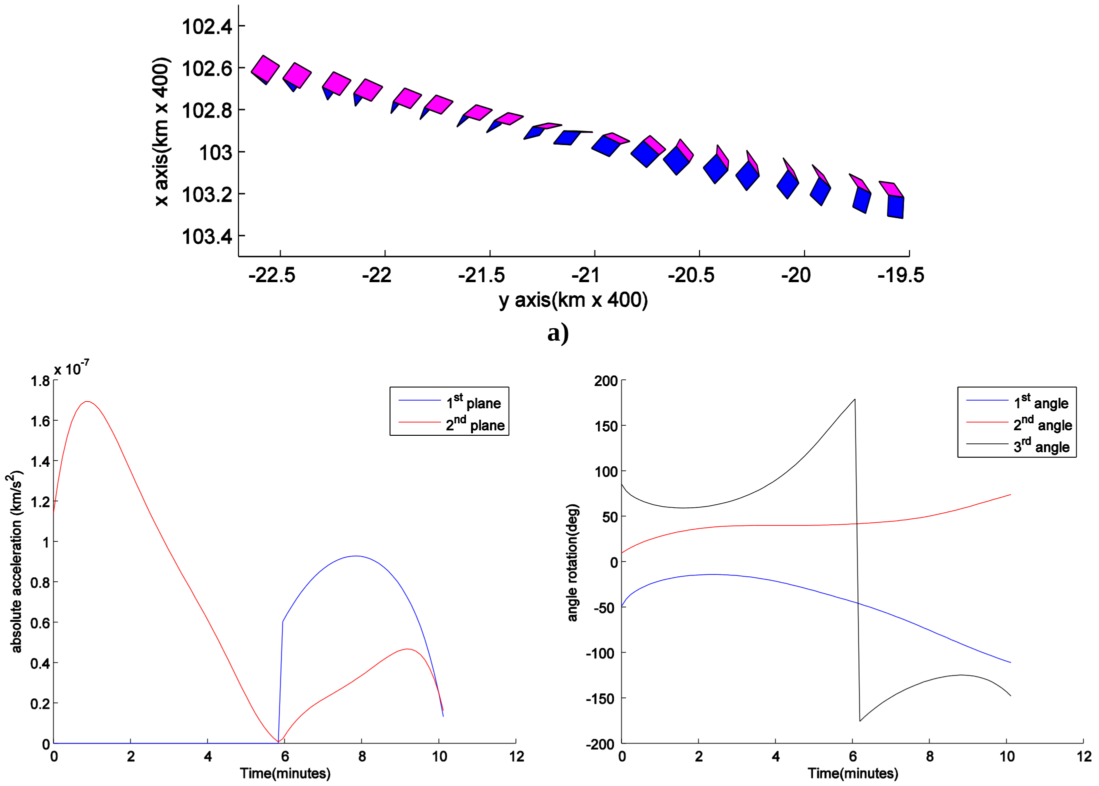

a)

a) b)

**Figure 4.18 Simulation results of Kapton® under $J_2$ and solar radiation pressure with self-shadowing ($M^k_{js,h}$) in 10 minutes a) time-lapse of deformation in inertial frame (1 plot/ 30 seconds) b) absolute acceleration of both planes c) Euler angle evolution.**

### 4.7.2 Effective cross-section area under $J_2$ and solar radiation pressure

The change of effective cross-section area alters the variations in the incidence angles on a debris surface thus leading to the attitude dynamics of debris. Figure 4.19(a) and Figure 4.19(b) show the propagations of effective cross-section area over a period of 10 minutes of PET® ($M^p_{js}$, $M^p_{js,h}$ and $R^p_{js}$) and Kapton® ($M^k_{js}$, $M^k_{js,h}$ and $R^k_{js}$) under $J_2$ and SRP disturbances. The effective cross-section areas of the rigid model ($R^p_{js}$ and $R^k_{js}$) are calculated by averaging all possible attitudes of effective area over solar latitude and longitude leading to both average exposed area values of 0.1747 m$^2$ and 0.1040 m$^2$ respectively. The equivalent area of $R^k_{js}$ is around 1.6 times smaller due to imperfect reflection properties. For the multibody model, the effective cross-section areas are the summation of the effective cross-section area of both planes due to their rotations.

Analysing the effects of self-shadowing in Figure 4.19, it can be seen that the effective cross-sectional area with self-shadowing differs significantly from that with non-self-shadowing for both PET® and Kapton®. The rate of change of the effective cross-section area of $M^p_{js}$ and $M^p_{js,h}$ in Figure 4.19(a) fluctuates more rapidly than that of $M^k_{js}$ and $M^k_{js,h}$

in Figure 4.19(b). The highest value of effective cross-sectional area indicates that the SRP vector acts almost perpendicularly to the debris plane while the lowest value corresponds to the debris plane being almost parallel to SRP vector. These results are in accordance with the unstable attitude motion and variations in SRP accelerations discussed in previous section.

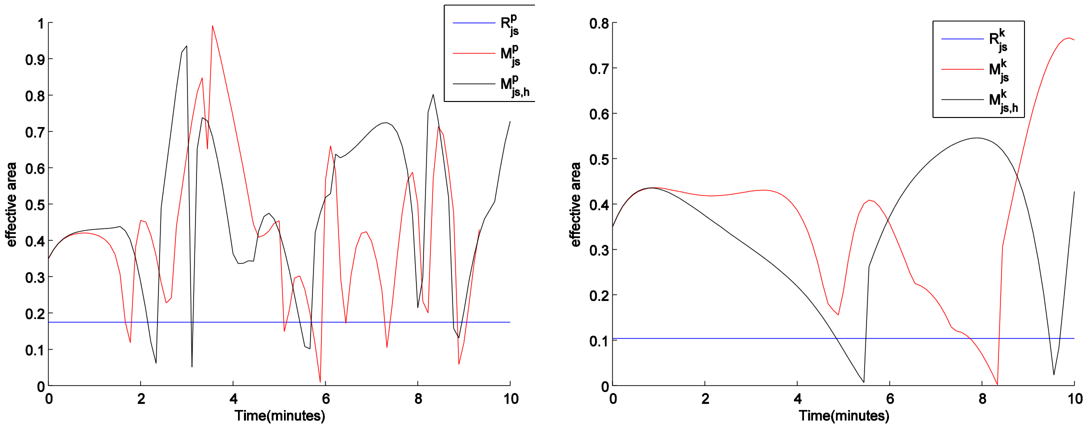

**a) b)**

**Figure 4.19 Comparison in variations of effective cross-section area under $J_2$ and solar radiation pressure in 10 minutes a) PET® b) Kapton®.**

### 4.7.3 Dynamics under $J_2$ and luni-solar third body perturbations

Figure 4.20(a) and Figure 4.20(b) show that there are very small changes in both inclination and eccentricity of $M_{jg}^{p}$, $R_{jg}^{p}$, $M_{jg}^{k}$ and $R_{jg}^{k}$. Figure 4.20(c) and Figure 4.20(d) shows the difference in inclination and eccentricity of both materials in the order of $10^{-5}$ and $10^{-8}$ respectively when applied to the flat rigid plate model. While the changes for the eccentricity appear to be bounded, the inclination change suggests a secular trend. It would suggest that the gravitational effects insignificantly change in the orbital dynamic of multibody model when comparing with cannonball. For the simulation of the deformation dynamics, Figure 4.21 shows a spin of $M_{jg}^{p}$. The cause for this behaviour is that the gravity gradient torque acts with sufficiently difference on each lump mass. This leads to the deformation of the body and the tumbling motion (Figure 4.21(b)-Figure 4.21(c)).

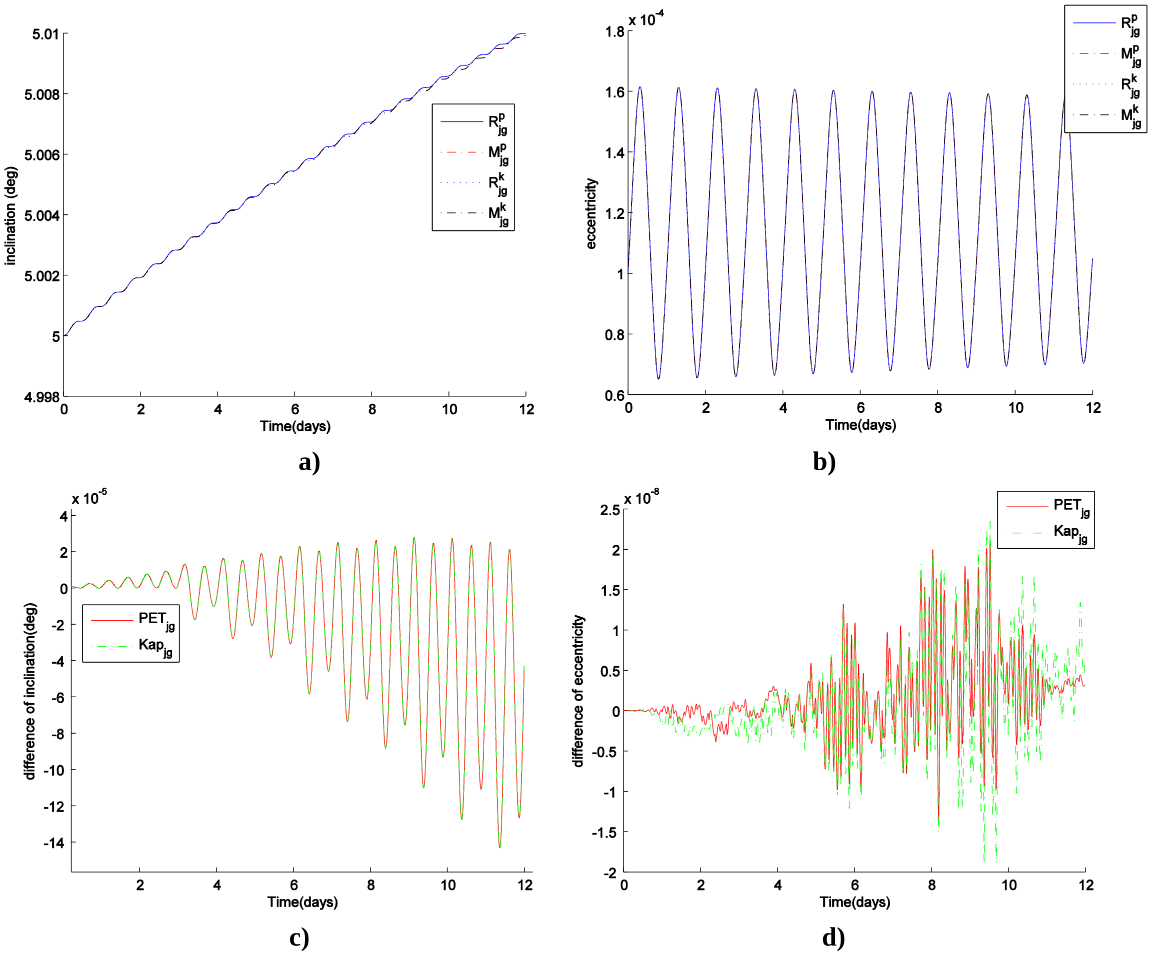

a) b)

c) d)

**Figure 4.20 Comparison inclination and eccentricity evolution of $M_{jg}^{p}$, $R_{jg}^{p}$, $M_{jg}^{k}$ and $R_{jg}^{k}$ under J$_2$ and third body perturbations over 12 days a) Inclination evolution b) Eccentricity evolution. c) Difference in inclination between multibody model and rigid models d) Difference in eccentricity between multibody and rigid mode.**

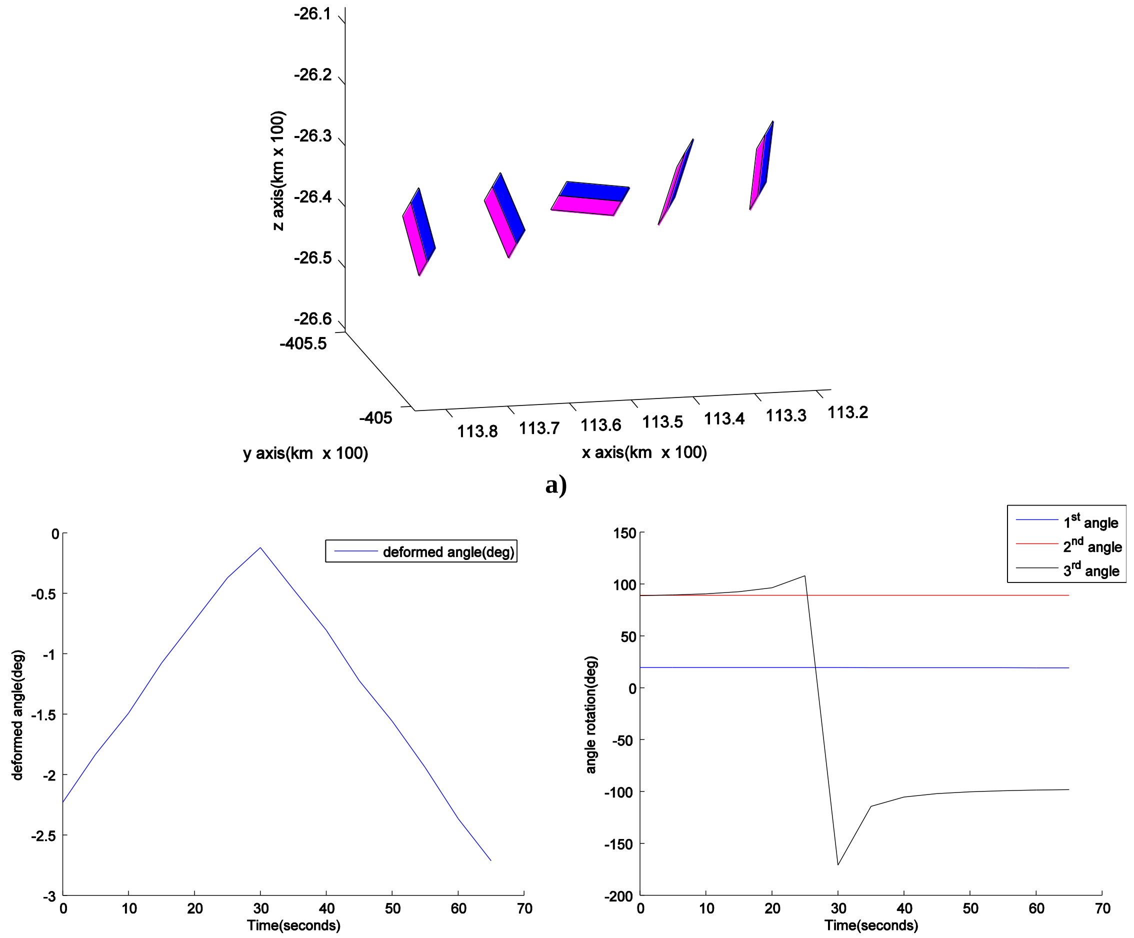

a)

b)

c)

**Figure 4.21 Show tumbling and deformation of PET® object under $J_2$ and the third body from the Sun and Moon during 1.8296-1.8305 day (65 seconds) a) time-lapse of deformation in inertial frame (1 plot /3 seconds) b) Deformed angle evolution c) Euler angle evolution.**

### 4.7.4 Dynamics under all perturbations

This section aims to investigate the orbital evolution under the effects of all perturbations for the three objects ($M^{p}_{jgs,h}$, $M^{k}_{jgs,h}$, $R^{p}_{jgs}$, $R^{k}_{jgs}$, $C^{p}_{jgs}$ and $C^{k}_{jgs}$) over a period of 12 days with the self-shadowing effect considered for the multibody models ($M^{p}_{jgs,h}$, $M^{k}_{jgs,h}$). Figure 4.22 shows the orbital dynamics of the bodies. $C^{p}_{jgs}$ presents the highest variations in both inclination and eccentricity. The maximum inclination change of $M^{p}_{jgs,h}$ can reach $\Delta i \approx 0.033$ while for $M^{k}_{jgs,h}$, this is one order of magnitude smaller at around $\Delta i \approx 0.006$. The difference is due to PET® being lighter than Kapton® and having uniform reflection properties. It is evident from these results that the variations in both inclination and eccentricity caused by SRP are dominant over those exerted by $J_2$ and the third body from the Sun and Moon. The attitude motions of $M^{p}_{jgs,h}$ and $M^{k}_{jgs,h}$ during 1.0-1.5 day are shown in Figure 4.23 and Figure 4.24 respectively and both display very fast and complex motion. It is worthy to note that the combinations of the multibody model, reflection properties and the self-shadowing effect lead to unique non-stable rotations and deformations of both PET® and Kapton®. This simulation takes 3.26 minutes/day evolution on a personal PC CPU @ 1.80 GHz with RAM 8 GB. This is around three times faster than the time required for the simulation of the Bernoulli model.

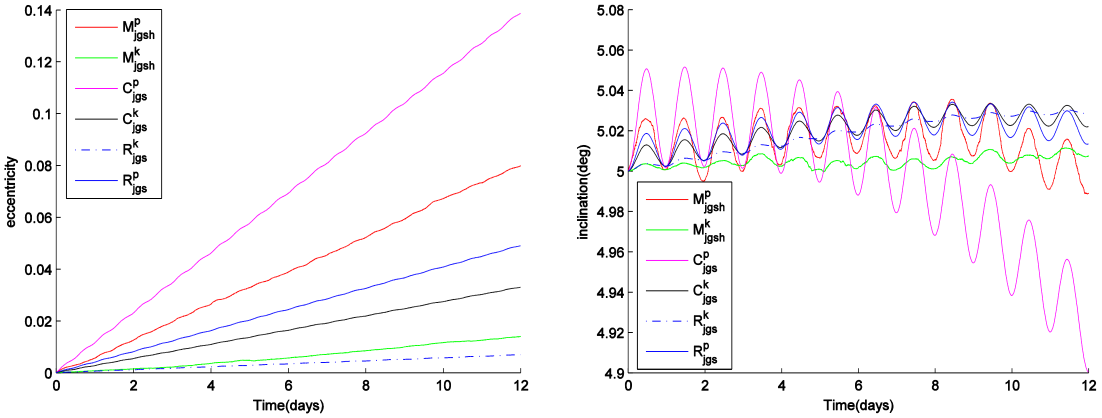

**Figure 4.22 Comparison in eccentricity and inclination evolution over 12 days of $M^{p}_{jgs,h}$, $M^{k}_{jgs,h}$, $R^{p}_{jgs}$, $R^{k}_{jgs}$, $C^{p}_{jgs}$ and $C^{k}_{jgs}$ under $J_2$, third body perturbations and solar radiation pressure.**

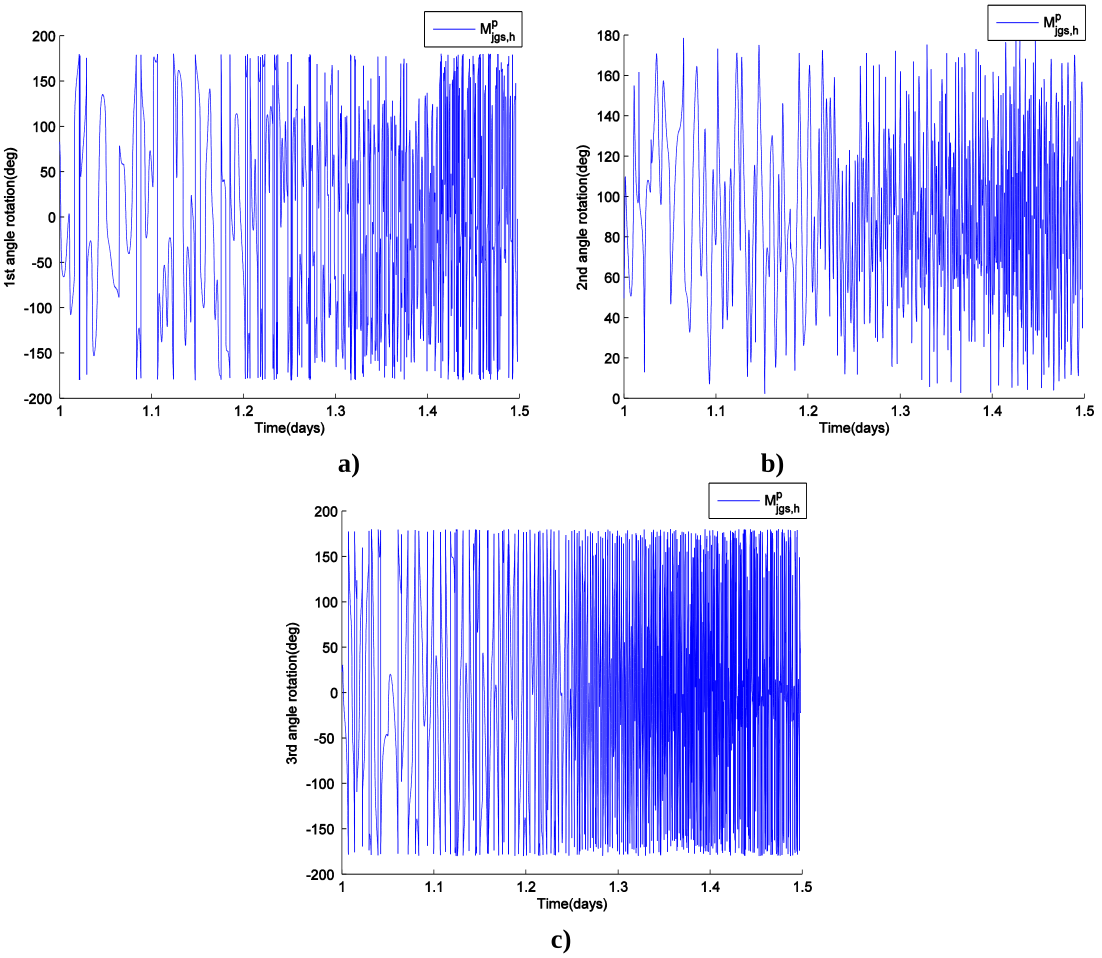

**a)** **b)**

**c)**

**Figure 4.23 Euler angle evolution of $M^{p}_{jgs,h}$ during 1.0-1.5 day under J2, third body perturbations and the direct solar radiation pressure a) the 1st Euler rotation b) the 2nd Euler rotation c) the 3rd Euler rotation.**

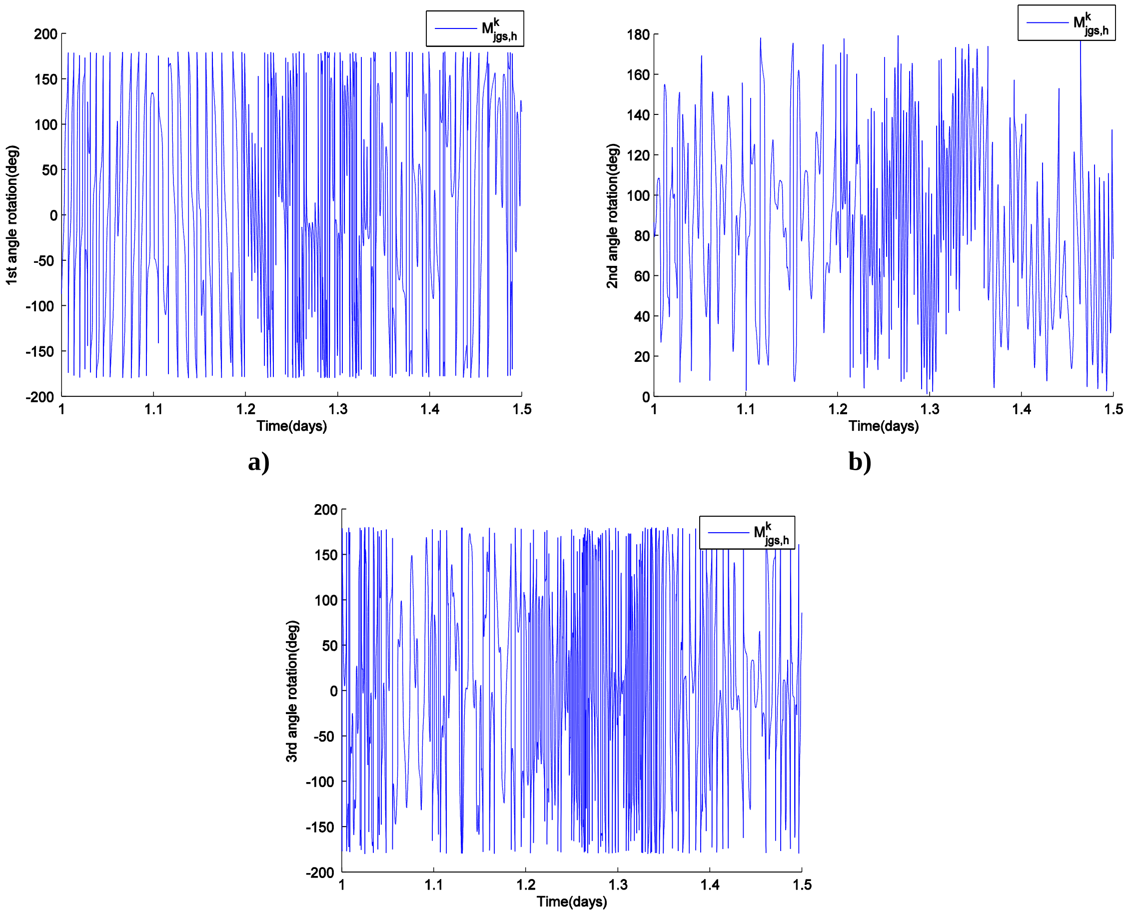

**a)** **b)**

**c)**

**Figure 4.24 Euler angle evolution of $M^k_{jgs,h}$ during 1.0-1.5 day under J2, third body perturbations and the direct solar radiation pressure a) the 1st Euler rotation b) the 2nd Euler rotation c) the 3rd Euler rotation.**

## 4.7.5 Monte Carlo simulation

In a real case scenario the attitude and shape of the debris will not be known. Performing a Monte Carlo analysis can therefore shed some light on understanding the effects that different initial conditions have on the orbital propagation of the debris. A Monte Carlo simulation of the multibody model is therefore, performed to investigate the uncertainty of the orbital evolution over a period of 100 days under different initial attitude and deformation angle of the multibody model ($M^p_{jgs,h}$) by comparing it with cannonball model ($C^p_{jgs}$) and flat rigid plate ($R^p_{jgs}$). All objects will be in the same initial orbit shown in Table 4.2 and the same starting date. In the case of the rigid models, there are 3 cannonball objects with different AMR of 50, 70 and 111.11 $m^2$/kg and flat rigid plates: $R^p_{jgs}$ with AMR of 19.56 $m^2$/kg with averaged solar radiation pressure average.

The computational cost over 100 days of Monte Carlo for the multibody model is higher due to the coupling of deformation attitude and orbital dynamic as well as the inclusion of self-shadowing effects when compared to the rigid model. The sampling technique is, therefore, important to select the suitable sampling sizes of initial rotation angles and deformed angle. From the study of Burhene and Matala by comparing different sampling methods (random sampling, stratified sampling, Latin hypercube sampling and sampling based on Sobol sequence) [56, 57], the Latin hypercube (LH) sampling shows the fastest convergence and produces reasonable results even for very small sample sizes. This technique is flexible in terms of data density and location and has good uniformity with respect to each dimension variable.

Figure 4.25 shows a mean value of uniform distribution sampling of attitude dynamics and deformation angle by varying the sample size. Due to the large the number of sampling sizes and complicated dynamics of multibody model to predict orbital motions of all 300 initial conditions, this investigation requires the expensive computations. The simulations were, therefore, performed in parallel on a Linux-based computer cluster with 50 processor cores.

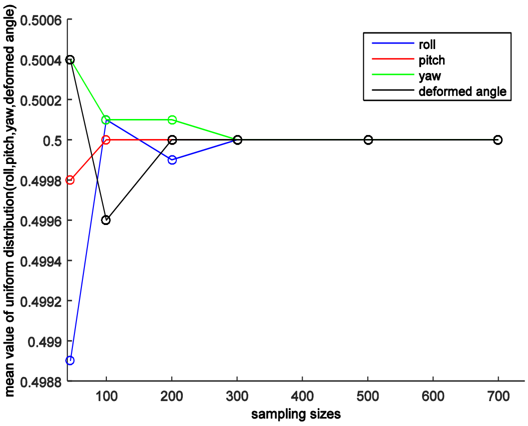

**Figure 4.25 Comparing mean values of 4 variables (yaw, pitch, roll and deformed angle) in different sampling size by using Latin hypercube method in term of uniform distribution [0,1].**

Figure 4.26 shows the final values of eccentricity, inclination and semi-major for $C^{p}_{jgs}$, $R^{p}_{jgs}$ and $M^{p}_{jgs,h}$ over 50 days. It can be noticed that $C^{p}_{jgs}$ with AMR: 111.11 (triangular) and $R^{p}_{jgs}$ (cross) shows the highest and lowest eccentricity respectively and for $C^{p}_{jgs}$ with AMR 70 m$^2$/kg (diamond), the orbital evolutions of this object is close to the debris cloud of $M^{p}_{jgs,h}$. We produce the histogram and fitted normal distribution of the orbital element data of $M^{p}_{jgs,h}$ by using statistical data binning as show in Figure 4.27, presenting that eccentricity, inclination and semi-major evolutions are in range of 0.31–0.34, 4.30–4.62

degrees and 41,611–42,629 km respectively. These results imply that the propagation of a different initial rotational motion and a unique shape provide a different orbital motion.

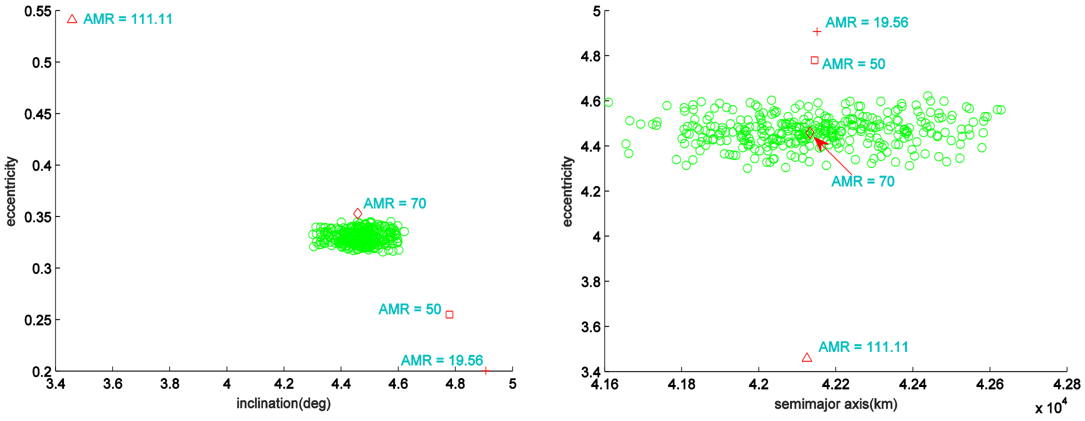

a) b)

**Figure 4.26 Comparison the orbital distribution of the Monte Carlo simulation of the multibody model (green circle) with rigid flat plate (blue circle) and cannonball objects (red symbols) over 50 days a) inclination vs eccentricity b) semi-major axis vs eccentricity.**

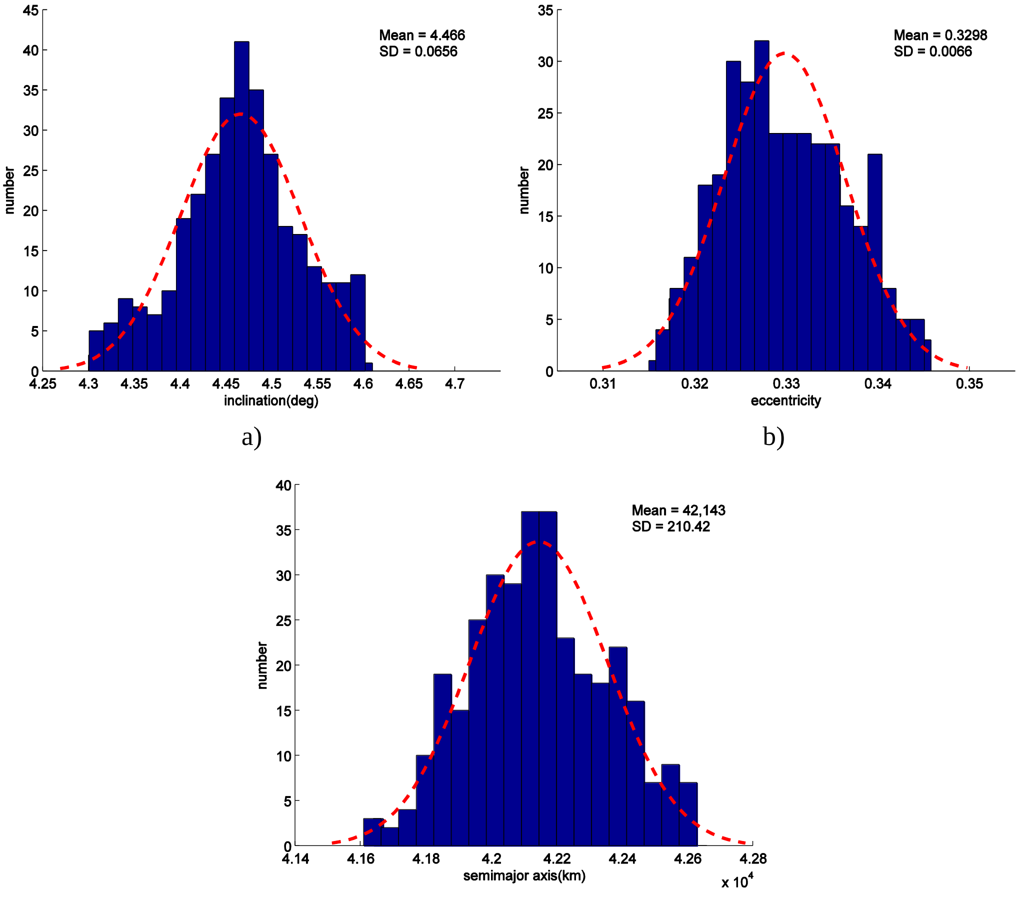

a) b)

c)

**Figure 4.27 Histogram and fitted normal distribution of orbital evolutions of $M^{p}_{jgs,h}$ over 100 days a) inclination (b) eccentricity (c) semi-major axis.**

After evaluating the orbital dynamics over 100 days in Figure 4.28, all rigid bodies ($C^{p}_{jgs}$ and $R^{p}_{jgs}$) in Figure 4.28(b) of the graph plotting semi-major vs inclination move in the

$M^{p}_{jgs,h}$ clusters between semi-major axis range of 42,139-42,211 km with inclination range of 5.45- 6.98 degrees. The histogram of multibody model cluster (Figure 4.29) displays larger clouds: inclination range of 0.52–0.62 degrees, eccentricity range of 4.72–5.59 and semi-major axis of 41,504-42,964 km that coherent with SD values increase in all orbital elements when compared to the 50th day. As the results of the Monte Carlo simulations over 100 days, it is worthwhile noting that the different initial conditions of multibody model lead to different evolution because the model is subject to changes in the effective cross-sectional area, which results in large variations in the SRP force vector. In case of the rigid object ($C^{p}_{jgs}$ and $R^{p}_{jgs}$), the secular eccentricity is proportional to AMR value but the evolutions of both inclination and semi-major axis of cannonball model display narrower variations when compared to multibody model. These results support the suggestions of real measurements as well as characterization measurements that the effectively exposed area is not stable and the objects are possible in fast attitude motion. Therefore, it can be noted that the cannonball model and flat rigid plate despite using an averaged area values do not appear to provide a good approximation to the orbital dynamics of MLI debris.

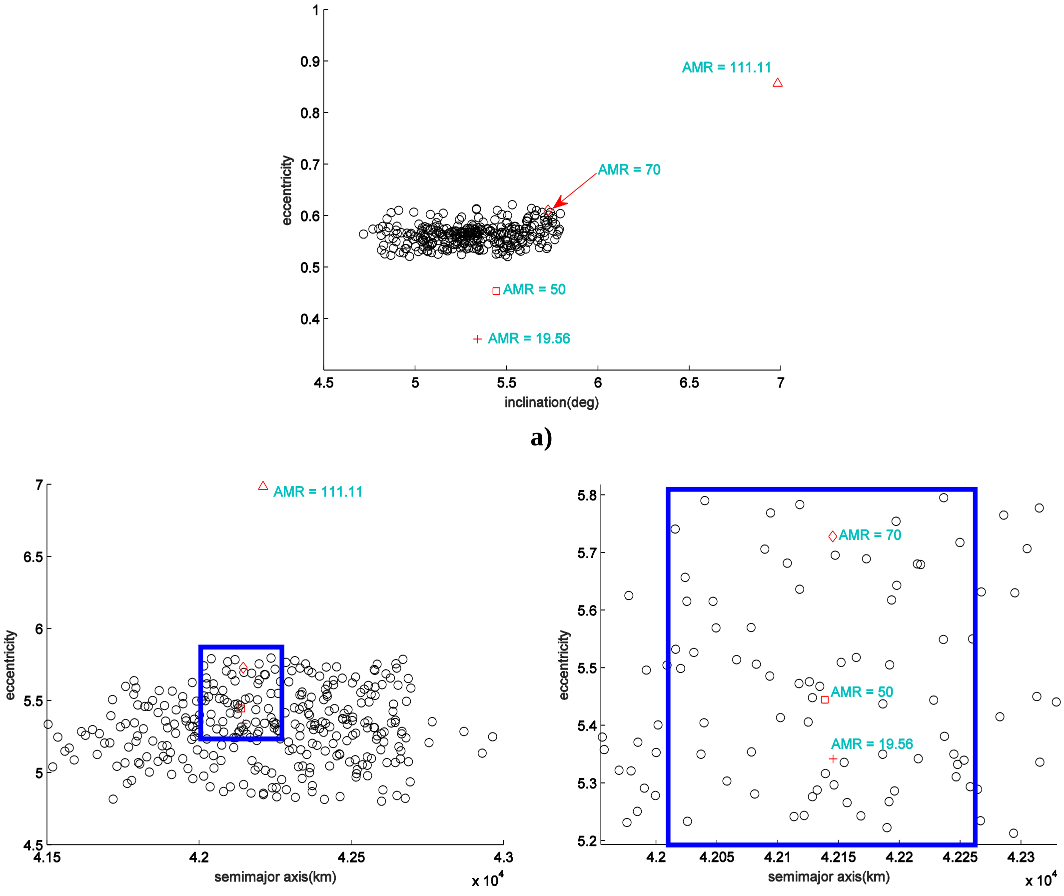

a)

b) c)

**Figure 4.28 Comparison the orbital distribution of the Monte Carlo simulation of the multibody model (black circle) with rigid flat plate (blue circle) and cannonball objects (red symbols) over 100 days a) eccentricity vs inclination b) semi-major axis vs inclination c) Magnify on the blue area of semi-major axis vs inclination.**

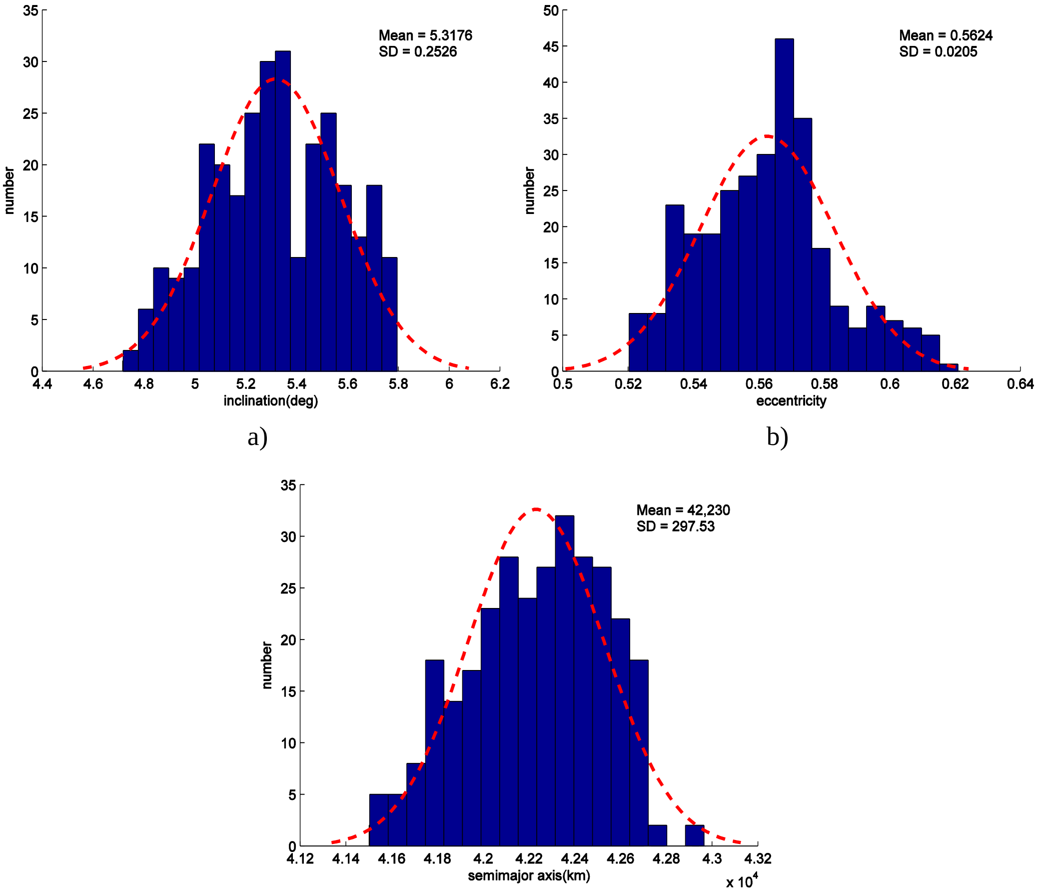

a)

b)

c)

**Figure 4.29 Histogram and fitted normal distribution of orbital evolutions of $M^{p}_{jgs,h}$ over 100 days a) inclination (b) eccentricity (c) semi-major axis**

## 4.8 Summary

A new model for high area-to-mass ratio (HAMR) objects based on multibody dynamics that is able to couple deformation, attitude and orbit dynamics in near GEO region has been presented. The specific results of the effects of various perturbations on different orbital parameters and physical properties of the body are analysed.

Compared to the orbital element evolutions of a flat rigid model, the multibody model displays larger changes in inclination and eccentricity. The fast rotation of the multibody model leads to inclination and eccentricity changes that are different from a flat rigid plate. Then, the self-shadowing effect provides different orbital and attitude dynamics, deformation and hence effective cross-section area when compared to a body without self-shadowing effects.

The $J_2$ and luni-solar perturbations can induce body rotation due to gravity torque. Larger area-to-mass ratios are also the reason for higher oscillations in both inclination and eccentricity as well as rapid irregular spin. In all simulations the results show that perturbations from solar radiation pressure also play a significant role in both the dynamical evolution and rapid complex rotation of the body.

According to the results of the Monte Carlo simulations, different initial conditions of in the attitude dynamics and shape orientation leads to substantially different orbital dynamics over a period of just 100 days. The results also appear to support the idea that rigid objects (cannonball and rigid flat plate) are not a good approximation to predict the long term orbital evolutions of HAMR debris [14, 29, 30].

The next chapter is will describe set experimental setup, through the use of a vacuum chamber that replicates the space environment to determine the characteristics of the material (damping ratio) and natural frequency of real multilayer insulation including the validation the multibody model through experimental results.

# 5 Experimental validation

## 5.1 Introduction

This chapter presents a methodology to determine the dynamic properties of thin membranes with the aim to validate the deformation of the computational flexible model. The experiments are performed in a high-vacuum chamber in order to replicate as much as possible, the space environment. The first experiment, a free motion test, is used to determine the damping characteristics and natural frequency of the thin membrane with the free vibration decay technique. The motion is tracked through an optical camera, and a Kalman filter is implemented in the tracking algorithm. Then, the effect of solar radiation pressure of the thin membrane is investigated in the second experiment by mean of a high power spotlight which is used to illuminate the sample and any displacement of the thin membrane is measured by means of a high-resolution laser sensor. Analytic methods of both experimental setups are used for the validation of the multibody model by comparing with the experimental results of amplitude decay, natural frequencies and forced displacement.

## 5.2 Experimental setup

The two experimental setups (free motion and forced motion experiments) of this chapter are described in this section. Three MLI samples are used in both experiments: PET 1 mil, Kapton 1 mil and PET 5 mils. All samples have the same width (5 cm) and length (20 cm) and their physical characteristics and properties are shown in Table 5.1.

**Table 5.1 Properties of PET and Kapton [18, 58].**

| Material type | Thickness mil (µm) | Mass (mg) | Density (kg/ m$^3$) | Young’s Modulus (N/m$^2$) | *Cs, Cd, Ca* |
|---|---|---|---|---|---|
| PET 1mil | 1 (25.4) | 0.3530 | 1,390 | $8.81 \times 10^9$ | 0.60 0.26 0.14 |
| PET 5 mils | 5 (127) | 1.7653 | 1,390 | $8.81 \times 10^9$ | 0.60 0.26 0.14 |
| Kapton 1 mil | 1 (25.4) | 0.3606 | 1,420 | $2.50 \times 10^9$ | 0.60 0.26 0.14 |

### 5.2.1 Free motion experiment setup

The setup for the free motion test is shown in Figure 5.1. This test aims to find the damping characteristics of each MLI sample. The sample is attached by means of a stand and held in place by an electromagnetic latch. The camera (Canon IXUS 110 IS, 30fps) is set in front of the mirror window. Before starting the experiment, we drain the air inside of the vacuum chamber (size : 30x30x28.7 cm$^3$) down the lowest possible level of 10$^{-4}$ mbar (high vacuum level). The power to the electromagnetic latch is then turned off and this releases the sample, which swings freely and this motion is recorded by the camera. The data is used for the object tracking process to allow measurement of the amplitude decay and application of Fast Fourier Transform (FFT) process to define the natural frequencies of the MLI samples.

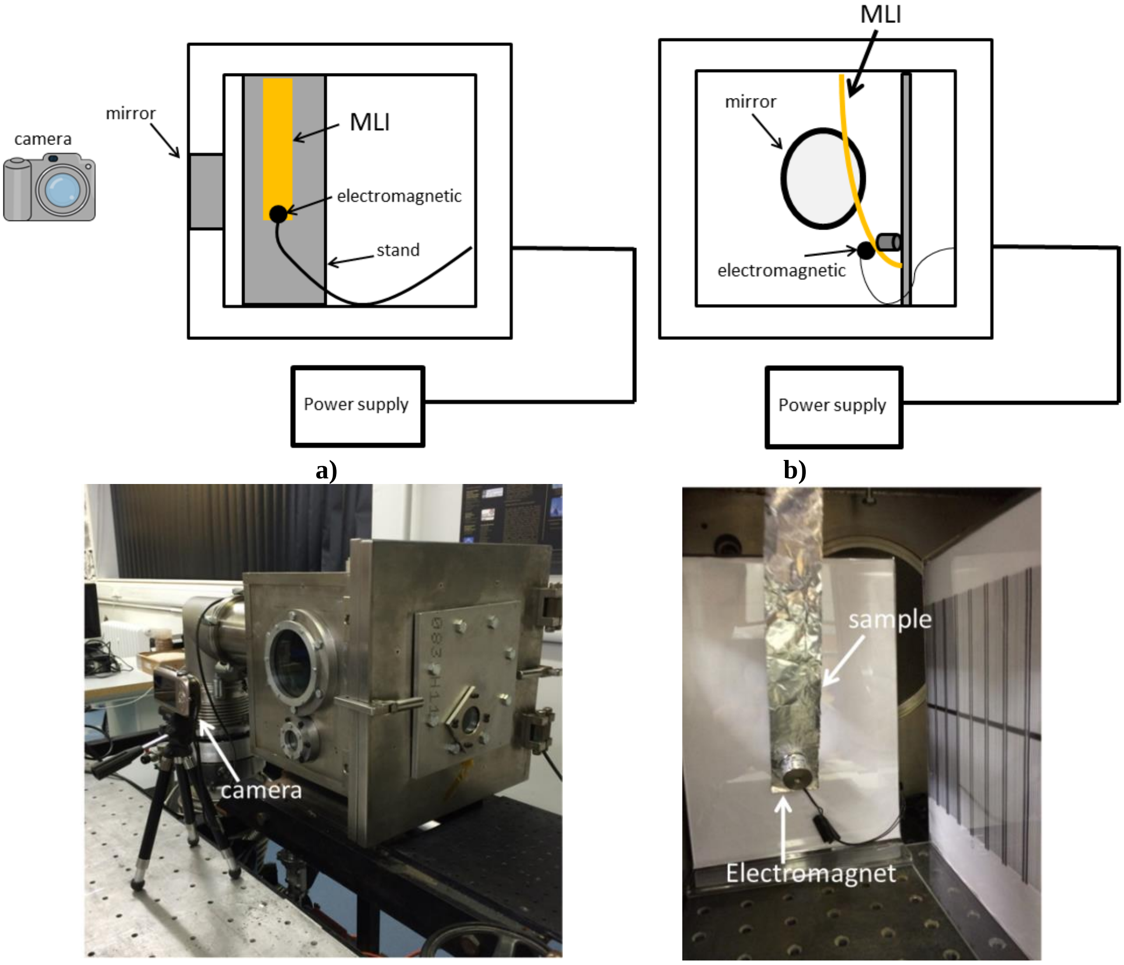

a) b)

c) d)

**Figure 5.1 Schematic drawing and experimental setup of the free motion setup a) side view b) back view c) outside vacuum d) inside vacuum.**

#### 5.2.1.1 Object tracking

In order to measure the motion of the MLI sample inside the vacuum chamber during the experiment, object motion tracking, through a recorded video, is used. This is achieved by measurement of the movement of a red point, representing the lump mass of the multibody model. There are six major steps, illustrated in Figure 5.2 to this proc. The motion of the sample is converted to be an image sequence (Figure 5.3(a)). The three red pixels are then extracted and separated from blue and green pixels (Figure 5.3(b)). In the object recognition and representation step (Figure 5.3(c)), the extracted red pixels are converted to white in a binary image. This will then allow to process a representation of each recognized tracked object. The last step, Kalman filter tracking, uses a Kalman algorithm[59, 60] to estimate an observable state, which is updated in each time step with a linear state update, and plots the tracking blue rectangle around the object's movement at each time step (Figure 5.3(d)).

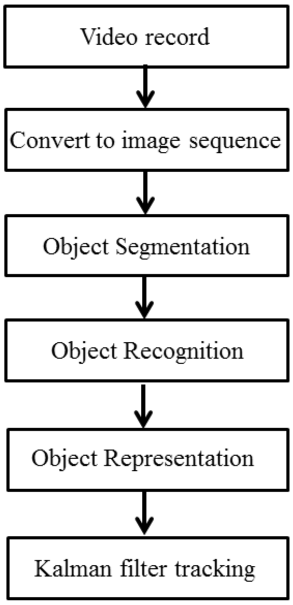

**Figure 5.2 Object tracking process.**

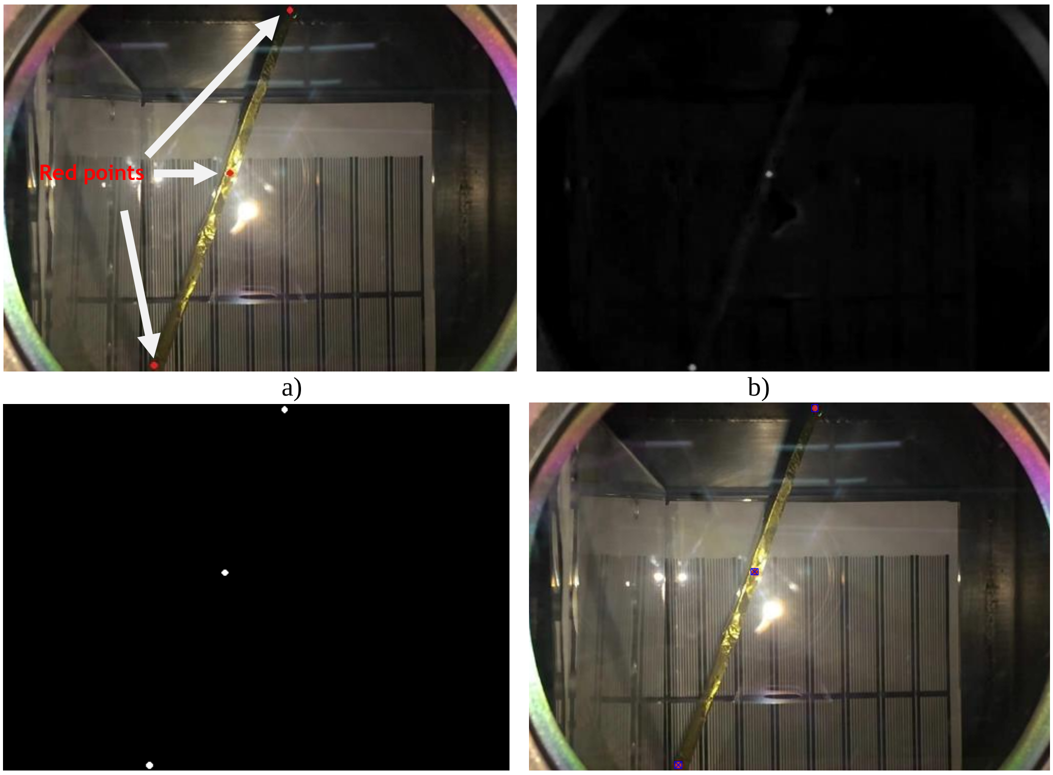

a) b)

c) d)

**Figure 5.3 Object tracking simulation a) an extracted image from a video record b) Extracting the red pixels from a picture c) Converting a grayscale image into a binary image d) Blue mark on the red three points on an image.**

### 5.2.1.2 Kalman filter

The Kalman filter is an algorithm that uses a series of measurements observed over time to predict a future state and uses available measurements to correct this prediction. For visual object tracking, Kalman filtering is usually achieved by representing the uncertainty via a Gaussian function, to balance the effects of tracking results from observation and prediction. In this experiment, the state measurements of the free motion experiment are represented by the positions of three red points. The Kalman filter algorithm has, two steps: prediction and update.

#### 5.2.1.2.1 Prediction

The prediction step makes uses of the state estimate from the previous time step to produce an estimate of the state at the current time step.

1) State prediction, $\bar{X}_{i+1}$: a Kalman filter makes a prediction of the state at $i+1$ defined by:

$$\overline{X}_{i+1} = \Phi_s \hat{X}_i \tag{5.1}$$

Where $\Phi_s$ is the state transition matrix and $\hat{X}_i$ is the current state vector.

In the model of object tracking on 2D camera images [61], the state vector consists of a two-dimensional position, velocity and acceleration. By considering a constant acceleration, the state transition matrix can be determined from the basic kinematic equation as follow:

$$\vec{x}_{t+1} = \vec{x}_t + \vec{x}_t \Delta t + \frac{1}{2} a_t \Delta t^2 \tag{5.2}$$

$$\vec{v}_{t+1} = \vec{v}_t + a_t \Delta t \tag{5.3}$$

$$\vec{a}_{t+1} = a_t \tag{5.4}$$

Where $\vec{x}_t$ and $\vec{x}_{t+1}$ is vector $\begin{bmatrix} x & y & \dot{x} & \dot{y} & \ddot{x} & \ddot{y} \end{bmatrix}$ in time of $t$ and $t+1$ respectively. $x$ and $y$ are the coordinates of the red point representing a lump mass and $\dot{x}$ and $\dot{y}$ are its velocity and $\Delta t$ is the discrete time of sequence image. Therefore, $\Phi_s$ matrix is expressed as:

$$\Phi_s = \begin{bmatrix} 1 & 0 & \Delta t & 0 & 0.5\Delta t & 0 \\ 0 & 1 & 0 & \Delta t & 0 & 0.5\Delta t \\ 0 & 0 & 1 & 0 & 1 & 0 \\ 0 & 0 & 0 & 1 & 0 & 1 \\ 0 & 0 & 0 & 0 & 1 & 0 \\ 0 & 0 & 0 & 0 & 0 & 1 \end{bmatrix} \tag{5.5}$$

2) State covariance prediction: a Kalman filter estimates the error covariance $\overline{P}_{i+1}$ forward as:

$$\overline{P}_{i+1} = \Phi \hat{P}_i \Phi^T + Q \tag{5.6}$$

Where $Q$ is the process noise covariance and $\hat{P}_i$ is the error covariance matrix.

##### 5.2.1.2.2 Measurement update

After predicting the state and its error covariance at time $i+1$ the process then continues as:

1) Kalman Gain: the Kalman filter computes a Kalman gain $K_{i+1}$ used to correct the state estimates $\bar{X}_{i+1}$:

$$K_{i+1} = \bar{P}_{i+1} H_{i+1}^T (H_{i+1} \bar{P}_{i+1} H_{i+1}^T + R)^{-1} \tag{5.7}$$

Where $H_{i+1}$ is a matrix that converts the state space into a measurement space at $i+1$ and $R$ is a measurement noise covariance.

2) Update Estimate with measurement $\hat{X}_{i+1}$: the Kalman gain and measurement from time step, are then used to update the state estimate as;.

$$\hat{X}_{i+1} = \bar{X}_{i+1} + K_{i+1}[Z_{i+1} - H_{i+1}\bar{X}_{i+1}] \tag{5.8}$$

Where $Z_{i+1}$ is the measurement vector.

3) Update error Covariance estimate ($\hat{P}_{i+1}$): the final step of the Kalman filter's iteration is the update of the error covariance $\bar{P}_{i+1}$ to $\hat{P}_{i+1}$.

$$\hat{P}_{i+1} = [I - K_{i+1}H_{i+1}]\bar{P}_{i+1} \tag{5.9}$$

Where $I$ is the identity matrix.

#### 5.2.1.3 Multibody model

As introduced in Chapter 4, the multibody, flexible model is represented as three lump masses connected with rigid rods ($L = L_1 = L_2$ = 0.10 m). The 2nd lump mass includes a rotational spring and damper. The multibody model based on both free motion and forced motion experiments in Figure 5.4 is fixed at one end to the top of the vacuum chamber while the other end is left to swing freely under the effects of gravity and other external forces. This 3D membrane is modelled as two dimensional, considering only the plane of the main oscillation. This plane is perpendicular to the plane of the undeformed membrane itself. The first lump mass is defined as origin of the frame of reference at the pivot point.

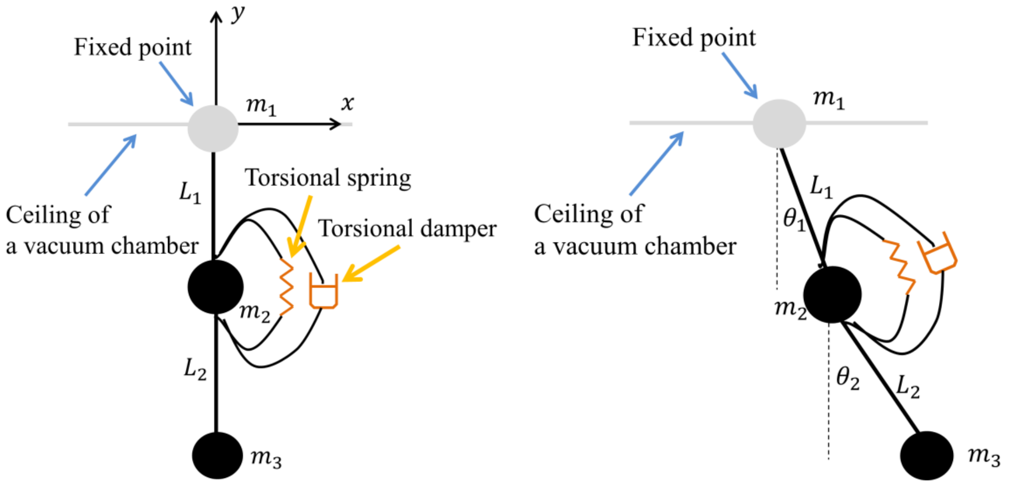

a) b)

**Figure 5.4 Multibody model of the three lump masses a) initial position b) Displacement after applying an external force on the lump mass.**

In order to develop the system dynamics, we first define the positions of each lump mass ($x_1, y_1, x_2, y_2, x_3, y_3$) in terms of the deformation angles ($\theta_1$ , $\theta_2$) as:

$$x_1 = 0 \tag{5.10}$$

$$y_1 = 0 \tag{5.11}$$

$$x_2 = L_1 \sin\theta_1 \tag{5.12}$$

$$y_2 = -L_1 \cos\theta_1 \tag{5.13}$$

$$x_3 = x_2 + L_2 \sin\theta_2 \tag{5.14}$$

$$y_3 = y_2 - L_2 \cos\theta_2 \tag{5.15}$$

The free-body diagram in Figure 5.5 shows the net force acting on each lump mass. The net forces on the 1$^{st}$ mass are zero due to the pivot point.

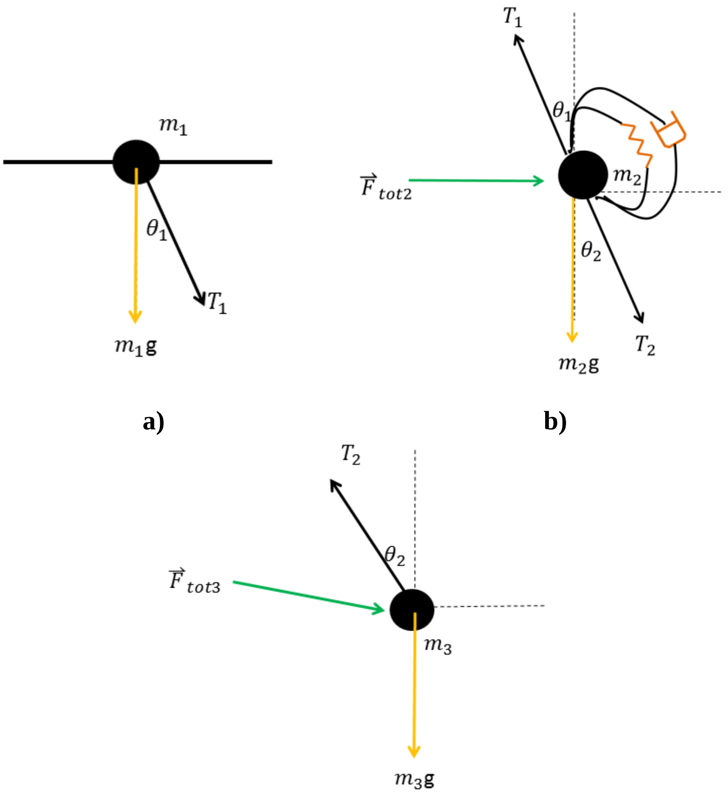

**a)** **b)**

**c)**

**Figure 5.5 Free body diagram of each lump mass a) 1st lump mass (fixed position)b) 2nd lump mass c) 3rd lump mass.**

The equation of motion of the 2nd lump mass is represented in the horizontal and vertical forces ( $F_{x\_tot,2}$ and $F_{y\_tot,2}$ ) by using the second law of Newton:

$$m_2\ddot{x}_2 = -T_1 s_1 + T_2 s_2 + F_{x\_tot,2} \tag{5.16}$$

$$m_2\ddot{y}_2 = T_1 c_1 - T_2 c_2 - m_2 g + F_{y\_tot,2} \tag{5.17}$$

Where $m_2$ is the second lump mass $F_{x\_tot,2}$ and $F_{y\_tot,2}$ are total force vectors acting on the 2th lump mass in $x$ and $y$ direction respectively ( $\vec{F}_{tot,2} = \vec{F}_{\text{int},2} + \vec{F}_{ext,2} + \vec{F}_{D,2}$ ), $\vec{F}_{\text{int},2}$ is the internal force vector from the summation of rotational damper and spring force vectors ( $\vec{F}_{\text{int},2} = \vec{F}_{spring} + \vec{F}_{damper}$ ), $\vec{F}_{ext,2}$ is the external force vector, $\vec{F}_{D,2}$ is the air friction, $\vec{T}_j$ is the tension force vector generated by the $j^{th}$ rods ( $j =$ 1 and 2), $\ddot{x}_2$ is acceleration in x direction of the 2th lump mass, $s_1 = \sin\theta_1$, $c_1 = \cos\theta_1$, $\ddot{y}_2$ is acceleration y direction the 2th lump mass and $s_2 = \sin\theta_2, c_2 = \cos\theta_2$. The rotational spring and damper forces are expressed as:

$$F_{spring} = K_{eq}(\theta_2 - \theta_1)/L_i \tag{5.18}$$

$$F_{damper} = C_{eq}(\dot{\theta}_2 - \dot{\theta}_1) / L_i \tag{5.19}$$

Where $\dot{\theta}_1$ and $\dot{\theta}_2$ are angular velocities of $L_1$ and $L_2$ respectively, $K_{eq}$ is the equivalent stiffness coefficient and $C_{eq}$ is the equivalent damping coefficient. The general equation of the air friction [62] is expressed as:

$$\vec{F}_D = -\frac{1}{2}\rho \vec{V}_i^{\,2} A C_D \tag{5.20}$$

Where $\rho$ is the air density, $A$ is the area of the object, $\vec{V}_i$ is the velocity of the $i^{\text{th}}$ lump mass and $C_D$ is the drag coefficient ($C_D$ of flat plate = 1.9). The equation of motion of the 3rd lump mass is:

$$m_3\ddot{x}_3 = -T_2\,\mathrm{s}_2 + F_{x\_tot,3} \tag{5.21}$$

$$m_3\ddot{y}_3 = T_2\,\mathrm{c}_2 - m_3 g - F_{y\_tot,3} \tag{5.22}$$

Then, we substitute Eq.(5.21) and (5.22) into Eq.(5.16) and (5.17):

$$m_2\ddot{x}_2 = -T_1 s_1 - m_3\ddot{x}_3 + F_{x\_tot,3} + F_{x\_tot,2} \tag{5.23}$$

$$m_2\ddot{y}_2 = T_1\,\mathrm{c}_1 - m_3\ddot{y}_3 - m_3 g - m_2 g + F_{y\_tot,2} + F_{y\_tot,3} \tag{5.24}$$

We multiply $\cos\theta_1$ in Eq.(5.23) and $\sin\theta_1$ in Eq.(5.24) and rearrange the LHS in term of $T_1 s_1 c_1$:

$$T_1 s_1 c_1 = -c_1 m_2\ddot{x}_2 - m_3\ddot{x}_3 c_1 + c_1(F_{x\_tot,2} + F_{x\_tot,3}) \tag{5.25}$$

$$T_1 s_1\,\mathrm{c}_1 = s_1 m_2\ddot{y}_2 + s_1 m_3\ddot{y}_3 - s_1(-m_3 g - m_2 g + F_{y\_tot,2} + F_{y\_tot,3}) \tag{5.26}$$

Then, substituting Eq (5.25) into Eq (5.26):

$$\begin{aligned} c_1(F_{x\_tot,2} + F_{x\_tot,3}) - c_1 m_2\ddot{x}_2 - m_3\ddot{x}_3 c_1 &= s_1 m_2\ddot{y}_2 + s_1 m_3\ddot{y}_3 \\ &\quad - s_1(-m_3 g - m_2 g + F_{y\_tot,2} + F_{y\_tot,3}) \end{aligned} \tag{5.27}$$

In order to find expressions for the angular acceleration of $\ddot{\theta}_1$ and $\ddot{\theta}_2$ in terms of $\theta_1$, $\dot{\theta}_1$, $\theta_2$ and $\dot{\theta}_2$, the second order derivatives from Eq.(5.12) to Eq.(5.15) are the acceleration as:

$$\ddot{x}_2 = -\dot{\theta}_1^{\,2} L_1 \sin\theta_1 + \ddot{\theta}_1 L_1 \cos\theta_1 \tag{5.28}$$

$$\ddot{y}_2 = \dot{\theta}_1^2 L_1 \cos\theta_1 + \ddot{\theta}_1 L_1 \sin\theta_1 \tag{5.29}$$

$$\ddot{x}_3 = \ddot{x}_2 - \dot{\theta}_2{}^2 L_2 \sin\theta_2 + \ddot{\theta}_2 L_2 \cos\theta_2 \tag{5.30}$$

$$\ddot{y}_3 = \ddot{y}_2 + \dot{\theta}_2{}^2 L_2 \cos\theta_2 + \ddot{\theta}_2 L_2 \sin\theta_2 \tag{5.31}$$

The next step is a substitution of the acceleration from Eq.(5.28) to Eq.(5.31) in Eq.(5.27):

$$\begin{aligned} &\ddot{\theta}_1 L_1 (m_2 + m_3) + \ddot{\theta}_2 L_2 m_3 \cos(\theta_2 - \theta_1) - \dot{\theta}_2^2 L_2 m_3 \sin(\theta_2 - \theta_1) \\ &\qquad = c_1 (F_{x\_tot,2} + F_{x\_tot,3}) + s_1(-m_3 g - m_2 g + F_{y\_tot,2} + F_{y\_tot,3}) \end{aligned} \tag{5.32}$$

In the same way for the 3rd lump mass, we multiply Eq.(5.21) by $\cos\theta_2$ and Eq.(5.22) by $\sin\theta_2$ and substitute the acceleration from Eq.(5.28) to Eq.(5.31). Finally, the equation for the angular acceleration of the third lump mass will be expressed as:

$$\ddot{\theta}_1 L_1 m_3 \cos(\theta_2 - \theta_1) + \ddot{\theta}_2 L_2 m_3 + \dot{\theta}_2^2 L_1 m_3 \sin(\theta_2 - \theta_1) = s_2 (m_3 g + F_{y\_tot,3}) - c_2 F_{x\_tot,3} \tag{5.33}$$

Eq.(5.32) and Eq.(5.33) can be written in matrix form:

$$\begin{bmatrix} C_1 & C_2 \\ C_3 & C_4 \end{bmatrix} \begin{bmatrix} \ddot{\theta}_1 \\ \ddot{\theta}_2 \end{bmatrix} = \begin{bmatrix} A_1 \\ A_2 \end{bmatrix} \tag{5.34}$$

Where:

$$\begin{aligned} C_1 &= (m_2 + m_3) L_1 \\ C_2 &= m_3 L_2 \cos(\theta_2 - \theta_1) \\ C_3 &= m_3 L_2 \cos(\theta_2 - \theta_1) \\ C_4 &= m_3 L_2 \\ A_1 &= \dot{\theta}_2^2 L_2 m_3 \sin(\theta_2 - \theta_1) + c_1 (F_{x\_tot,2} + F_{x\_tot,3}) + s_1 (F_{y\_tot,2} + F_{y\_tot,3} - (m_2 + m_3) g) \\ A_2 &= -\dot{\theta}_2^2 L_1 m_3 \sin(\theta_2 - \theta_1) + s_2 (m_3 g + F_{x\_tot,3}) - c_2 F_{x\_tot,3} \end{aligned}$$

By multiplying the left hand side of Eq.(5.34) by the inverse of the C matrix. We can define the angular acceleration vector as:

$$\begin{bmatrix} \ddot{\theta}_1 \\ \ddot{\theta}_2 \end{bmatrix} = \begin{bmatrix} C_1 & C_2 \\ C_3 & C_4 \end{bmatrix}^{-1} \begin{bmatrix} A_1 \\ A_2 \end{bmatrix} \tag{5.35}$$

#### 5.2.1.3.1 Numerical integration

The numerical integrator used to solve the dynamics of the multibody model equations is ODE45 (MATLAB®). It requires to convert the 2nd order equations into the 1st order equations. Then, the new system is written as:

$$\begin{aligned}\dot{\theta}_1 &= \omega_1 \\ \dot{\theta}_2 &= \omega_2 \\ \dot{\omega}_1 &= \ddot{\theta}_1 \\ \dot{\omega}_2 &= \ddot{\theta}_2\end{aligned} \tag{5.36}$$

All simulations in this chapter are performed on a PC with CPU @ 1.80 GHz and 8GB RAM.

### 5.2.1.4 Underdamped free vibration

The free motion of membrane is slowly damped due to friction present in the system at the hinge and residual atmosphere in the vacuum chamber. The MLI membrane is modelled as a double pendulum as shown in Figure 5.4. The amplitude of the oscillation decreases as shown in Figure 5.6.

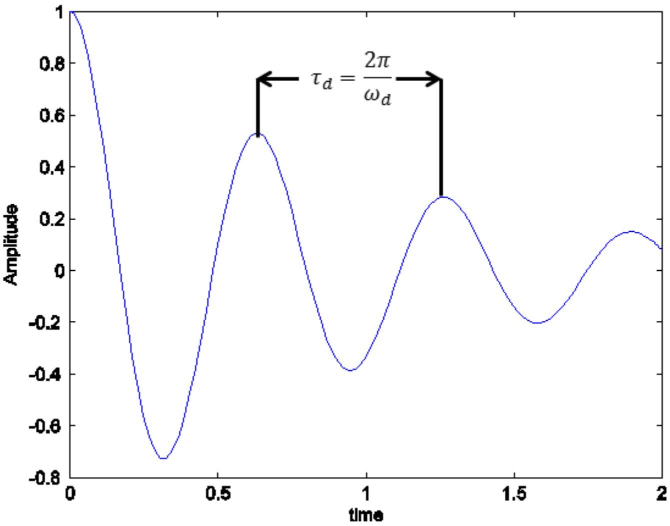

**Figure 5.6 Transient response of a decaying time-history.**

The damped vibration period ( $\tau_d$ ) in Figure 5.6 is defined as:

$$\tau_d = \frac{2\pi}{\omega_d} \tag{5.37}$$

Where $\omega_d$ is the damped natural frequency: $\omega_d = \sqrt{1-\xi^2}\,\omega_n$ and $\omega_n$ is the natural frequency of the system.

The amplitude response in the time domain can be transformed in frequency domain (Figure 5.7) by using FFT in order to estimate the damping ratio ($\xi$) of a sample.

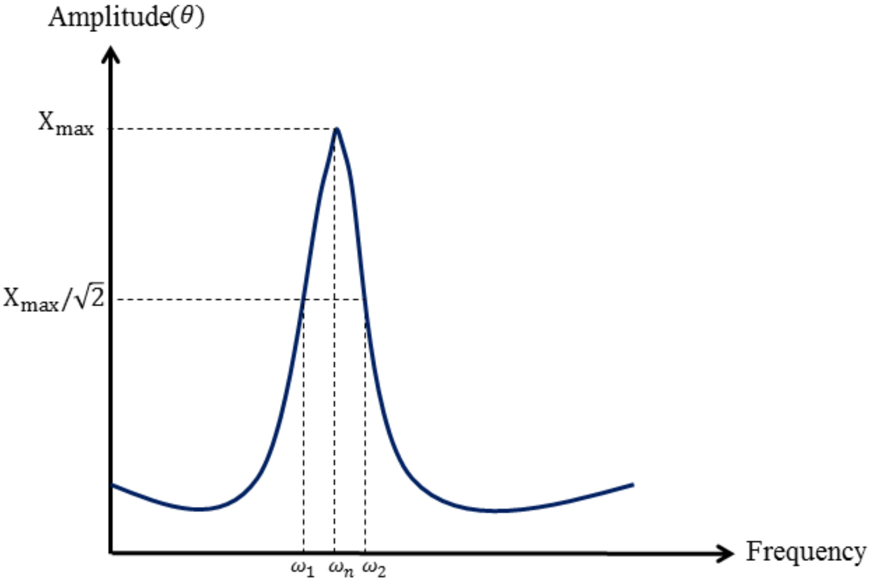

**Figure 5.7 Frequency response.**

The half-power bandwidth from the frequency response is a very useful tool for computing the damping ratios for multi freedom systems as:

$$\xi = \frac{(\omega_2 - \omega_1)}{2\omega_n} \tag{5.38}$$

From the amplitude decay and frequency response in Figure 5.6 and Figure 5.7, we can find an equivalent stiffness constant ($K_{eq}$), and equivalent damping coefficient ($C_{eq}$). They are defined as:

$$K_{eq} = \omega_n^2 M \tag{5.39}$$

and

$$C_{eq} = 2M\omega_n\xi \tag{5.40}$$

Where $M$ is the total mass of a membrane.

We can now measure the damping ratio of the material by observing the amplitude decay of the displacement and computing the natural frequency from the frequency response. Based on an unforced damped two-degree-of-freedom mass-spring-damper system, the differential equation is written as following:

$$[M]\ddot{\vec{\theta}}+[C]\dot{\vec{\theta}}+[K]\vec{\theta}=0 \tag{5.41}$$

Where $[M]$ is mass matrix, $[C]$ is the damping coefficient matrix, $[K]$ is the stiffness matrix, $\ddot{\vec{\theta}}$ is angular acceleration vector, $\dot{\vec{\theta}}$ is angular velocity vector and $\vec{\theta}$ is angular displacement vector.

### 5.2.1.4.1.1 Normal modes

In order to analyse the normal modes of oscillation of the multibody model, we reduce Eq.(5.41) to a standard eigenvalue form by removing the damping matrix. The new equation can be written as:

$$[M]\ddot{\vec{\theta}}+[K]\vec{\theta}=0 \tag{5.42}$$

And the general solutions have the form: $\theta_{1,2}(t)=A_{1,2}e^{j\omega t}$. Therefore, we can find the normal modes as:

$$\det([K]-\omega^2[M])=0 \tag{5.43}$$

The natural frequencies [63], which are the eigenvalues ($\omega^2$) of the multibody model, are determined by solving Eq.(5.43) as the solution of the quadratic equation:

$$\omega_{\pm}^2=\frac{k_1k_4+k_2k_5\pm\sqrt{(k_1k_4-k_2k_5)^2+2k_1k_5k_6^2}}{2\left(k_2k_4-k_6^2\right)} \tag{5.44}$$

Where:

$$k_1 = g(m_{rod,2}L_1 + m_{rod,1}L_1 / 2)$$
$$k_2 = I_1 + m_{rod,1}L_1^2 + m_{rod,1}(L_1 / 2)^2$$
$$k_4 = m_{rod,2}(L_1 / 2_1)^2 + I_2$$
$$k_5 = -m_{rod,2}g(L_1 / 2)$$
$$k_6 = -L_1 m_{rod,2}(L_1 / 2)$$

$I_1$ and $I_2$ are the moments of inertia of rigid rod

From Eq.(5.44), we can find the normal modes of the oscillation. The ratios of the amplitude $A_1$ and $A_2$ of two coordinates are expressed as:

$$(\frac{A_1}{A_2})_\pm = \frac{-k_5 k_6}{\omega_\pm^2\left(k_2 k_4 - k_6^2\right) - k_1 k_4} \qquad (5.45)$$

The 1st mode ($(A_1 / A_2)_+ > 0$) represents both rigid rods oscillating in the same direction (in-phase in Figure 5.8(a)). The 2nd mode ($(A_1 / A_2)_- < 0$) implies that the rigid rods move in opposite directions (out of phase in Figure 5.8(b)). The analytic method to determine natural frequency called "*normal mode*" will be compared with modal analysis performed by using ANSYS® and the experimental results obtained during free motion experiment.

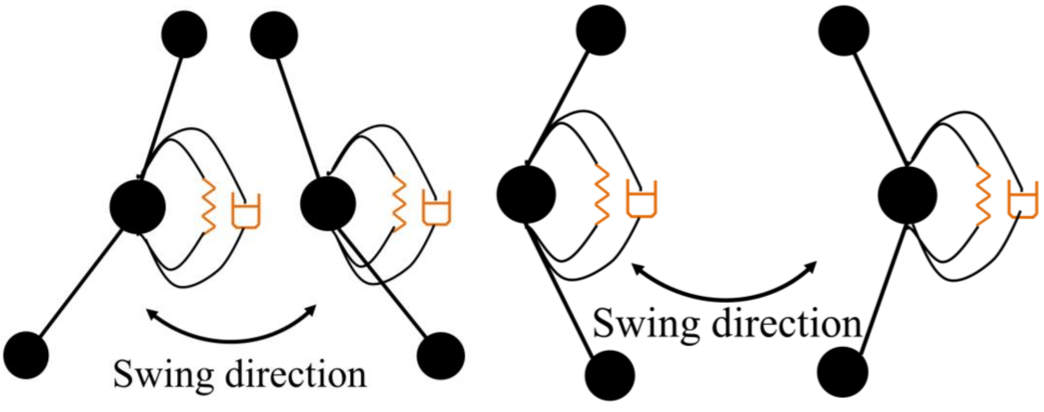

**a)** **b)**

**Figure 5.8 Two normal modes of multibody model a) 1st mode b) 2nd mode.**

### 5.2.2 Forced motion experimental setup

For the forced motion set up illustrated in Figure 5.9, we use a high power spotlight beamed onto the sample. A dimmer allows to vary the spotlight power in order to study the relationship between light intensity and sample displacement. A high resolution laser measurement system optoNCDT 1700-2LL [64], (resolution: 0.1 μm and measuring range 2 mm) is used to measure the displacement at the bottom of sample (the 3rd lump mass) as shown in Figure 5.9(c). The RS422 converter [64], which converts serial data from the sensor to a USB port, is installed to interface the sensor with a laptop. The experiment has been repeated five times on each sample and the average of the five measurements are used here to critically evaluate the results. In this experiment, the heat of radiation pressure from spotlight is able to generate air flow inside because air flows from the colder to the hotter (thermal transpiration) leading to oscillation of measurement data. We can measure this effect by using Crookes radiometer known as a light mill that was developed to measure the intensity of radiant energy or thermal effect. Basically, the air pressure inside vacuum chamber needs to strike a balance between 1 Pa and $10^{-3}$ Pa. A strong vacuum inside the bulb does not permit motion because there are not enough air molecules to cause the air currents that propel the vanes and transfer heat to the outside before both sides of each vane reach thermal equilibrium by heat conduction through the vane material. For this experiment, we however can ignore this effect because a vacuum chamber is very high level to bring a pressure down into low level air molecules and the measurement data during experiment did not show the oscillation.

In addition, the experimental results will be compared with the numerical results obtained from the analytic solution of both multibody dynamics and FEM simulations (through commercial package ANSYS®).

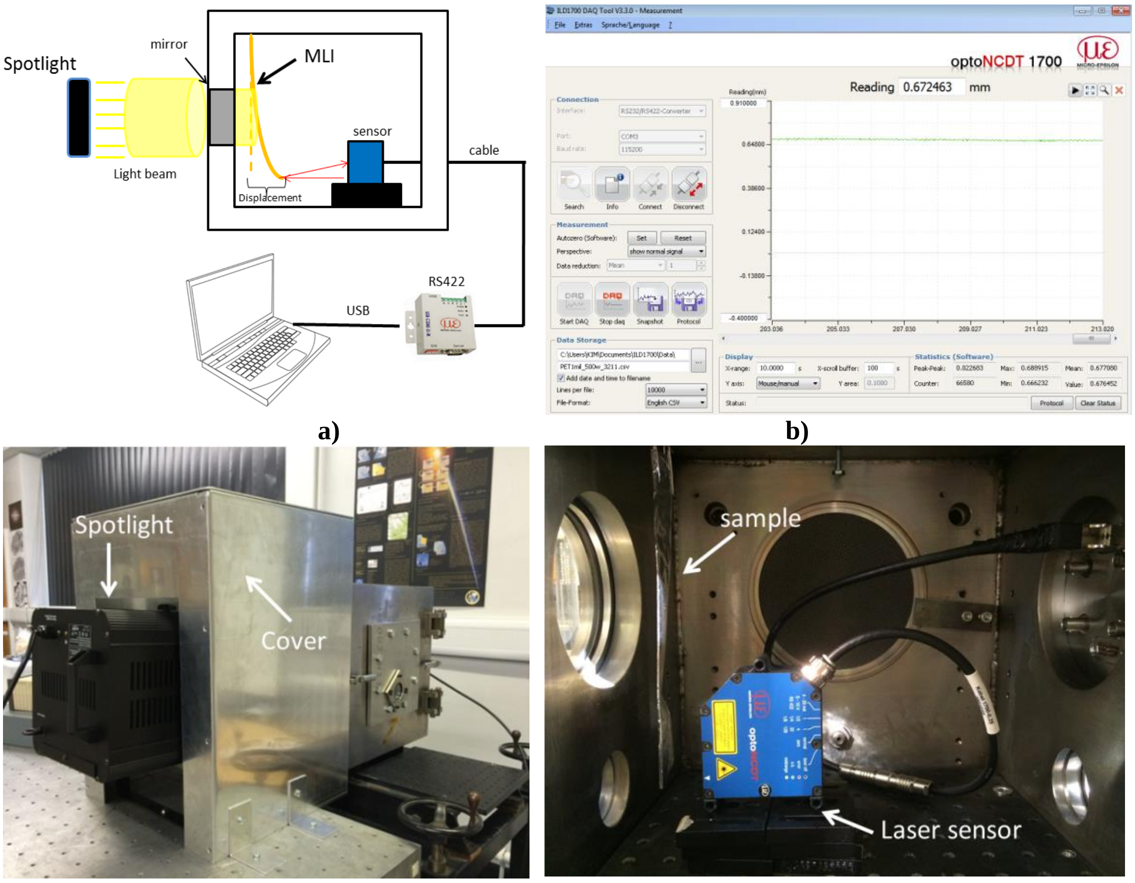

a) b)

c) d)

**Figure 5.9 Schematic drawing and experimental set up of a forced motion setup a) schematic on side view b) interface program c) outside view of the experiment d) inside view of the vacuum chamber.**

### 5.2.2.1 Radiation pressure force of the spotlight

The forced motion investigation is the experiment to measure the displacement of the free end of a membrane by exposing it to the radiation pressure from a spotlight. The aim is to replicate the effect of solar radiation pressure on the MLI element. The spotlight is assumed to emit like a perfect parabolic mirror [21] as shown in Figure 5.10. The estimation of the radiation pressure is given by:

$$I_{rad} = \frac{2P\varepsilon}{4\pi d^2} \tag{5.46}$$

Where $I_{rad}$ is radiation flux, $P$ is the power of the spotlight, $d$ is the distance of the light source from the membrane and $\varepsilon$ is the transmissivity efficiency of the clear glass window of the vacuum chamber, which is approximated as perfect ( $\varepsilon$ =1).

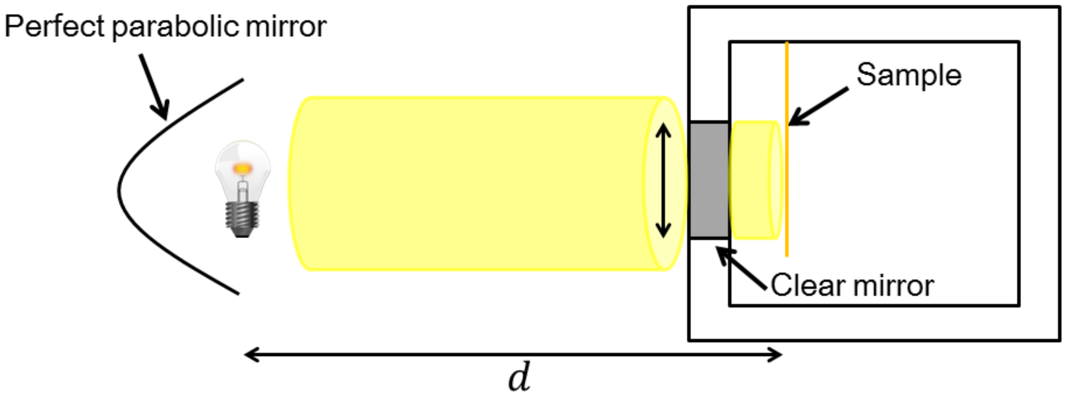

**Figure 5.10 Schematic drawing of spotlight exposure.**

In this experiment, we need to account for the specular and diffuse reflection properties of the MLI. Therefore, the solar radiation force ($\vec{F}_{\exp}$) [36] can be calculated as:

$$\vec{F}_{\exp} = \frac{I_{rad}}{C} A_{\exp} \cos(\theta_{inc}) \left\{ 2\left( \frac{C_{Rd}}{3} + C_{Rs}\cos(\theta_{inc}) \right)\hat{N} + (1-C_{Rs})\hat{S} \right\} \tag{5.47}$$

Where $A_{\exp}$ is exposed area of sample, $c$ is the speed of light (299,792,458 m/s), $C_{Rd}$ and $C_{Rs}$ are the coefficients of diffuse and specular reflectivity respectively. The relationship between $C_{Rs}, C_{Ra}$ and $C_{Rd}$ is $1 = C_{Rs} + C_{Ra} + C_{Rd}$, $\hat{N}$ is the normal unit vector of membrane, $\hat{S}$ is the spotlight incidence unit vector.

In this experiment, the spotlight operates along the x axis direction and the incident angle ($\theta_{inc}$) is perpendicular to the membrane. Then, Eq.(5.47) defines the external force acting on the MLI element.

# 5.3 Experimental results

## 5.3.1 Free motion investigation.

Figure 5.11 shows the angular motion of the Kapton 1 mil MLI element under normal atmospheric conditions. The result shows that air friction plays a lead role in supressing the motion of the MLI element. The object tracking detections of the free fall motion of PET 1 mil, Kapton 1 mil and PET 5 mils in vacuum environment are shown as in Figure 5.12, Figure 5.13 and Figure 5.14 respectively. The motions of lump masses are denoted by a blue rectangle.

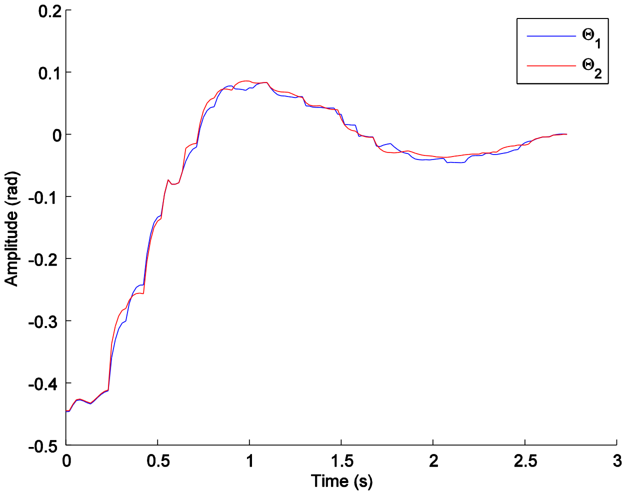

**Figure 5.11 Free vibration response of Kapton 1 mil in normal atmosphere.**

**a)** **b)** **c)**

**Figure 5.12 Detection of three red points of PET 1 mil.**

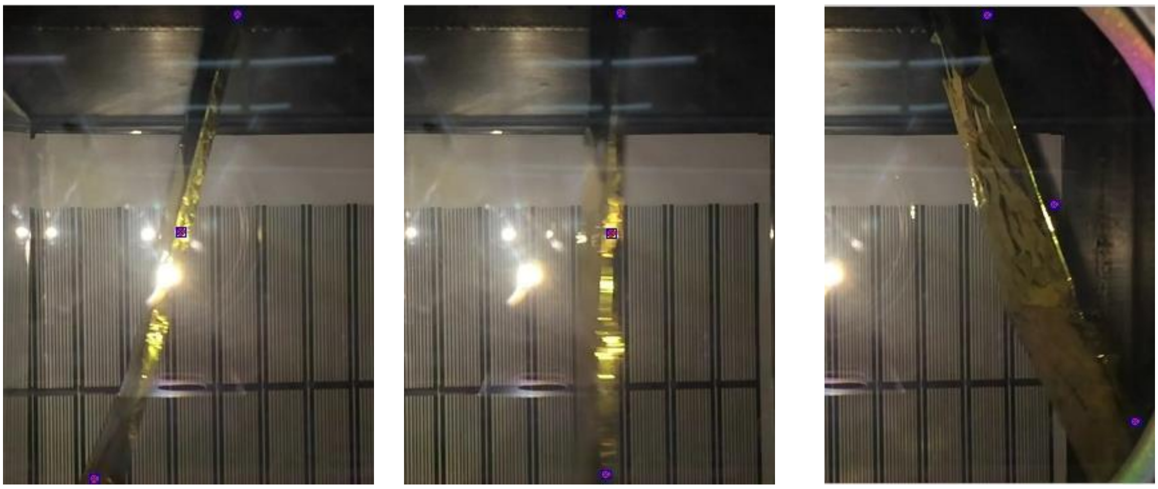

a) b) c)

**Figure 5.13 Detection of three red points of Kapton 1 mil.**

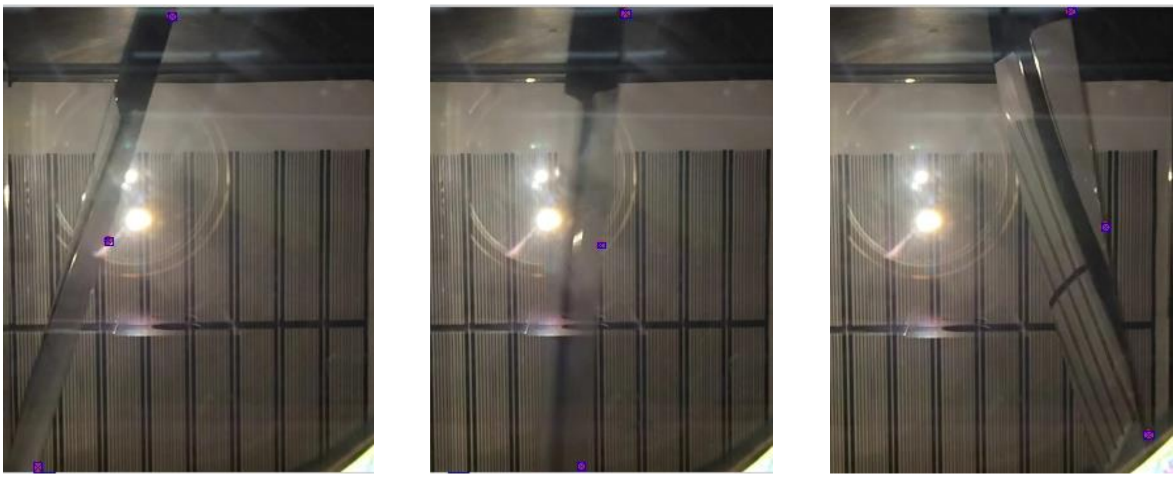

a) b) c)

**Figure 5.14 Detection of three red points of PET 5 mils.**

Figure 5.15 shows the free vibration of the deformation angles $\theta_1$ and $\theta_2$ in the time domains and frequency domains for each MLI sample. The settling times of the PET 1 mil, Kapton 1 mil and PET 5 mils are 12.41, 12.52 and 24:30 seconds respectively. The bigger mass will affect the higher gravitational potential energy. With more energy, the bigger mass will swing faster. The natural frequency, which has the same value for both $\theta_1$ and $\theta_2$, is 0.5156, 0.2109 and 1.3090 Hz. It is obvious that amplitude, settling time and natural frequency of a sample depends on its material properties and dimension. From these results, we can compute the damping ratio ($\xi$) from Eq.(5.38). The equivalent rotational spring and damping coefficients on the 2$^{nd}$ lump mass can be calculated with Eq.(5.39) and Eq.(5.40) respectively. We can see the damping ratio Table 5.2 shows the damping ratio, stiffness and damping coefficients obtained from the experimental data. We will use values in Table 5.2 to investigate the amplitude decays and natural frequencies of the multibody model.

**Table 5.2 Damping ratio, stiffness and damping coefficients of MLI sample from experimental results.**

| Material | $\xi$ | $K_{eq}$ ($\mathrm{N\cdot m/rad}$) | $C_{eq}$ ($\mathrm{N\cdot m\cdot s/rad}$) |
|---|---|---|---|
| PET 1 mil | 0.0409 | 0.0258 | 2.467E-04 |
| Kapton 1mil | 0.0441 | 0.0251 | 2.652E-04 |
| PET 5 mils | 0.0145 | 0.1162 | 4.153E-04 |

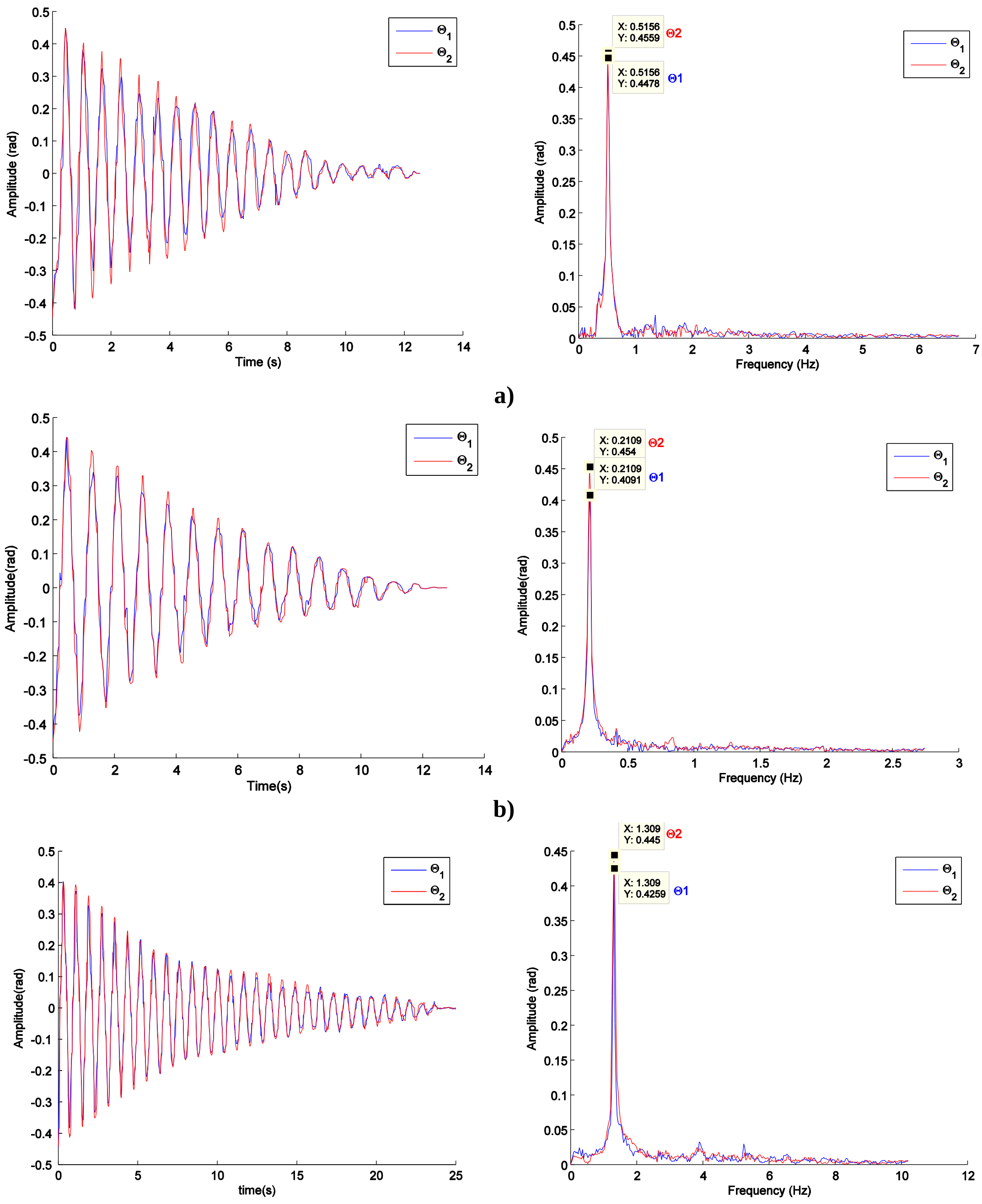

a)

b)

c)

**Figure 5.15 Free vibration response of the damping experiments in time and frequency domains a) PET 1 mil b) Kapton 1 mil c) PET 5 mils.**

The free motion simulation of the numerical multibody model of Kapton 1 mil is, for example, shown in Figure 5.16, which motion is similar as the 1st mode in Figure 5.8. The settling times of the PET 1 mil, Kapton 1 mil and PET 5 mils are shown in Figure 5.17 and are 24.30, 25.10 and 40.10 seconds respectively. As shown in the experimental results, Kapton 1 mil takes the shortest time to stabilise while PET 5 mils takes the longest. The results are coherent with the damping ratios ($\xi$), as Kapton 1 mil and PET 5 mils have the highest and lowest damping coefficient ($C_{eq}$) respectively. Comparing the experimental results with the numerical simulations, we can see that the motion appears to match well for the initial 2-3 cycles but then the settling time for the numerical results are approximately double that of the experimental results. This is caused by the presence of dissipative forces at the hinge inside the vacuum chamber.

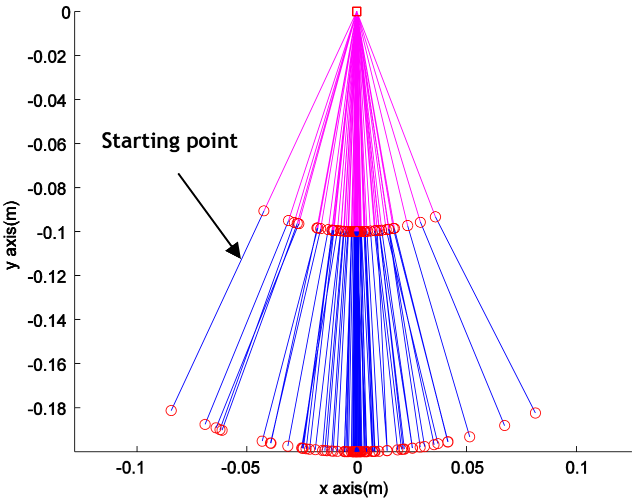

**Figure 5.16 The simulation example of free motion of multibody dynamics for Kapton (1 plot/0.5004 second).**

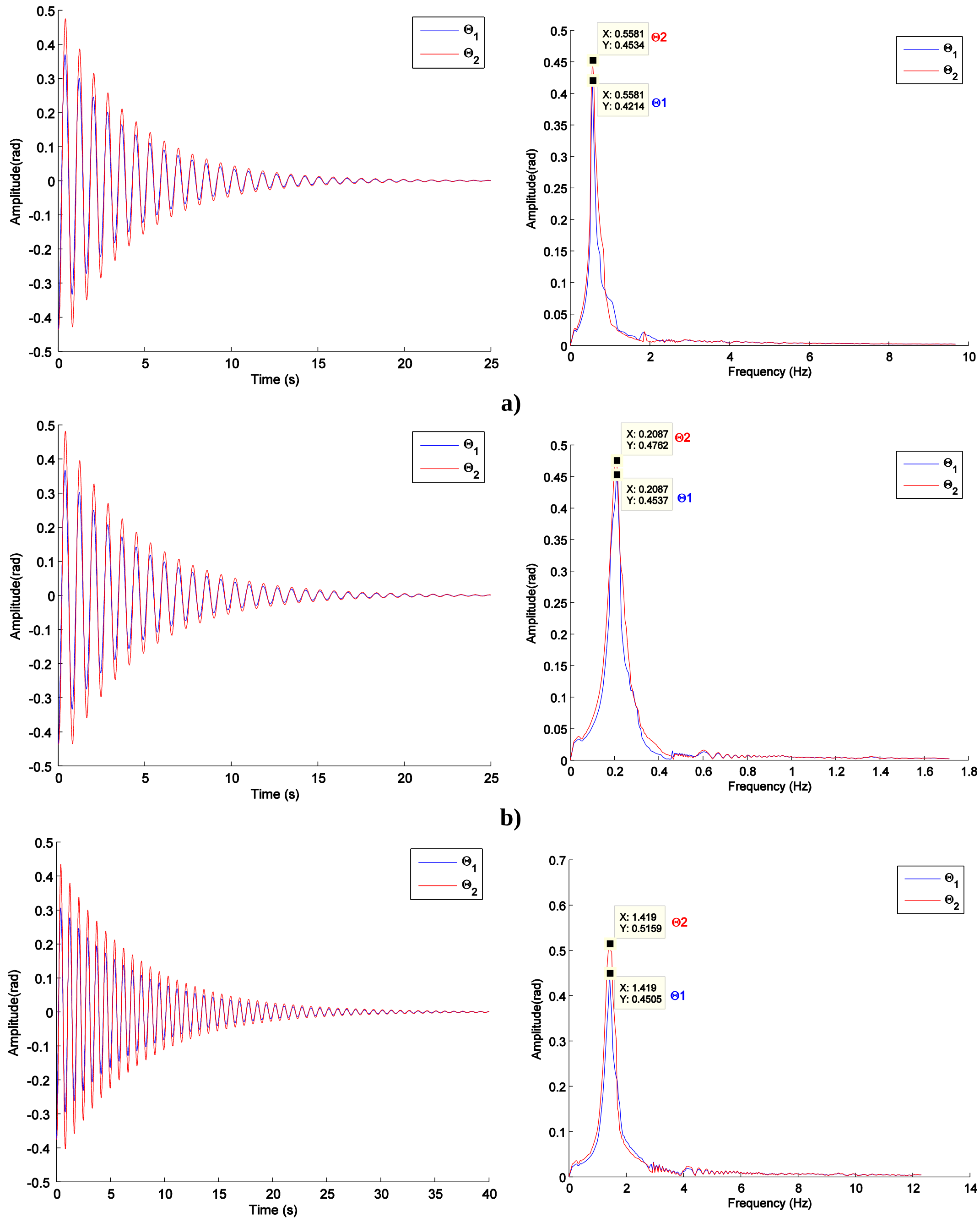

a)

b)

c)

**Figure 5.17 Free vibration response of the damping experiments in time and frequency domains a) PET 1 mil b) Kapton 1 mil c) PET 5 mils.**

The natural frequencies of the PET 1 mil, Kapton 1 mil and PET 5 mils from the experimental results in Figure 5.15 are 0.5156, 0.2109 and 1.3090 Hz which match well with the results obtained through the numerical simulations in Figure 5.17 (0.5581, 0.2087 and 1.4190 Hz respectively). We now analyse the phase of both $\theta_1$ and $\theta_2$ in order to investigate the normal mode of the oscillation response. We can see from Figure 5.15 and Figure 5.17 that in both numerical and experimental results, the amplitudes of all samples are in-phase throughout the motion. These results therefore imply that the natural frequency of all samples is in the 1st mode as shown in Figure 5.8.

The numerical results of the modal analysis of the 1st and 2nd modes of all samples with ANSYS® in Figure 5.18 is similar to normal mode of multibody model in Figure 5.8. A summary of the natural frequency values, obtained through experimental results, numerical multibody model simulations, normal mode through Eq.(5.44) and FEA are shown in Table 5.3. We can see that the natural frequency for all samples appear to be very similar.

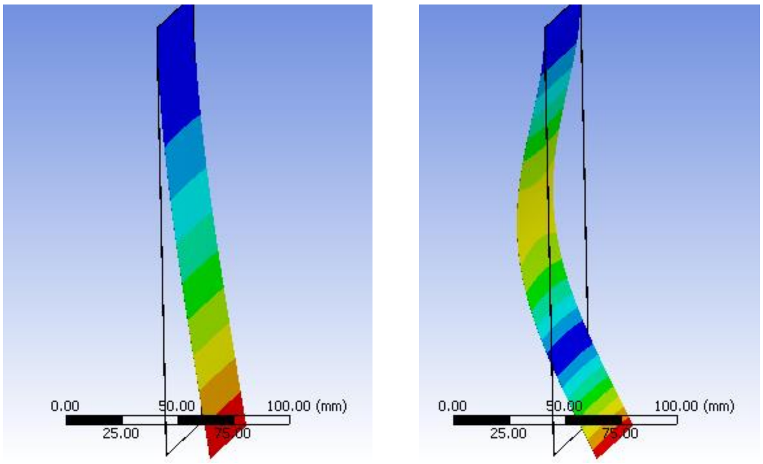

**a)** **b)**

**Figure 5.18 Mode shape from FEA(ANSYS®): Natural modes a) the 1st mode b) the 2nd mode.**

**Table 5.3 Natural frequency comparison.**

| Material | Natural Frequency (Hz) | | | | | |
|---|---|---|---|---|---|---|
| | Free vibration simulation (MATLAB®) | Free vibration method (Experiment) | Normal mode | | Free vibration method (ANSYS®) | |
| | $f_1$ | $f_1$ | $f_1$ | $f_2$ | $f_1$ | $f_2$ |
| PET 1 mil | 0.5581 | 0.5156 | 0.5265 | 1.3474 | 0.5350 | 1.3815 |
| Kapton 1mil | 0.2087 | 0.2109 | 0.2299 | 0.6147 | 0.2095 | 0.6270 |
| PET 5 mils | 1.4190 | 1.3090 | 1.3480 | 8.1566 | 1.3338 | 8.3209 |

### 5.3.2 Forced motion investigation

To determine the motion of the MLI samples subject to external forces, we illuminate the samples with a high power spotlight. The spotlight is calibrated at four different power values (500, 1000, 1500 and 2000 W) and each experiment (coupling of MLI sample and power intensity) is ran five times with the results then averaged. Figure 5.19 shows that the numerical and FEA results align well with the experimental results. All results show very small displacements in the order of micrometres. The displacement of the numerical result is lower than that for FEA and experiment, which all results nevertheless show small nonlinear behaviour in all membrane types.

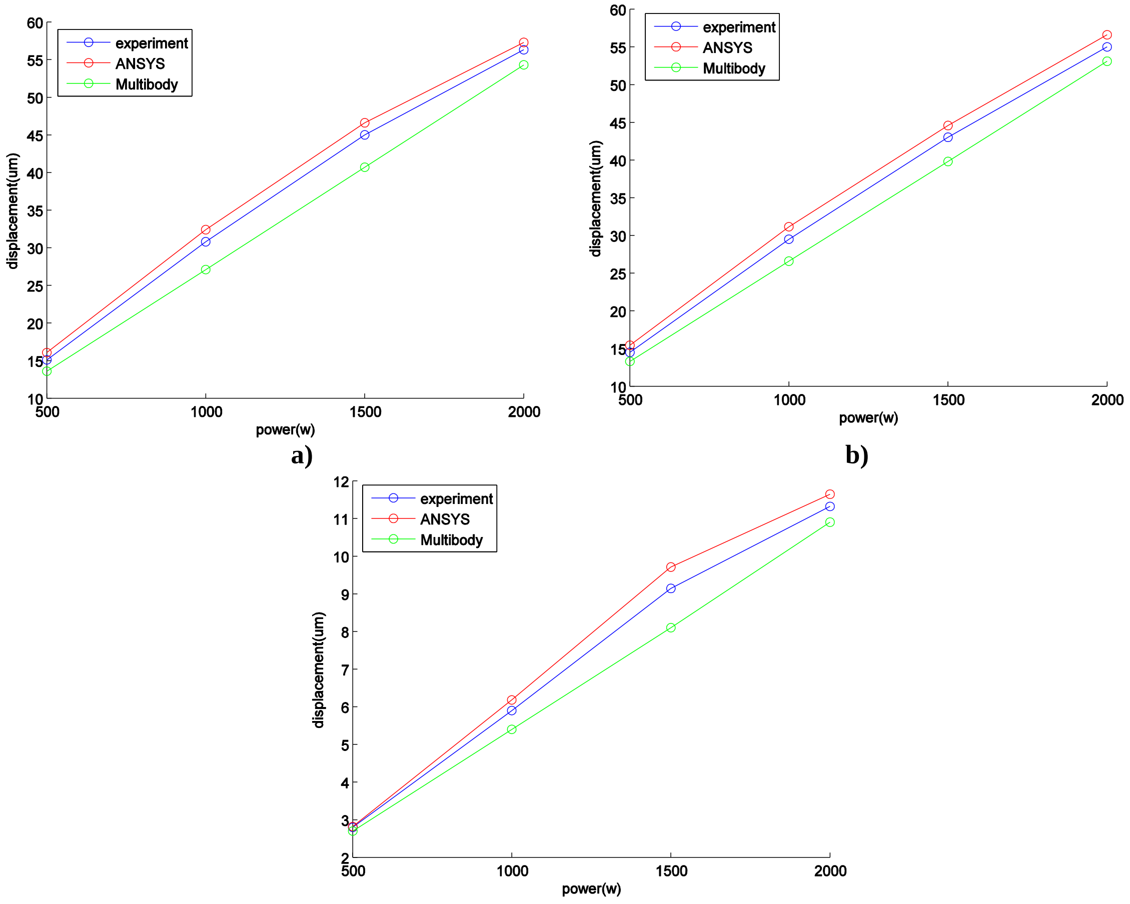

a) b)

c)

**Figure 5.19 Comparison of displacement results of forced motion experiment, FEA and multibody dynamics a) PET 1 mil b) Kapton 1 mil c) PET 5 mils.**

In Figure 5.4, Δ is the relative error of the displacement of the numerical and FEA compared to the experimental results. The relative error of the numerical model is the largest (12.01%) at 1000W while the relative error of FEA has the maximum relative error at 500W for both PET 1 mil (6.46%) and Kapton 1 mil (6.48%) but the relative minimum error is PET 5 mils (0.70%). The relative error of both numerical and FEA of all membrane types at 2000W is less than the relative error at 1000W and 1500W for all cases but not that of the relative error of FEA (PET 5 mils, Δ = 0.70%) at 500W. To summarise, the relative error range of the numerical model is 3.45-12.01% while the relative error range of FEA is 0.70-6.48%. This suggests that the finite element analysis software handles a nonlinear problem better than the numerical model. However, when the deformation motion is coupled with the attitude and orbital dynamics propagation the computational cost of using such a software becomes unduly large. With this in mind, the numerical model appears to be more than adequate to provide a fairly accurate first estimate of the motion of an orbiting MLI element subject to environmental perturbations.

**Table 5.4 The relative error of the analytic simulation (Multibody model and FEA) compared to the measured displacement.**

| Material | Method | Δ (%error) | | | |
|---|---|---|---|---|---|
| | | 500(w) | 1000(w) | 1500(w) | 2000(w) |
| PET 1 mil | Multibody | -9.93 | -12.01 | -8.13 | -3.55 |
| | FEA | 6.46 | 5.19 | 5.20 | 1.73 |
| Kapton 1mil | Multibody | -8.28 | -9.83 | -7.48 | -3.45 |
| | FEA | 6.48 | 5.59 | 5.62 | 2.90 |
| PET 5 mils | Multibody | -3.57 | -8.49 | -11.40 | -3.71 |
| | FEA | 0.70 | 4.75 | 6.20 | 2.88 |

## 5.4 Summary

This chapter described the experimental setup used to validate the numerical, multibody model introduce in Chapter 4. The first experiment (free motion experiment) is performed to determine the damping characteristics of the membranes and their fundamental natural frequencies. The second experiment addresses the forced motion of a membrane exposed to a radiation pressure from a high power spotlight. The experimental results are then used to validate the numerical simulations of multibody model as well as compared to normal mode and FEA results.

The results from the free motion experiment allow us to determine the damping characteristic and natural frequencies of a thin and low strength membrane. The values of the natural frequencies obtained through the experiment show good agreement with and the numerical results. The experimental results for the settling time are however substantially shorter than the numerical ones but this appears to be due to residual dissipative forces presenting during the experiment. The results for the forced motion experiment show that the numerical multibody model has good agreement with the experimental results. The relative errors obtained by means of FEA are better than those achieved through the numerical model, but when coupled with attitude and orbit dynamics propagation the computational costs of using such a software become almost prohibitive.

6

# 6 Conclusions

This dissertation presents the development of an effective and simple flexible model to represent HAMR objects, by means of Bernoulli and multibody models and compares their orbital dynamics with that of rigid models (flat plate and cannonball). The computational model for the flexible body is then validated through vacuum chamber experiments. This final chapter summarizes and comments the work done and the findings of this thesis. The last section of this chapter will discuss limitations of this dissertation and possible future investigations.

Unexpected HAMR space debris discovered in the GEO region is thought to be MLI materials separated from the spacecraft due to fragmentation, collision events or aging process. The observation of spectral measurements provide that HAMR debris are very fast rotation and very sensitive to SRP, unstable AMR and reflection to a light (light curve). The investigation in Chapter2 show that attitude dynamics of this debris play one of important factors leading unique orbital prediction when comparing with rigid object due to vary SRP but it does not answer the unstable AMR. Therefore, Chapter 3 and Chapter 4 show two approaches to model and integrate deformable, highly reflective membranes in GEO orbits. The first model (Chapter 3) is based on modelling the flexibility of the membrane as Bernoulli-Euler beam theory and the second model (Chapter 4) discretizes the membrane with lump masses connected by rods. Both approaches assume that the membrane can fold along one folding line, which remains fixed on the membrane. However, both approaches can be extended by considering more folding lines, at additional computational cost.

Both approaches were used to predict the orbit of a typical GEO debris, and compared with other propagation methods by using rigid body approximation (cannonball and flat rigid plate), and showed sensible differences in the evolution of the orbital parameters, particularly inclination and eccentricity.

The linear approach (small deformation) of Bernoulli model is somewhat intrinsically limited due to the fact that large displacements that need to update the stiffness of the body at every time step that will take more additional cost of computation cannot be correctly model large membranes, whose deformations are clearly not limited in principle. The multibody approach overcomes this limitation and at the lower cost of computational effort. However, the speed of computation by using ODE45 is able to improve by optimizing relative tolerance (RelTol) and absolute tolerance (AbsTol) or change the numerical method that provide many integration function in MATLAB® because each Methods intended to solve different stiff problems efficiently do more work per step, but can take much bigger steps. At each step, they use MATLAB matrix operations to solve a system of simultaneous linear equations that helps predict the evolution of the solution [65].

The Earth gravity ($J_2$), SRP, gravitational attraction of the Sun and Moon, self-shadowing effects were all considered in the propagation. However, as it was mentioned in the introduction, because MLI membranes are aluminized and hence conductive, self-induced currents are also an important source of internal forces that contribute to the attitude dynamics and the deformation of the sheet. SRP perturbation is the main contributor to changes in the cross-sectional area of the flexible model leading to variations in shapes and inducing rapid and irregular tumbling and unique orbital motion when compared to the rigid approach. In addition, the results also suggest that the self-shadowing effect plays a significant role in the attitude and orbital motion when compared to the results without self-shadowing.

Monte Carlo simulation by varying initial conditions for the attitude configuration and different initial shape of the multibody model lead to significant changes in the Keplerian elements over both short and long term propagations. It is worthwhile noting that the more accurate the shape of the MLI debris can be defined, the more precision the propagation of translational and rotational motions will be.

Although all flexible body methods were matched to equivalent rigid-body approximations, and the results of the orbital integration were compared, no validation of either approach was done using real space debris data from empirical observations.

Potentially, light curves of flexible debris could be estimated by considering the relative position and attitude with respect to the sun and an observer on the Earth. Simulations could be carried out by assuming that a particular debris object is a deformable MLI sheet, and then matching the simulated attitude/deformation motion with the observed light curve. However, these would depend on extremely precise initial conditions, as well as characteristics (size, thickness, reflection properties and material type) of the debris sheet, which are not available, making this type of validation extremely difficult.

In addition, the multibody approach makes use of discrete rotational springs and dampers to account for the bending stiffness of the membrane. The spring and damper constants were estimated through semi-empirical formulas, based on the data of the materials of the typical MLI membranes. These estimations however can be wrong because of the extremely thin nature of the membrane itself. The first experiment in Chapter 5 (free motion experiment) was be set up, in order to have a better estimation of these parameters. An MLI sheet is held hanging on the top wall of a vacuum chamber. The sheet is then displaced from its equilibrium position along the vertical, and left swinging due to gravity. The amplitude and frequency of oscillation over time (monitored through a glass window by using image process technique to measure the movement) are related to the elastic properties of the membrane. The vacuum chamber ensures that the effect of the air friction is negligible. The rotational spring and damper in the multibody model can then tuned such that the response of the model matches that of the real membrane. The second experiment (forced motion experiment) by means of a high energy spotlight replicating solar radiation exposure has been performed and the displacement is measured by a laser sensor. Both experiments performed on three different samples show fairly good agreement with multibody model and the FEM simulation (ANSYS®). The relative errors in the FEA are better than those in the multibody model. This is due to FEA being able to better solve systems with higher degrees of freedom. Long term orbital propagation of HAMR objects by means of FEA will however require high computational costs. However, the multibody model, while possibly less accurate, does enable orbital propagation HAMR debris at substantially lower computational costs.

The outcomes of this work have a direct effect on the ability to predict the long term evolution of HAMR debris. It will provide a clearer understanding of MLI-type debris, thus enabling the community to develop appropriate mitigation strategies and enhances the reliability and success probability of current and future space mission by minimising the possibility of debris impact. For example, the flexible model will allow to increase solution ranges of the orbital debris models developed by NASA and ESA (e.g. EVOLVE, GEO EVOLVE, LEGEND and MASTER 2009) including break up model of debris from collision or explosion events.

Other application areas can also benefit from this work. More accurate orbital propagation of space debris can enhance active debris removal concepts such as drag sail or robotic arm or allow the development of new concepts for space debris removal. Additionally flexible spacecraft appendages such as antennas and solar panels can benefit from the flexible model developed here as attitude slews often cause dynamic deformation in these structures. Finally, more accurate prediction of solar sail dynamics can be improved by extending the flexible model to the entire sail as well as future large space structures, which such as solar power satellites which will be highly flexible and have high area to mass ratios.

## 6.1 Limitations and future work

The flexible model developed here is currently able to represent deformations only in one direction, which is perpendicular to the membrane. Improvement of this model, therefore, should focus on increase the deformation directions as well as increasing the number of lump masses from the current three. The more accurate the modelling of the real shape is, the more precise the orbital propagation will be. This will however come at substantial computational costs.

Due to budget constraints, we were not able to determine, during the experimental campaign the thermal expansion of the MLI membrane, which may be responsible for part of the material deformation due to thermal bending. Moreover, the validation of the radiation pressure force of Eq.(5.47) from the spotlight can be validated by a light detector to measure the actual power of the spotlight on a membrane, comparing it with the calculation of the radiation exposure equation. To summarise, further investigations can be concluded as following:

### Future development of the flexible model

- Increase the number of lump masses and allow for more directions of the deformation in order to improve the more accuracy of shape by accepting higher computational cost.

- Investigate attitude and orbital motions due to electrostatic charging of the flexible model [33].

- Investigate the Earth's shadow effects on the attitude-orbit dynamics of flexible model.

- Request the observation data from Astronomical Institute of the University of Bern (AIUB), which have the huge data of HAMR debris and investigate the light curve and orbital evolution of flexible model based on the same initial conditions of real observations [11, 12, 16] of HAMR debris and compare the simulated results with the observed .

- To speed up ODE function, there is two possible ways to do. Firstly, it is good idea to play with RelTol and AbsTol settings. Secondly, if a simulation still take long time, it is possible the dynamics that is stiff problem. We can try to change the numerical method. MATLAB [65] have many integrations such as ODE23, ODE113, ODE15s, ODE23s, ODE23t and ODE23tb and compare the speed of each integration.

### Further experiments

- Validate the exposure equation in chapter 5 and thermal expansion bending by means of a light detector and thermal sensor.

- Investigate the effect of thermal transpiration in the forced motion experiment by using Crookes radiometer

- Zero-g weightlessness experiment for further validation of the model

# Appendix A

## Appendix A

## A.1 Sun vector

The number of Julian centuries ($T_{TDB}$) required to define the Earth-Sun vector [36] at any given time is given by:

$$T_{TDB} = \frac{JD - 2451545}{36525} \tag{A.1}$$

Where $T_{TDB}$ is the number of Julian centuries based on barycentric dynamical time (TDB) and $JD$ is Julian Date. And then using the number of Julian centuries is to calculate the solar mean anomaly ($M_{\odot}$), mean longitude of the Sun ($\lambda_{\odot M}$), ecliptic longitude of the Sun($\lambda_{\odot ecliptic}$), magnitude of the distance to the Sun ($r_{\odot}$) and the obliquity of the ecliptic ,ε, can be calculated as:

$$M_{\odot} = 357.5277233° + 35999.05034 T_{TDB} \tag{A.2}$$

$$\lambda_{M_{\odot}} = 280.460° + 36000.770 T_{TDB} \tag{A.3}$$

$$\lambda_{\odot ecliptic} = \lambda_{M_{\odot}} + 1.914666471 \sin(M_{\odot}) + 0.019994643 \sin(2M_{\odot}) \tag{A.4}$$

$$r_{\odot} = 1.000140612 - 0.0167086 \cos\left(M_{\odot}\right) - 0.000139589 \cos(2M_{\odot}) \tag{A.5}$$

$$\varepsilon = 23.439291 - 0.0130042 T_{TDB} \tag{A.6}$$

The distance between the Earth and the Sun vector ($\vec{r}_{\odot}$) referred to the epoch date is :

$$\vec{r}_1 = r_{\odot} \begin{bmatrix} \cos(\lambda_{\odot ecliptic}) \\ \cos(\varepsilon)\sin(\lambda_{\odot ecliptic}) \\ \sin(\varepsilon)\sin(\lambda_{\odot ecliptic}) \end{bmatrix} \tag{A.7}$$

## A.2 Moon vector

The Moon position with respect to the Earth [36] requires to Julian centuries as similar as the sun vector and is calculate as:

$$\begin{aligned}\lambda_{\text{☾}ecliptic} = {} & 218.32° + 481,267.883T_{TDB} \\ & + \ 6.29\sin\left(134.9 + 477,198.85T_{TDB}\right) \\ & -1.27\sin\left(259.2 - 413,335.38T_{TDB}\right) \\ & +0.66\sin\left(235.7 + 890,534.23T_{TDB}\right) \\ & +0.21\sin\left(269.9 + 954,397.70T_{TDB}\right) \\ & -0.19\sin\left(357.5 + 35,999.05T_{TDB}\right) \\ & -0.11\sin\left(186.6 + 966,404.05T_{TDB}\right)\end{aligned} \tag{A.8}$$

$$\begin{aligned}\phi_{\text{☾}ecliptic} = {} & 5.13°\sin\left(93.3 + 481,202.03T_{TDB}\right) \\ & +0.23\sin\left(228.2 + 960,,400.87T_{TDB}\right) \\ & -0.28\sin\left(318.3 + 6003.18T_{TDB}\right) \\ & -0.17\sin\left(217.6 + 407,332.20T_{TDB}\right)\end{aligned} \tag{A.9}$$

$$\begin{aligned}\rho = {} & 0.9508° + 0.0518\sin\left(134.9 + 477,198.85T_{TDB}\right) \\ & +0.0095\cos\left(259.2 + 413,335.18T_{TDB}\right) \\ & +0.0078\cos\left(235.7 + 890,534.23T_{TDB}\right) \\ & +0.0028\sin\left(269.9 + 954,397.70T_{TDB}\right)\end{aligned} \tag{A.10}$$

$$\varepsilon = 23.439291° - 0.0130042T_{TDB} - 1.64x10^{-7}\,T_{TDB}^{2} + 5.04x10^{-7}\,T_{TDB}^{3} \tag{A.11}$$

$$r_{\text{☾}} = \frac{1}{\sin\rho} \tag{A.12}$$

Where $\lambda_{\text{☾}ecliptic}$ is ecliptic longitude of the moon, $\phi_{\text{☾}ecliptic}$ is ecliptic latitude of the moon, ρ is the horizontal parallax and $\varepsilon$ is the obliquity of the ecliptic. And then the moon position vector in the Earth radius is as:

$$\vec{r}_2 = r_{\text{☾}}\begin{bmatrix}\cos(\phi_{\text{☾}ecliptic})\cos(\lambda_{\text{☾}ecliptic}) \\ \cos(\varepsilon)\cos(\phi_{\text{☾}ecliptic})\cos(\lambda_{\text{☾}ecliptic}) - \sin(\varepsilon)\sin(\phi_{\text{☾}ecliptic}) \\ \sin(\varepsilon)\cos(\phi_{\text{☾}ecliptic})\cos(\lambda_{\text{☾}ecliptic}) + \cos(\varepsilon)\sin(\phi_{\text{☾}ecliptic})\end{bmatrix} \tag{A.13}$$

# Appendix B

## B.1 Moment of inertia

The inertia tensor, a matrix of the moments of inertia, will take place in all three coordinate axis, x, y and z [42].

$$\begin{bmatrix} I_{xx} & -I_{xy} & -I_{xz} \\ -I_{yx} & I_{yy} & -I_{yz} \\ -I_{zx} & -I_{zy} & I_{zz} \end{bmatrix} \tag{B.1}$$

It is assumed that the origin of the body frame is positioned on the centre of mass of all simulated objects. In this case, all components spare the diagonal of the moment of inertia tensor become zero:

$$I = \begin{bmatrix} I_{xx} & 0 & 0 \\ 0 & I_{yy} & 0 \\ 0 & 0 & I_{zz} \end{bmatrix} \tag{B.2}$$

In this work, there are two objects of this thesis to compute moment of inertia for attitude dynamics such as a thin flat plate and thin rod.

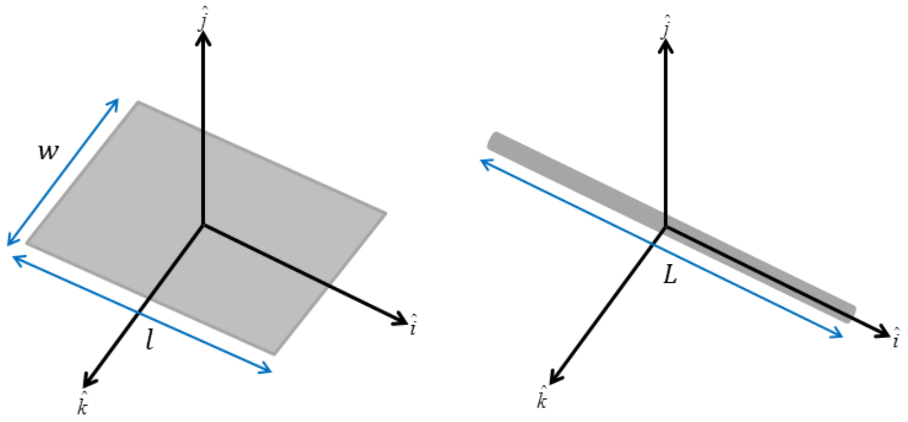

a) b)

**Figure B.1 Moment of inertia in the body frame a) a flat plate b) a beam**

### B.1.1Moment of thin flat plate.

$$I_{xx} = m(w^2)/12 \\ I_{yy} = m(w^2 + l^2)/12 \\ I_{zz} = m(l^2)/12 \tag{B.3}$$

### B.1.2Moment and thin rod

$$I_{xx} = 0 \\ I_{yy} = m(l^2)/12 \\ I_{zz} = m(l^2)/12 \tag{B.4}$$

## B.2 Parallel axis theorem

The moment of inertia of a flexible models consisting of 2 beam elements in a particular axis (Figure B.2) is equal to the moment of inertia around parallel axis that goes through the centre of mass. In this case, we define the centre of mass on the 2nd node. The moment of inertia about any axis parallel through the centre of rotation is given by:

$$I = I_{CM} + md^2 \tag{B.5}$$

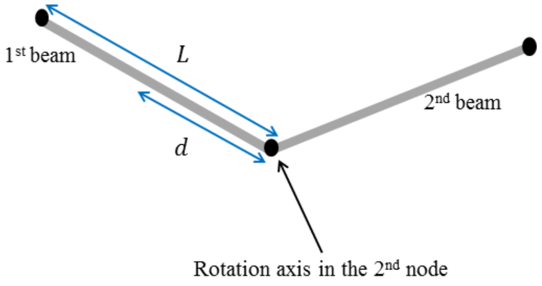

**Figure B.2 Moment of inertia of flexible model by centre of mass at the 2nd node.**

In flexible model based on finite element method, the 2nd node (the end of rod) is defined the centre of rotation of the flexible model. The moment of inertial of the 1st and 2nd beam elements at 2nd node are expressed as:

$$I_{2^{nd}\,node} = \frac{1}{12}ml^2 + \frac{1}{4}ml^2 = \frac{1}{3}ml^2 \tag{B.6}$$

# Appendix C

## C.1 Rayleigh damping

The Reylieigh damping [44] is one of the simplest methods to approximate damping and often utilized in FEM simulation.

$$[C] = \alpha[M] + \beta[K] \tag{C.1}$$

Where $[C]$ is damping matrix of physical system, $[M]$ is mass matrix of physical system and $[K]$ is stiffness matrix. $\alpha$ and $\beta$ are constants with unit of s$^{-1}$ and s respectively. In the formulation of Rayleigh damping orthogonal transformation of damping matrix reduces to matrix to form the equation

$$2\xi_i\omega_i = \alpha + \beta\omega_i^2 \tag{C.2}$$

Where $\xi_i$ is damping ratio of $i^{\text{th}}$ mode and $\omega_i$ is the natural frequency of $i^{\text{th}}$ mode. Finally, we write this equation in term of damping ratio ( $\xi_i$ ) in term of LHS.

$$\xi_i = \frac{\alpha}{2\omega_i} + \frac{\beta\omega_i}{2} \tag{C.3}$$

From Eq. (C.3), it can explain that when frequency ( $\omega_i$ ) will be the small, term of $\alpha / 2\omega_i$ will dominate, and as $\omega_i$ will increase the term $\beta\omega_i$ will start domination and $\alpha / 2\omega_i$ will approach to zero as shown in Figure C.1

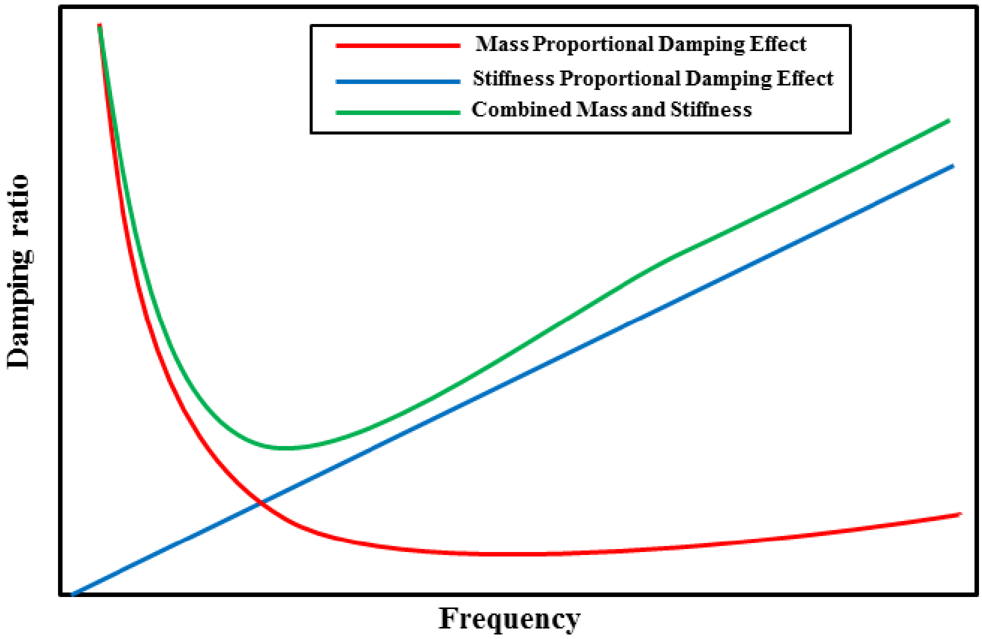

**Figure C.1 Frequency effect of proportional damping on damping ratio.**

The mass and stiffness proportional coefficients from $\omega_i$ to $\omega_j$ can be solved from the Eq. (C.3). Then, they are given by:

$$\alpha = 2\omega_i\omega_j \frac{\xi_j\omega_j - \xi_i\omega_i}{\omega_j^2 - \omega_i^2} \qquad \text{(C.4)}$$

$$\beta = 2\frac{\xi_j\omega_j - \xi_i\omega_i}{\omega_j^2 - \omega_i^2}$$

In practical engineering, it is very difficult to calculate value of damping ratio for all the modes. The selecting damping ratio is typically simplified to be constant for all significant modes. In this investigation of the flexible model based on FEA theory, we define the damping ratio of this MLI as equal as 5% and consider modes of natural frequencies from 1th mode to 8th modes, which are determined by commercial programme software (ANSYS®) as shown in Figure C.2. The boundary of thin membrane is set none of any support. As a result, we can compute as equal as $\alpha$ and $\beta$ as 0.0334 $s^{-1}$ and 0.0475 s respectively.

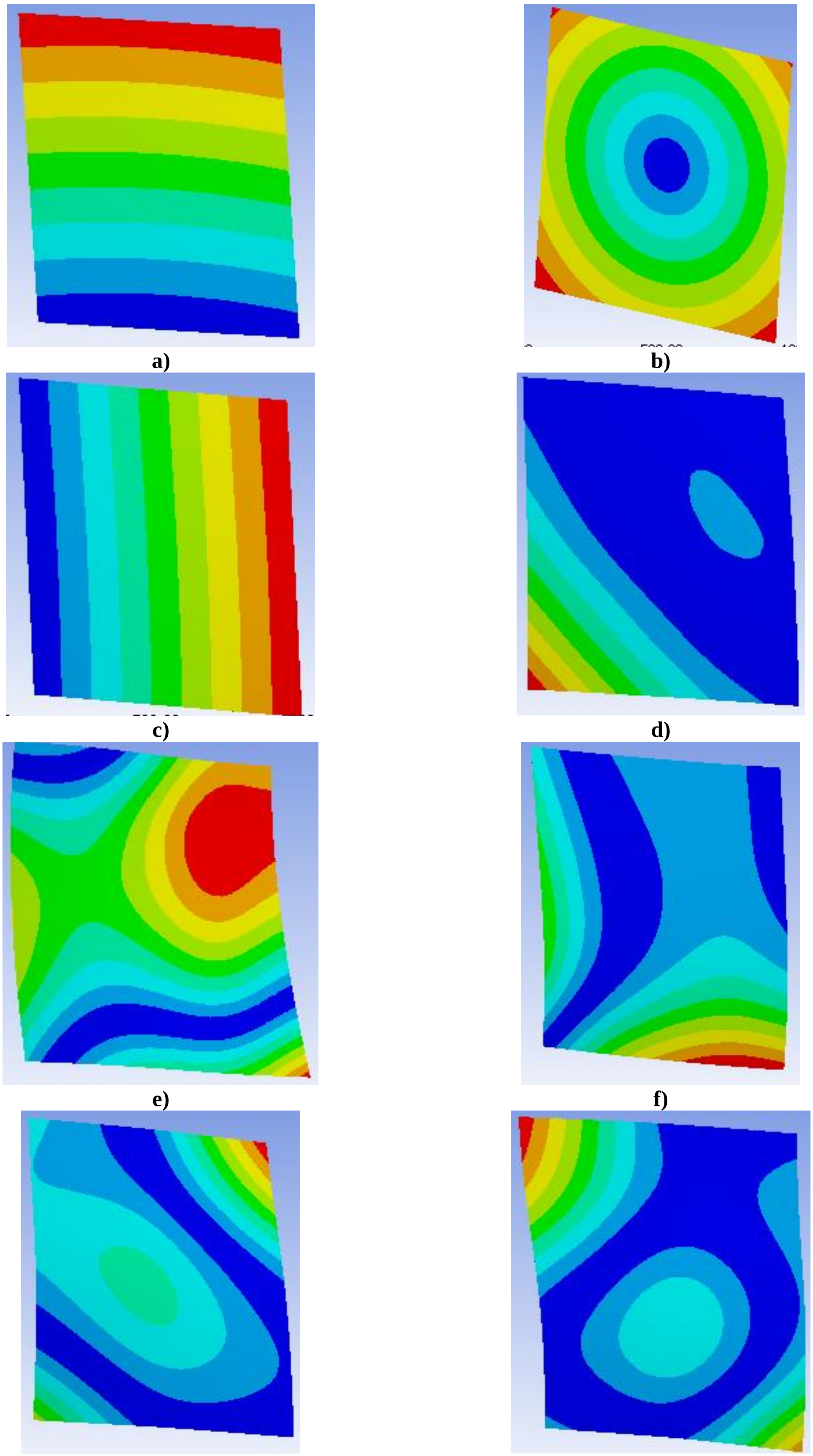

a) b) c) d) e) f) g) h)

**Figure C.2 Natural frequency response of PET (1x1 m$^2$) in 8 modes a) 1st mode: 0.0021 Hz b) 2nd mode: 0.0134 Hz c) 3rd mode: 0.0662 Hz d) 4th mode: 0.2366 Hz e) 5th mode: 0.2414 Hz f) 6th mode: 0.2484 Hz g) 7th mode: 0.2562 Hz h) 8th mode: 0.2688 Hz.**

## C.2 Shear Modulus

In the simplest case of an isotropic material, the relationship between young modulus and shear modulus of isotropic material is given as:

$$G_y = \frac{E_y}{2(1+\nu)} \tag{C.5}$$

Where $G_y$ is shear modulus, $E_y$ is young modulus and $\nu$ is Poisson’s ratio.

# Appendix D

## Appendix D

### D.1 Sampling of Monte Carlo simulation

The Latin hypercube sampling (LHS) is used for sampling attitude motions ($\psi, \theta, \phi$) and deformed angle ($\theta_d$). The results of 4 variables in uniform distribution [0,1] can be shown in 4 plots in Figure D.1.

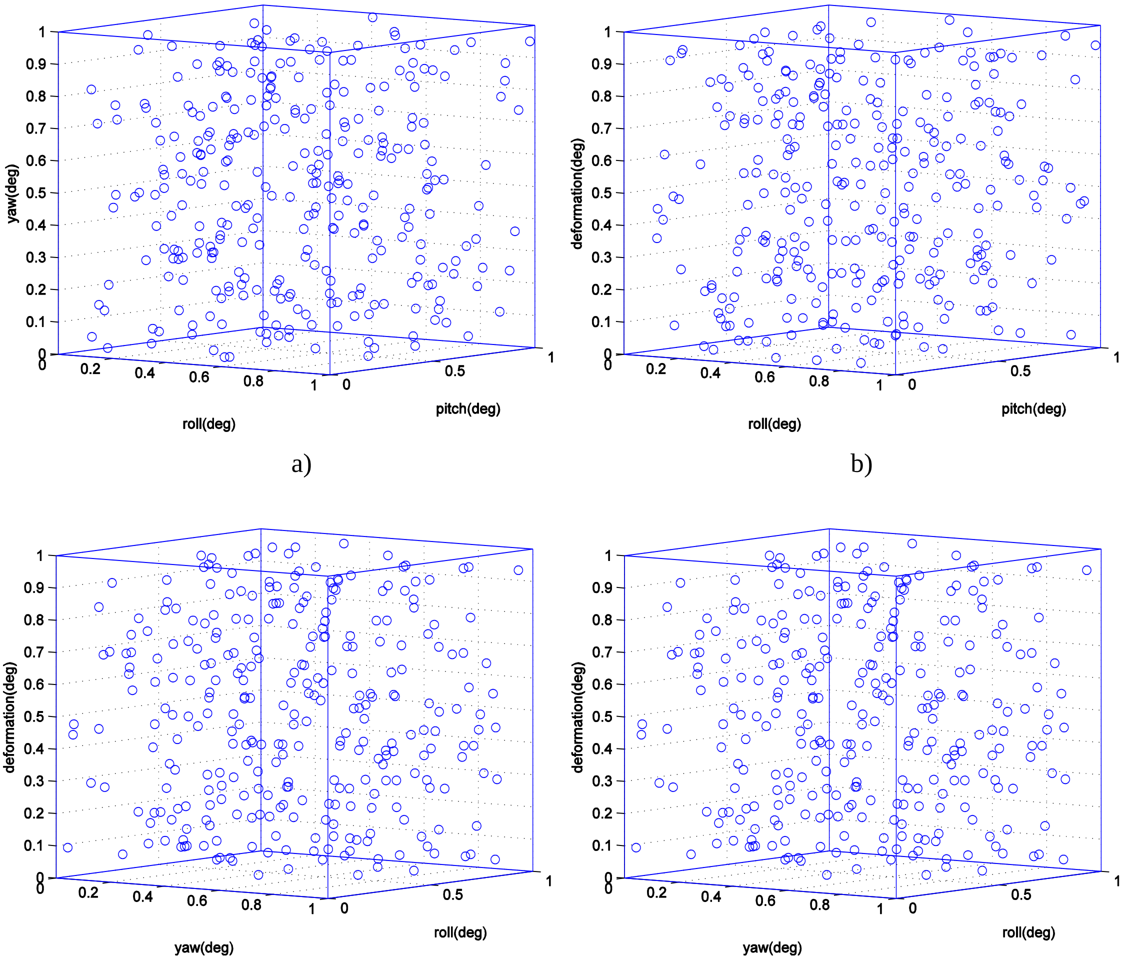

a)

b)

c)

d)

**Figure D.1 Three-dimensional plot of sampled points by using Latin hypercube in against each other of the 4 parameter space (roll, pitch, yaw and deformed angle) a) roll, pitch, yaw b) roll, pitch, deformed angle c) yaw, roll, deformed angle d) yaw, roll, deformed angle**.

The results of 300 different initial conditions in the actual range of 3 rotational angles and deformed angle are shown in Table D.1

**Table D.1 300 initial conditions by using LHS sampling**.

| Sampling NO. | Yaw(deg) | pitch(deg) | Roll(deg) | Deformed angle(deg) |
|---|---|---|---|---|
| 1 | 162.05 | 172.01 | 37.40 | 220.57 |
| 2 | 9.71 | 100.18 | 22.96 | 306.27 |
| 3 | 40.23 | 157.96 | 45.37 | 343.66 |
| 4 | 17.50 | 133.99 | 110.60 | 352.87 |
| 5 | 103.06 | 26.09 | 108.59 | 323.41 |
| 6 | 87.24 | 0.72 | 96.84 | 13.97 |
| 7 | 20.08 | 138.06 | 116.80 | 19.42 |
| 8 | 140.53 | 97.20 | 134.93 | 134.01 |
| 9 | 132.67 | 41.76 | 57.80 | 33.63 |
| 10 | 32.78 | 127.66 | 54.87 | 144.75 |
| 11 | 114.11 | 119.92 | 94.69 | 266.29 |
| 12 | 145.37 | 153.94 | 129.96 | 313.17 |
| 13 | 148.98 | 62.50 | 161.10 | 120.56 |
| 14 | 73.66 | 58.99 | 63.34 | 325.08 |
| 15 | 147.52 | 50.22 | 42.22 | 230.50 |
| 16 | 11.82 | 3.38 | 25.11 | 156.33 |
| 17 | 20.92 | 48.49 | 63.64 | 295.85 |
| 18 | 146.77 | 151.58 | 8.48 | 357.27 |
| 19 | 100.82 | 28.65 | 64.64 | 138.20 |
| 20 | 163.66 | 102.97 | 23.69 | 177.53 |
| 21 | 37.63 | 15.48 | 105.91 | 221.33 |
| 22 | 153.76 | 147.33 | 154.18 | 150.49 |
| 23 | 12.51 | 170.95 | 158.76 | 224.03 |
| 24 | 108.69 | 52.04 | 97.57 | 219.16 |
| 25 | 10.34 | 42.32 | 133.70 | 288.01 |
| 26 | 51.11 | 165.34 | 79.29 | 212.86 |
| 27 | 45.66 | 146.39 | 5.01 | 97.42 |
| 28 | 54.07 | 137.90 | 36.89 | 168.48 |
| 29 | 108.59 | 95.60 | 42.77 | 159.53 |
| 30 | 123.87 | 107.05 | 99.55 | 133.13 |
| 31 | 168.13 | 109.09 | 16.24 | 327.08 |
| 32 | 117.55 | 75.99 | 80.98 | 128.78 |
| 33 | 115.05 | 144.82 | 105.46 | 195.99 |
| 34 | 79.53 | 29.69 | 149.70 | 69.17 |
| 35 | 69.92 | 21.09 | 119.31 | 183.01 |
| 36 | 92.47 | 98.34 | 144.45 | 54.99 |
| 37 | 155.24 | 103.22 | 15.66 | 191.87 |
| 38 | 77.33 | 30.51 | 104.68 | 253.71 |
| 39 | 161.86 | 27.76 | 22.28 | 111.15 |
| 40 | 148.05 | 14.40 | 129.29 | 214.37 |
| 41 | 151.75 | 78.32 | 60.09 | 305.89 |
| 42 | 159.20 | 91.52 | 121.06 | 321.62 |
| 43 | 65.69 | 1.43 | 152.93 | 277.89 |
| 44 | 12.79 | 45.62 | 0.81 | 77.08 |

| Sampling NO. | Yaw(deg) | pitch(deg) | Roll(deg) | Deformed angle(deg) |
|---|---|---|---|---|
| 45 | 56.11 | 61.63 | 83.34 | 227.11 |
| 46 | 21.43 | 3.64 | 65.83 | 250.96 |
| 47 | 121.49 | 127.05 | 141.54 | 1.43 |
| 48 | 170.45 | 147.73 | 136.63 | 217.77 |
| 49 | 117.75 | 76.62 | 117.05 | 341.69 |
| 50 | 83.10 | 141.44 | 75.29 | 20.54 |
| 51 | 51.66 | 178.71 | 46.64 | 80.58 |
| 52 | 69.05 | 78.61 | 26.79 | 333.58 |
| 53 | 125.13 | 170.36 | 38.71 | 67.13 |
| 54 | 95.80 | 79.35 | 112.92 | 113.17 |
| 55 | 149.80 | 37.62 | 107.85 | 238.49 |
| 56 | 65.25 | 36.19 | 170.63 | 75.57 |
| 57 | 22.06 | 136.41 | 93.60 | 164.89 |
| 58 | 153.38 | 166.73 | 165.59 | 190.75 |
| 59 | 86.23 | 152.14 | 44.72 | 158.28 |
| 60 | 53.41 | 74.23 | 99.89 | 180.77 |
| 61 | 110.70 | 167.92 | 18.67 | 65.99 |
| 62 | 103.99 | 86.67 | 147.51 | 33.04 |
| 63 | 174.51 | 128.20 | 34.69 | 340.66 |
| 64 | 13.53 | 92.36 | 102.64 | 39.94 |
| 65 | 131.90 | 66.55 | 145.93 | 124.00 |
| 66 | 164.76 | 112.55 | 166.10 | 287.33 |
| 67 | 38.64 | 120.16 | 115.24 | 44.92 |
| 68 | 163.89 | 39.69 | 36.56 | 201.04 |
| 69 | 150.65 | 104.16 | 18.37 | 310.36 |
| 70 | 120.51 | 169.38 | 68.58 | 343.16 |
| 71 | 118.46 | 156.94 | 176.98 | 165.76 |
| 72 | 98.77 | 173.27 | 52.87 | 94.85 |
| 73 | 34.62 | 116.57 | 43.25 | 63.71 |
| 74 | 112.95 | 73.55 | 29.74 | 245.09 |
| 75 | 74.41 | 82.25 | 159.46 | 36.86 |
| 76 | 87.99 | 2.01 | 83.63 | 48.80 |
| 77 | 107.70 | 60.37 | 100.84 | 246.64 |
| 78 | 160.32 | 137.19 | 3.22 | 148.12 |
| 79 | 26.59 | 119.30 | 89.37 | 89.28 |
| 80 | 177.44 | 83.65 | 147.60 | 107.71 |
| 81 | 158.62 | 165.79 | 12.42 | 194.91 |
| 82 | 88.63 | 175.44 | 62.86 | 55.96 |
| 83 | 152.92 | 92.43 | 72.97 | 3.27 |
| 84 | 60.14 | 81.15 | 131.24 | 0.02 |
| 85 | 96.82 | 139.68 | 171.47 | 184.02 |
| 86 | 136.49 | 23.63 | 174.38 | 330.73 |
| 87 | 75.18 | 143.58 | 113.90 | 346.66 |
| 88 | 55.53 | 133.29 | 150.74 | 128.03 |
| 89 | 55.09 | 109.51 | 53.65 | 200.35 |
| 90 | 104.43 | 54.08 | 70.61 | 130.34 |
| 91 | 89.39 | 107.59 | 43.86 | 186.33 |
| 92 | 90.26 | 105.53 | 175.86 | 23.07 |

| Sampling NO. | Yaw(deg) | pitch(deg) | Roll(deg) | Deformed angle(deg) |
|---|---|---|---|---|
| 93 | 176.40 | 36.64 | 2.14 | 100.68 |
| 94 | 144.50 | 13.80 | 122.36 | 136.90 |
| 95 | 44.10 | 40.70 | 71.01 | 279.98 |
| 96 | 173.15 | 177.82 | 127.90 | 47.86 |
| 97 | 9.04 | 140.88 | 27.66 | 141.89 |
| 98 | 2.71 | 9.79 | 17.03 | 333.90 |
| 99 | 42.78 | 101.07 | 104.15 | 87.82 |
| 100 | 61.58 | 46.93 | 157.80 | 263.28 |
| 101 | 72.99 | 96.44 | 111.02 | 115.72 |
| 102 | 156.64 | 106.65 | 143.68 | 170.61 |
| 103 | 169.97 | 10.24 | 6.40 | 232.84 |
| 104 | 13.90 | 155.91 | 112.44 | 242.34 |
| 105 | 81.31 | 89.87 | 67.87 | 163.01 |
| 106 | 172.46 | 35.66 | 30.33 | 3.80 |
| 107 | 48.16 | 176.00 | 28.38 | 153.59 |
| 108 | 6.20 | 160.63 | 7.25 | 302.81 |
| 109 | 1.05 | 115.49 | 77.93 | 328.98 |
| 110 | 46.62 | 67.67 | 175.67 | 210.76 |
| 111 | 122.11 | 163.46 | 155.11 | 303.93 |
| 112 | 30.63 | 159.98 | 108.72 | 131.54 |
| 113 | 128.01 | 12.31 | 77.14 | 307.28 |
| 114 | 75.79 | 18.94 | 4.10 | 317.43 |
| 115 | 71.43 | 42.64 | 136.87 | 224.97 |
| 116 | 174.60 | 59.43 | 122.98 | 143.96 |
| 117 | 18.35 | 148.89 | 8.18 | 92.13 |
| 118 | 52.34 | 5.34 | 131.48 | 359.03 |
| 119 | 81.93 | 45.10 | 144.76 | 229.07 |
| 120 | 127.40 | 129.43 | 13.41 | 270.67 |
| 121 | 135.54 | 19.48 | 90.90 | 314.79 |
| 122 | 3.19 | 152.94 | 178.74 | 167.45 |
| 123 | 142.63 | 32.73 | 74.84 | 99.58 |
| 124 | 64.06 | 84.42 | 125.72 | 171.97 |
| 125 | 82.64 | 48.83 | 39.89 | 11.73 |
| 126 | 18.62 | 102.38 | 92.64 | 82.54 |
| 127 | 68.53 | 173.63 | 11.72 | 199.10 |
| 128 | 29.58 | 27.09 | 6.95 | 145.75 |
| 129 | 62.41 | 154.29 | 91.49 | 271.69 |
| 130 | 171.79 | 90.87 | 55.71 | 297.51 |
| 131 | 139.08 | 110.02 | 14.25 | 203.78 |
| 132 | 150.29 | 0.41 | 125.28 | 204.70 |
| 133 | 26.12 | 90.55 | 59.58 | 217.00 |
| 134 | 41.12 | 131.39 | 140.67 | 205.34 |
| 135 | 106.23 | 100.42 | 35.94 | 172.91 |
| 136 | 1.44 | 177.31 | 5.79 | 125.48 |
| 137 | 56.90 | 95.37 | 138.07 | 291.44 |
| 138 | 118.82 | 11.67 | 78.53 | 286.19 |
| 139 | 39.84 | 22.59 | 90.08 | 103.45 |
| 140 | 122.53 | 88.79 | 48.77 | 71.28 |

| Sampling NO. | Yaw(deg) | pitch(deg) | Roll(deg) | Deformed angle(deg) |
|---|---|---|---|---|
| 141 | 24.25 | 31.41 | 70.10 | 90.38 |
| 142 | 91.38 | 84.87 | 148.87 | 72.64 |
| 143 | 27.10 | 113.75 | 153.55 | 201.95 |
| 144 | 97.67 | 22.92 | 46.98 | 192.85 |
| 145 | 53.25 | 17.90 | 124.40 | 115.17 |
| 146 | 36.24 | 5.55 | 49.99 | 299.40 |
| 147 | 85.70 | 18.31 | 85.21 | 18.97 |
| 148 | 101.60 | 75.35 | 20.96 | 146.44 |
| 149 | 61.96 | 81.79 | 56.63 | 320.68 |
| 150 | 134.31 | 150.60 | 169.51 | 313.66 |
| 151 | 66.35 | 43.81 | 79.02 | 79.94 |
| 152 | 5.87 | 146.40 | 161.91 | 84.11 |
| 153 | 80.83 | 68.69 | 114.03 | 335.36 |
| 154 | 64.39 | 6.20 | 126.02 | 231.90 |
| 155 | 70.34 | 132.71 | 98.48 | 101.51 |
| 156 | 8.79 | 31.06 | 71.55 | 35.59 |
| 157 | 135.84 | 6.80 | 86.17 | 249.90 |
| 158 | 16.10 | 108.29 | 160.43 | 206.63 |
| 159 | 59.85 | 140.26 | 119.57 | 39.13 |
| 160 | 83.97 | 124.54 | 25.77 | 56.67 |
| 161 | 125.90 | 51.23 | 69.26 | 257.39 |
| 162 | 49.32 | 99.20 | 150.27 | 9.13 |
| 163 | 146.36 | 33.21 | 52.22 | 96.74 |
| 164 | 137.34 | 98.45 | 84.53 | 350.54 |
| 165 | 66.94 | 38.04 | 60.82 | 5.12 |
| 166 | 50.39 | 125.37 | 27.51 | 284.68 |
| 167 | 129.50 | 70.55 | 115.07 | 279.01 |
| 168 | 79.81 | 41.12 | 124.18 | 29.51 |
| 169 | 171.27 | 106.03 | 162.14 | 252.15 |
| 170 | 116.45 | 25.64 | 139.65 | 15.30 |
| 171 | 22.82 | 49.45 | 61.93 | 17.98 |
| 172 | 142.13 | 16.48 | 109.43 | 284.28 |
| 173 | 124.80 | 71.18 | 31.18 | 276.23 |
| 174 | 25.19 | 155.07 | 1.25 | 355.22 |
| 175 | 42.02 | 111.55 | 81.38 | 345.01 |
| 176 | 168.98 | 67.03 | 156.95 | 264.68 |
| 177 | 41.73 | 118.50 | 32.45 | 349.56 |
| 178 | 5.14 | 114.26 | 58.53 | 41.74 |
| 179 | 100.68 | 60.95 | 168.02 | 237.51 |
| 180 | 0.32 | 32.09 | 172.08 | 139.85 |
| 181 | 103.39 | 167.16 | 151.33 | 197.54 |
| 182 | 89.73 | 97.11 | 155.50 | 338.11 |
| 183 | 155.75 | 168.07 | 64.94 | 318.29 |
| 184 | 107.26 | 87.39 | 152.17 | 78.04 |
| 185 | 7.28 | 164.05 | 50.43 | 22.69 |
| 186 | 123.04 | 138.85 | 141.88 | 75.86 |
| 187 | 29.21 | 93.82 | 100.47 | 240.97 |
| 188 | 169.22 | 4.44 | 13.02 | 160.79 |

| Sampling NO. | Yaw(deg) | pitch(deg) | Roll(deg) | Deformed angle(deg) |
|---|---|---|---|---|
| 189 | 4.27 | 43.37 | 109.95 | 175.91 |
| 190 | 128.51 | 79.97 | 135.53 | 255.43 |
| 191 | 137.61 | 158.75 | 167.90 | 119.36 |
| 192 | 126.10 | 161.89 | 14.41 | 300.53 |
| 193 | 78.57 | 115.19 | 41.96 | 294.37 |
| 194 | 162.85 | 86.16 | 132.14 | 111.75 |
| 195 | 94.20 | 142.88 | 118.54 | 292.78 |
| 196 | 113.85 | 64.88 | 103.72 | 6.38 |
| 197 | 30.54 | 121.32 | 31.77 | 301.22 |
| 198 | 154.65 | 63.27 | 173.42 | 177.62 |
| 199 | 91.01 | 24.79 | 178.06 | 31.85 |
| 200 | 167.67 | 85.39 | 57.37 | 208.38 |
| 201 | 139.62 | 7.91 | 11.31 | 49.22 |
| 202 | 44.57 | 101.92 | 168.85 | 331.82 |
| 203 | 32.14 | 171.50 | 82.54 | 260.02 |
| 204 | 25.29 | 33.78 | 40.74 | 46.34 |
| 205 | 49.05 | 9.39 | 59.40 | 70.78 |
| 206 | 46.91 | 83.02 | 163.56 | 181.80 |
| 207 | 47.50 | 72.10 | 174.67 | 105.45 |
| 208 | 92.25 | 172.65 | 19.62 | 234.83 |
| 209 | 63.16 | 122.48 | 169.99 | 30.89 |
| 210 | 148.40 | 130.23 | 111.76 | 274.80 |
| 211 | 105.73 | 21.93 | 142.86 | 108.27 |
| 212 | 159.75 | 94.60 | 164.57 | 50.81 |
| 213 | 133.20 | 163.11 | 17.61 | 93.12 |
| 214 | 126.74 | 123.11 | 166.39 | 352.20 |
| 215 | 157.87 | 76.92 | 47.56 | 67.66 |
| 216 | 31.59 | 55.99 | 40.86 | 326.24 |
| 217 | 28.31 | 179.27 | 24.04 | 52.46 |
| 218 | 93.02 | 136.00 | 98.14 | 169.40 |
| 219 | 59.26 | 58.17 | 49.59 | 338.56 |
| 220 | 120.95 | 69.50 | 148.24 | 44.33 |
| 221 | 50.40 | 104.76 | 21.03 | 281.41 |
| 222 | 43.43 | 131.46 | 142.76 | 235.40 |
| 223 | 111.59 | 74.60 | 101.79 | 261.70 |
| 224 | 112.23 | 112.00 | 0.59 | 59.04 |
| 225 | 179.37 | 174.11 | 96.36 | 134.43 |
| 226 | 177.62 | 150.45 | 39.24 | 248.91 |
| 227 | 132.35 | 69.66 | 106.71 | 155.92 |
| 228 | 151.89 | 47.83 | 87.36 | 87.50 |
| 229 | 72.07 | 145.43 | 121.75 | 315.63 |
| 230 | 33.91 | 93.12 | 48.23 | 244.26 |
| 231 | 143.35 | 88.18 | 164.20 | 238.93 |
| 232 | 116.11 | 26.47 | 120.55 | 12.11 |
| 233 | 178.42 | 20.41 | 162.75 | 229.25 |
| 234 | 140.04 | 53.61 | 79.95 | 15.87 |
| 235 | 175.45 | 176.77 | 146.86 | 266.46 |
| 236 | 33.20 | 16.96 | 85.01 | 354.39 |

| Sampling NO. | Yaw(deg) | pitch(deg) | Roll(deg) | Deformed angle(deg) |
|---|---|---|---|---|
| 237 | 131.17 | 46.25 | 136.10 | 247.54 |
| 238 | 58.78 | 65.70 | 2.97 | 268.63 |
| 239 | 109.75 | 118.09 | 179.07 | 209.90 |
| 240 | 93.61 | 20.12 | 15.20 | 349.07 |
| 241 | 102.44 | 7.76 | 33.61 | 28.36 |
| 242 | 166.77 | 54.65 | 93.06 | 327.64 |
| 243 | 84.16 | 168.89 | 139.11 | 179.57 |
| 244 | 19.59 | 161.25 | 67.75 | 122.48 |
| 245 | 138.14 | 129.96 | 54.39 | 309.48 |
| 246 | 73.93 | 120.62 | 31.89 | 8.25 |
| 247 | 95.38 | 113.01 | 159.78 | 73.81 |
| 248 | 60.72 | 39.14 | 52.10 | 174.09 |
| 249 | 111.65 | 128.93 | 66.48 | 320.24 |
| 250 | 156.03 | 34.64 | 9.04 | 259.03 |
| 251 | 115.24 | 159.11 | 38.24 | 311.60 |
| 252 | 96.07 | 13.94 | 95.38 | 149.45 |
| 253 | 166.90 | 56.75 | 45.81 | 27.59 |
| 254 | 67.85 | 148.39 | 107.17 | 10.31 |
| 255 | 2.06 | 24.19 | 145.38 | 189.38 |
| 256 | 6.67 | 134.89 | 73.76 | 184.95 |
| 257 | 145.07 | 89.39 | 139.84 | 282.54 |
| 258 | 175.93 | 52.78 | 128.85 | 292.97 |
| 259 | 134.75 | 110.94 | 179.60 | 261.54 |
| 260 | 57.82 | 38.49 | 4.65 | 275.39 |
| 261 | 130.20 | 125.94 | 117.63 | 122.23 |
| 262 | 22.71 | 50.81 | 95.80 | 211.87 |
| 263 | 165.98 | 34.96 | 166.84 | 289.85 |
| 264 | 143.99 | 57.38 | 123.44 | 53.62 |
| 265 | 35.69 | 164.69 | 87.69 | 214.89 |
| 266 | 84.83 | 122.24 | 56.01 | 347.13 |
| 267 | 173.91 | 135.25 | 81.82 | 161.24 |
| 268 | 38.34 | 174.92 | 76.62 | 93.67 |
| 269 | 57.03 | 77.56 | 21.81 | 336.32 |
| 270 | 7.86 | 53.34 | 89.41 | 61.77 |
| 271 | 34.92 | 149.41 | 137.58 | 358.02 |
| 272 | 16.75 | 72.95 | 88.59 | 255.92 |
| 273 | 130.18 | 132.12 | 61.36 | 193.35 |
| 274 | 14.50 | 117.34 | 74.22 | 102.16 |
| 275 | 98.31 | 153.11 | 126.92 | 38.13 |
| 276 | 141.04 | 71.71 | 157.94 | 42.84 |
| 277 | 15.04 | 179.68 | 132.88 | 269.51 |
| 278 | 119.94 | 55.79 | 28.92 | 126.97 |
| 279 | 86.47 | 8.64 | 26.31 | 136.57 |
| 280 | 77.76 | 62.26 | 20.28 | 152.22 |
| 281 | 110.32 | 144.19 | 51.14 | 297.77 |
| 282 | 179.52 | 142.49 | 10.02 | 222.08 |
| 283 | 28.12 | 58.68 | 33.30 | 57.86 |
| 284 | 39.31 | 162.10 | 173.02 | 26.21 |

| Sampling NO. | Yaw(deg) | pitch(deg) | Roll(deg) | Deformed angle(deg) |
|---|---|---|---|---|
| 285 | 160.94 | 116.34 | 35.15 | 85.53 |
| 286 | 10.83 | 16.04 | 86.88 | 24.97 |
| 287 | 16.83 | 123.93 | 130.76 | 60.65 |
| 288 | 105.41 | 64.46 | 92.33 | 62.57 |
| 289 | 3.65 | 29.34 | 102.34 | 110.24 |
| 290 | 23.62 | 11.33 | 134.17 | 226.06 |
| 291 | 78.81 | 142.19 | 172.65 | 272.83 |
| 292 | 99.23 | 157.54 | 75.81 | 187.50 |
| 293 | 45.57 | 2.82 | 116.01 | 243.29 |
| 294 | 76.39 | 44.84 | 10.43 | 118.14 |
| 295 | 165.02 | 12.81 | 156.58 | 105.67 |
| 296 | 70.85 | 63.74 | 154.65 | 140.46 |
| 297 | 99.95 | 67.85 | 177.17 | 116.87 |
| 298 | 37.01 | 126.31 | 72.16 | 153.83 |
| 299 | 67.73 | 80.48 | 66.67 | 164.02 |
| 300 | 157.35 | 156.55 | 127.48 | 83.67 |

# Appendix E

## Appendix E

### E.1 Instrument and interface

The high power spotlight (2,000 W) and dimmer to vary the power of the spotlight, which is used in the forced experiment are shown in Figure E.1.

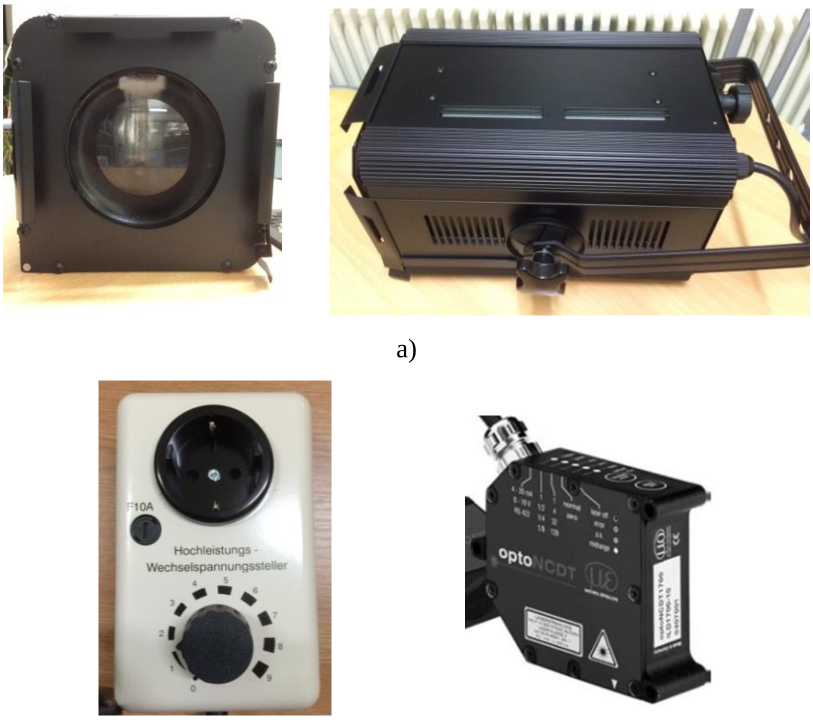

a)

b)

c)

**Figure E.1 Instruments in the forced motion experiment. a) high power spotlight (2000W) b) dimmer c) laser displacement sensor (resolution 0.1 μm).**

The schematic drawing to interface the laser sensor (optoNCDT 1700, MICRO-EPSILON) [64] connected with a laptop is shown in Figure E.2. The power supply is capable to covert from AC 220 V to DC power 15 V to supply the laser sensor. A RS422/USB converter [64]is a converter to interface the sensor with a laptop by using USB line. The transmitted data of a RS422 requiring in order to connect the sensor have 4 lines (Rx-, Rx+, Tx- and Tx+). The input lines, which are Rx- and Rx+ (yellow and grey colours respectively), receive data from interface programme on a laptop into a sensor and another two lines, which are Tx- and Tx+ (brown and green colours respectively), use to send the measured data back to a interface programme.

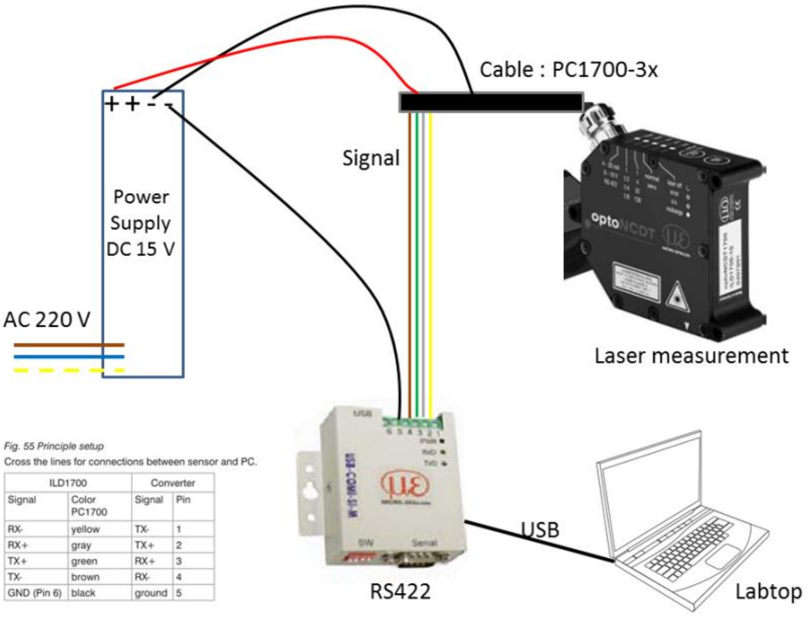

*Fig. 55 Principle setup*

Cross the lines for connections between sensor and PC.

| ILD1700 | | Converter | |
|---|---|---|---|
| Signal | Color PC1700 | Signal | Pin |
| RX- | yellow | TX- | 1 |
| RX+ | gray | TX+ | 2 |
| TX+ | green | RX+ | 3 |
| TX- | brown | RX- | 4 |
| GND (Pin 6) | black | ground | 5 |

**Figure E.2 Schematic drawing of interface of laser sensor with Laptop.**

# E.2 Object tracking test

In the chapter 5 of the free motion experiment, object tracking algorithm is to detect and measure the movement of red pixels. Before implementing with the experiment, there are two simulated tests. In the first test, we use the programme to detect the movement of a red balls and red heart as shown in Figure E.3 and Figure E.4 respectively. Both results of tests show that this algorithm is able to capture the movements of both red ball and red hearts in over time of simulations by using the blue frame.

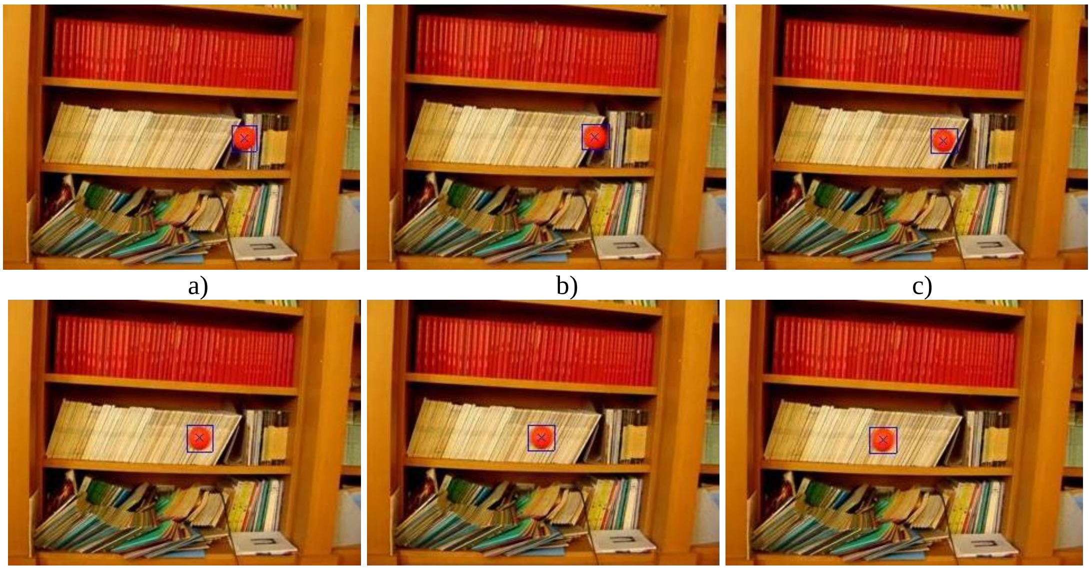

a) b) c)

d) e) f)

**Figure E.3 Object tracking simulation to detect the movement of a red ball a)-f) show the detection of red ball's motion from left to right sides in 2 seconds.**

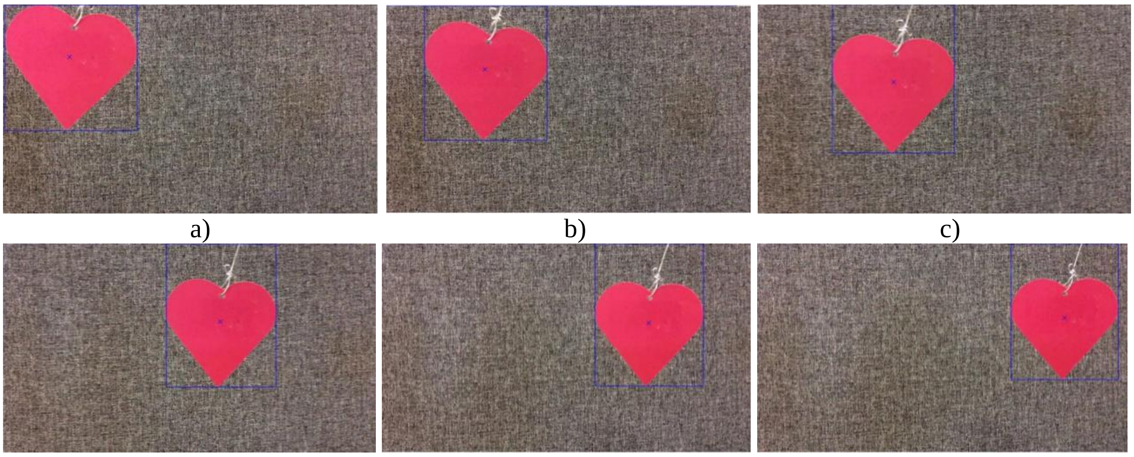

a) b) c)

d) e) f)

**Figure E.4 Object tracking simulation to detect the movement of a red heart a)-f) show the detection of pink heart’s motion from left to right sides in 5 seconds.**

# Bibliography

1. Desmond, B. *Accessing China's ASAT program*. http://rmit.nautilus.org/forum-reports/0714s-ball/fig3-debris.html 2007.
2. Tariq, M. *Debris From Space Collision Poses Threat to Other Satellites*. 2009.
3. Krisko, P.H., *EVOLVE historical and projected orbital debris test environment.* Advance Space in Research, 2004. 34: p. 975-980.
4. Johnson, N.L., et al., *NASA's new breakup model of evolve 4.0.* Advances in Space Research, 2001. 28(9): p. 1377-1384.
5. Anz-Meador, P.D. and M.J. Matney, *An assessment of the NASA explosion fragmentation model to 1 mm characteristic sizes.* Advances Space in Research, 2004. 34: p. 987-992.
6. Yi-yong, L., S. Huai-rong, and L. Zhi, *Faster algorithm of debris cloud orbital character from spacecraft collision breakup.* Advances in Space Research, 2009. 43: p. 1527-1531.
7. Krisko, P.H. and D.T. Hall, *Geosynchronous region orbital debris modeling with GEO_EVOLVE 2.0.* Advances Space in Research, 2004. 34: p. 1166-1170.
8. Liou, J.-C., et al., *LEGEND – a three-dimensional LEO-to-GEO debris evolutionary model.* Advances Space in Research, 2004. 34: p. 981-986.
9. Liou, J.-C., *Collision activities in the future orbital debris environment.* Advance Space in Research, 2006. 38: p. 2102 - 2106.
10. Klinkrad, H., et al., *An Introduction to the 1997 ESA Master Model*, in *Second European Conference on Space Debris*. 1997: Darmstadt, Germany. p. 217.
11. Schildknecht, T., R. Musci, and T. Flohrer, *Properties of the high area-to-mass ratio space debris population at high altitudes.* Advances Space in Research, 2008. 41(5): p. 1039-1045.
12. Schildknecht, T., et al., *Optical observation of space debris in GEO and in highly-eccentric orbits.* Advance Space in Research, 2004. 34: p. 901-911.
13. Flegel, S.K., et al., *Multi-layer insulation model for MASTER-2009.* Acta Astronautica, 2011. 69.
14. Früh, C., T.M. Kelecy, and M.K. Jah, *Coupled Orbit-Attitude Dynamics of High Area-to-Mass Ratio (HAMR) Objects: Influence of Solar Radiation Pressure, Shadow Paths and the Visibility in Light Curves.* Celestial Mechanics and Dynamical Astronomy (CELE), 2013.
15. Mozurkewich, D., *Toward Realistic Dynamics of Rotating Orbital Debris and Implications for Lightcurve Interpretation*, in *Advanced Maui Optical and Space Surveillance Technologies Conference*. 2011: Maui, Hawaii.
16. Früh, C. and T. Schildknecht, *Variation of Area-to-Mass-Ratio of HAMR Space Debris objects.* Monthly Notices of the Royal Astronomical Society, 2011. 419(4): p. 3521-3528.
17. Liou, J.-C. and J.K. Weaver. *Orbital Dynamics of High Area-To Ratio Debris and Their Distribution in the Geosynchronous Region*. in *Proceedings of the 4th European Conference on Space Debris*. 2005. Darmstadt, Germany.
18. Sheldahl. *The red book.* 2012; Available from: http://www.sheldahl.com/documents/RedBook%20revised%2020-AUG%20%202012.pdf.
19. Dever, J.A., et al., *Mechnical properties degradation of TEFLON FEP returned from the hubble space telescope*, in *36th Aerospace Sciences Meeting&Exhibit*. 1998.
20. Pardini, C. and L. Anselmo, *Evolution of the debris cloud generated by the FENGYUN-1C fragmentation event.*

21. Anselmo, L. and C. Pardini, *Long-term dynamical evolution of high area-to-mass ratio debris released into high earth orbits.* Acta Astronautica, 2010. 67: p. 204-216.
22. Sen, L., et al., *A model to describe the size distribution of satellite breakup debris*, in *63rd International Astronautical Congress*. 2012: Naples, Italy.
23. Murakami, J., et al., *Micro-satellite impact tests to investigate multi-layer insulation fragments*, in *Space Systems Dynamics Laboratory*. 2008, Kyushu University.
24. Valk, S. and A. Lemaître, *Semi-analytical investigations of high area-to-mass ratio geosynchronous space debris including Earth's shadowing effects.* Advances in Space Research, 2008. 42.
25. Valk, S., A. Lemaitre, and L. Anselmo, *Analytical and semi-analytical investigations of geosynchronous space debris with high area-to-mass ratio.* Advances in Space Research, 2008. 41.
26. Valk, S., A. Lemaître, and F. Deleflie, *Semi-analytical theory of mean orbital motion for geosynchronous space debris under gravitational influence.* Advances in Space Research, 2008. 43(7): p. 1070-1082.
27. Früh, C. and M. Jah, *Coupled orbit-attitude motion of high area-to-mass ratio (HAMR) objects including efficient self-shadowing.* Acta Astronautica, 2014. 95: p. 227-241.
28. Musci, R., T. Schildknecht, and M. Ploner, *Analyzing long observation arcs for objects with high area-to-mass ratio in geostationary orbits.* Acta Astronautica, 2010. 66: p. 693-703.
29. Sakva, N. and V. Agapov, *Orbit evolution of specular non-spherical space debris objects high area to mass ratio*, in *66th International Astronautical Congress*. 2015: Jerusalem, Israel.
30. McMahon, J.W. and D.J. Scheeres. *High-fidelity solar radiation pressure effects for high area-to-mass ratio debris with changing shapes*. in *Proceeding AAS/AIAA Astrodynamics Specialist Conference*. 2013. Hilton Head Island, South Carolina Paper AAS 13-763.
31. Rosengren, A.J. and D.J. Scheeres, *Long-term dynamics of high area-to-mass ratio objects in high-Earth orbit.* Addvances in Space Research, 2013. 52: p. 1545-1560.
32. Schildknecht, T., et al. *Color photometry and light curve observations of space debris in GEO*. in *Proceedings of Advanced Maui Optical and Space Surveillance Technologies Conference*. 2008. Maui Hawaii.
33. Früh, C., et al. *Passive Electrostatic Charging of Near-Geosynchronous Space Debris HAMR Ojects and its Effects on the Coupled Object Dynamics*. in *Proc. AAS Space Flight Mechanics Meeting*. 2014. Santa Fe, NM.
34. Channumsin, S., et al., *Orbital dynamics of lightweight flexible debris*, in *International Astronautical Congress*. 2013: Beijing China.
35. Channumsin, S., M. Ceriotti, and G. Radice, *A Deformation model of Flexible, high area-to-mass ratio debris for accurate propagation under perturbation*, in *65th International Astronautical Congress*. 2014: Toronto, Canada.
36. Vallado, D.A., *Fundamentals of Astrodynamics and Applications*. 2007, New York: Microcosm Press.
37. Knocke, P. and J. Ries, *Earth Radiation Pressure Effects on Satellites*. 1987, The University of Texas at Austin: Austin, Texas.
38. Duha, J. and G.B. Afonso, *Thermal forces effects on satellites.* Brazilian Journal of Geophysics, 1999. 17.
39. Luthcke, S.B., et al., *Enchance Radiative Force Modeling of The Tracking and Data Relay Satellites.* American Astronomical Society Jornal, 1997. 45: p. 349-370.
40. Pavlis, D.D., et al., *GEODYN-II*, ed. O. Manual. 1998, Grrenbelt, Maryland.

41. Blackburn, E.P., et al., *Spacecraft gravitational torques*, in *NASA space vehicle design criteria (guidance and control)*. 1969.
42. Schaub, H. and J.L. Junkins, *Analytical mechanics of space systems*. 2003: American Institute of Aeronautics and Astronautics.
43. C.T.F., R., *Advanced applied finite element methods*. 1998, West Sussex: Horwood Publishing Chichester.
44. Rayleigh, L., *Theory of Sound*. second ed. Vol. 2. 1877, New York: Dover.
45. ToolBox, T.E. *Young's modulus*. 2015; Available from: http://www.engineeringtoolbox.com/young-modulus-d_417.html.
46. DesigerData. *PET-Polyethylene terephthalate*. Available from: http://www.designerdata.nl/index.php?material=49&subject=2&pag=8&subpag=1&lang=en.
47. Mott, P.H. and C.M. Roland, *Limits to Poisson's ratio in isotropic materials*, N.R. Laboratory, Editor. 2009: Washington DC.
48. Schildknecht, T., *The Search for Space Debris Objects in High-Altitude Orbits*, in *Astronomical Institute, University of Bern*. 2003: Habilitation treatise.
49. Scheeres, D., A. Rosengren, and J.W. McMahon. *The Dynamics of High Area-to-Mass Ratio Ojbects in Earth Orbit: The Effect of Solar Radiation Pressure*. in *Proceedings of the 21st AAS/AIAA Space Flight Mechanics Meeting*. 2011. New Orleans, Louisana.
50. Goodfellow. *Properties of products*. 2014; Available from: http://www.goodfellow.com/.
51. Walker, M.J.H., J. Owen, and B. Ireland, *A set of modified equinoctial orbit elements*. Celestial Mechanics 1985. 36: p. 409-419.
52. Seeber, G., *Satellite Geodesy*. Walter de Gruyter, 1993.
53. Weisstein, E.W. *Sphere point picking*. 2016; Available from: http://mathworld.wolfram.com/SpherePointPicking.html.
54. Blinn, J.F., *Jim blinn's corner: Me and my (fake) shadow*. IEEE Computer Graphics & Applications8., 1988: p. 82-86.
55. Eisemann, E., et al., eds. *Real-time shadows*. 2012, CRC press,Taylor & Francis Group.
56. Matala, A., *Sample Size Requierement for Monte Carlo - simulation using Latin Hypercube Sampling*. 2008, Helsinki Universtiy of Technology.
57. Burhenne, S., D. Jacob, and G.P. Henze. *Sampling based on sobol/sequences for monte carlo techniques applied to building simulation*. in *12th Conference of International Building Performance Simulation Association*. 2011. Sydney.
58. CAPLINQ, *Technical Data Sheet LINQSTAT PIT1N-ALUM SERIES*. 2012.
59. Kalman, R.E., *A new approach to linear filtering and prediction problems.* Transaction of the ASME-Journal of Basic Engineering, 1960: p. 35-45.
60. Grewal, S. and P. Andrews, *Kalman Filtering Theory and Practice Using Matlab Grewal*, ed. n. Edition. 2001, New York: John Wiley & Sons Inc.
61. Suliman, C., C. Cruceru, and F. Moldoveanu, *Kalman Filter Based Tracking in an Video Surveillance System*, in *10th International Conference on Development and application systems*. 2010: Suceava, Romania.
62. Batchelor, G.K., *An Introduction to Fluid Dynamics*. 1967: Cambridge University Press.
63. Rafat, M.Z., M.S. Wheatland, and T.R. Bedding, *Dynamics of a double pendulum with distributed mass.* American Journal of Physics, 2009.
64. MICRO-EPSILON, *Instruction Manual optoNCDT 1700*, http://www.micro-epsilon.com/download/manuals/man--optoNCDT-1700--en.pdf, Editor. 2014.
65. Shampine, L.F., *Numerical Solution of Ordinary Differential Equations*. 1994, New York: Chapman & Hall.